Wave Theory Modeling of Three-Dimensional Seismo-Acoustic Reverberation in Ocean Waveguides

by

Henry Fan

B.S. Information Physics, Nanjing University (1988)

Submitted to the Department of Ocean Engineering
in partial fulfillment of the requirements for the degree of

Doctor of Philosophy

at the

MASSACHUSETTS INSTITUTE OF TECHNOLOGY

September 1995

Author .....
Department of Ocean Engineering
September 8, 1995

Certified by .....
Henrik Schmidt
Professor of Ocean Engineering
Thesis Supervisor

Accepted by .....
A. Douglas Carmichael
Chairman, Departmental Committee on Graduate Students

Wave Theory Modeling of Three-Dimensional Seismo-Acoustic Reverberation in Ocean Waveguides

by

Henry Fan

Submitted to the Department of Ocean Engineering
on September 7, 1995, in partial fulfillment of the
requirements for the degree of
Doctor of Philosophy

Abstract

The ocean environment is inhomogeneous on all scales of interest to sonar operation. These inhomogeneities form discontinuities in the physical properties in the medium and thereby intercept and reradiate a portion of the acoustic or seismic energy incident upon them (SCATTERING). The sum total of the scattering contributions from all the scatterers form REVERBERATION. Full wave theory models are developed in this thesis for discrete as well as diffuse reverberation. Elasticity, 3-D and waveguide effects are emphasized.

The fundamental physics of the 3-D discrete reverberation from bottom facets such as sediment covered ridge is addressed by means of a numerical model based on a hybrid wavenumber integration - boundary element (WI-BEM) approach. The bottom facet is assumed to be a 2-dimensional inclusion in an otherwise horizontally stratified seismo-acoustic environment. The elastic wave equations can then be separated by applying the spatial Fourier transform in the axial direction, leading to an integral representation for the total field in terms of solutions to 2-dimensional problems. These solutions are determined by a modified version of an existing WI-BEM model, incorporating the additional elastic boundary conditions and with the Green's functions for the stratified seismo-acoustic environment determined by a 3-dimensional version of SAFARI. The WI-BEM approach inherently decomposes the total field into basic wave components, thus enable us to visualize scattering into seismic interface waves and shear waves in the bottom.

A perturbation approach is used to model the diffuse scattering from horizontal roughness patches on the ocean bottom. A fixed cylindrical coordinate representation of the virtual seismic sources for the scattered field is introduced. It enables the incorporation of waveguide effects and the efficient computation of the scattered far field. The model is used to simulate numerically the scattering from a rough patch in the environment representing some scenarios in the ARSRP mid-Atlantic experiment. The effects of roughness statistics, bottom elasticity and waveguide physics are discussed. The principal conclusion is that Lambert's law is inadequate for representing bistatic bottom reverberation.

Thesis Supervisor: Henrik Schmidt
Title: Professor of Ocean Engineering

Acknowledgments

First, I would like to thank my thesis advisor, professor Henrik Schmidt. Henrik was the best advisor I can get. He had tremendous faith in his students, always encouraged us to find our own way, yet he was always there when we needed guidance. I was constantly fascinated by his scientific insight. He has his way of getting the grip of the most fundamental issues quickly and tell them in the simplest language. I wish I had learned more from him.

My thesis committee members have been very helpful for shaping up this thesis, especially on the presentation of the ideas. Professor Robert Fricke, thank you for the detailed suggestions on the writing and the tips on "setting yourself to success". I am grateful to Dr. D.J. Tang for introducing me to the wonderful world of the transmission-matrix and to Professor Paul Sclavounos for his support and the valuable suggestions on my presentation.

I benefited a lot from Professors Ira Dyer and Art Baggeroer, both from their excellent lectures and from the discussions at acoustic seminars.

Special thanks are also due to Dr. Peter Gerstoft and Dr. Kevin Lepage. Without their previous work, this thesis would have been impossible. Also, I would like to thank all the folks in Room 5-007 and upstairs: Qing, Hua, Ken, Dan, Chenyang, Rama, Jaiyong, Qin, Wenhua, Tarun, Matt, Joe, especially Brian and JT. The discussions with you guys have been inspirational and made my five years at MIT less of a lone journey. JT, how would you like the extra 1Gb in /project2?

I am grateful for the help of Sabina, Tacy and Judy throughout these years. Isela, trust me, no more last minute DHL packages.

Many thanks to all my friends in the volleyball and basketball clubs. I will miss those exciting games. Thank you, Feng, for offering me a place to stay for the final days at MIT. Flora, thank you for all those late night talks when I was stuck in the office.

Most special thanks to my parents and my sister. Their love and understanding has been and will always be my source of strength.

Contents

List of Figures

List of Tables

Chapter 1

Introduction

1.1 Motivation

The ocean environment is inhomogeneous on all scales of interest to sonar operation. These inhomogeneities might be within the water column (such as schools of fish) or in the sea bed (bottom inclusion), or could be rough interfaces (the tidal waves on the sea surface, the ridges on the sea-bed). These inhomogeneities form discontinuities in the physical properties in the medium and thereby intercept and reradiate a portion of the acoustic or seismic energy incident upon them. This reradiation is called SCATTERING, and the sum total of the scattering contributions from all the scatterers is called REVERBERATION. Since the reverberation distorts a transmitted signal, it plays a significant role in the use of sonar systems for target detection, localization and classification, both as noise and signal.

As noise, the reverberation is extremely difficult to eliminate in sonar signal processing due to the fact that it is generated by the signal itself. On the other hand, the reverberation contains the information of the target and the environment, which can be extracted using method such as matched field processing (MFP). In so doing, the reverberation becomes a "signal".

As in pursuing understanding of any natural phenomena, to understand the mechanism of reverberation and its effects on sonar signal processing, we have to resort to both EXPERIMENT and MODELING. First, we observe the phenomena (exper-

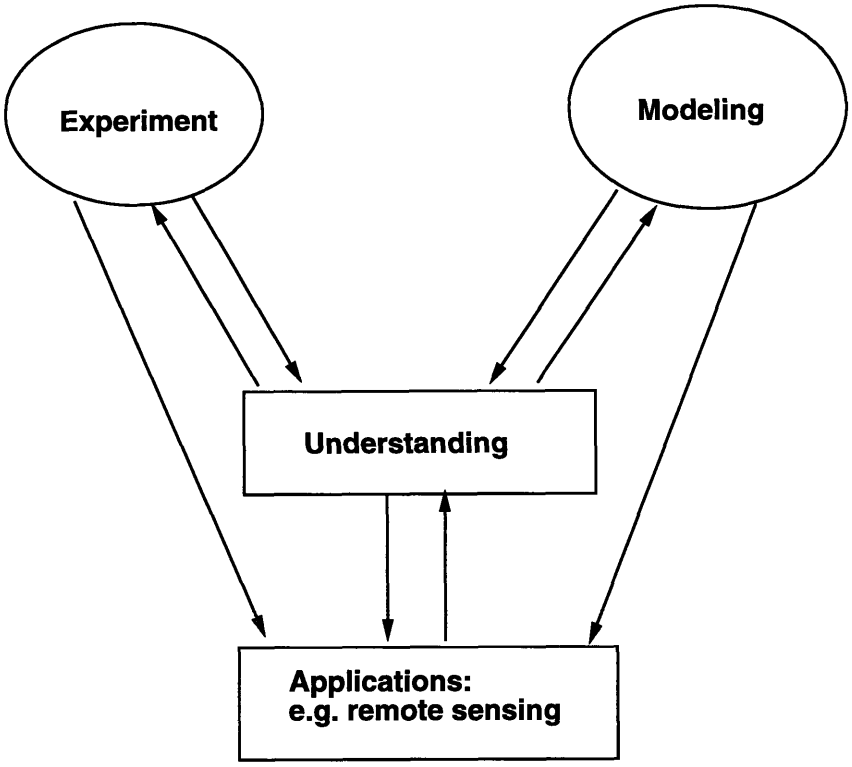

Figure 1-1: The Big Picture: How our work fits in.

iment). Then, we try to explain the observed data by attributing them to known processes (modeling). Thus, we get some preliminary understanding of what is happening. This is an iterative process. As we gain better understanding, we can design better experiments and develop better models. That, in turn, furthers our understanding of the phenomena. Ultimately, the experiment and modeling work provided us with good understanding of the physical processes as well as specific techniques, which will facilitate better applications. The process in shown in Fig. 1-1.

The reverberation in the real ocean environment calls for sophisticated mathematical/numerical models. As will be described in the next chapter, there are many kinds of scatterers and processes that contribute to the seismo-acoustic reverberation. It is virtually impossible to get a grip on the whole issue once and for all. Mathematical models can act as controlled experiments, in which the different factors can be isolated and analyzed separately, then put together. In some scenarios, such as the 3-dimensional reverberation, it is difficult enough to make sense of the results from

numerical models, let alone to solely rely on intuition to imagine what will happen.

1.2 Objectives

Within the context of the endeavor to understand the ocean reverberation (Fig. 1-1), the emphasis of this thesis is mainly on developing wave theory models (the upper left block in that figure), and using these models to further our understanding of the ocean reverberation (the middle block).

Among the many kinds of reverberation mechanisms in the ocean environment, this thesis attempts to address two types: DISCRETE and DIFFUSE scattering, their definition in the context of this thesis is given in the following.

In the received signal by a sonar in the ocean environment, discrete reverberation appears as the spikes occurring at discrete times and ranges, while diffuse reverberation appears more noise-like in the background. Discrete reverberation is caused by distinct features (FACET), such as sea mounts or ridges, and is in general considered a deterministic problem. Diffuse reverberation is caused by small scale features, such as the dust particles in the water column or the rough seabed. These features changes too frequently to be described deterministically and are numerous enough to be treated as stochastic ensembles. Actually, by examining diffuse and discrete reverberation, two extremes of the scatterer correlation lengths are covered. Discrete reverberation is caused by features with correlation lengths much longer than the acoustic wavelength and diffuse reverberation is caused by features with correlation lengths close to the acoustic wavelength. Of course, the real scatterers in the ocean environment spread all over the correlation length scale. But by examining the extremes, we gain important insights into the scattering mechanism. By changing the parameters in our model, some intermediate cases can be covered as well.

The objective of this thesis is to develop general mathematical/numerical models for discrete and diffuse scattering. These are general models in the sense that: First of all, they are full wave theory models rather than ray or normal-mode approximation. Second, some of the features generally ignored in the simpler models are included. So

the models developed here will be more versatile and provide a more complete picture of the scattering mechanism. On the other hand, they serve as bench-marks for the other simpler models. These features are:

- Three-dimensionality
- Elasticity
- Waveguide Effects

1.3 Approaches

Because of the different attributes of the discrete and diffuse scattering, we will develop separate models for each of them. But the core of both models will be the Wavenumber Integration Method [35]. This method is based on separation of variables through integral transforms, both for time and spatial domain analysis. One of the main advantages of the integral transform methods is the inherent decomposition of the total solution in both temporal and spatial spectral components, enabling interpretation of the results in terms of basic wave physics. The disadvantage of the integral transform methods is that the geometry must be separable. But the background environment (i. e., without the scatterers) we are dealing with is modeled as horizontally stratified media, which is a separable geometry. Of course, no real ocean consists of layers with exact horizontal boundaries. However, the mechanical properties of the ocean environment changes at a much faster rate in the vertical direction than in horizontal direction, so horizontal stratification is a good first approximation in most scenarios. As corrections, either slow varying range dependencies or interface roughness can be introduced. The latter is precisely one of the focuses of this thesis.

1.3.1 Discrete Scattering

Among the existing discrete scattering models, the coupled mode approach of Evans [17] is capable of modeling the 2D reverberation from facets, but is limited to purely fluid environments. It is therefore inapplicable to analysis of elastic scattering by ice

and bottom facets. Parabolic equation approaches allow sloping environments, but although some elastic PEs are being developed for elastic media and two-way propagation, they are not suited for modeling the reverberation in high-contrast media, which is exactly the basic characteristics of the environment that causes the discrete scattering.

Waterman developed Transition-matrix formulation for acoustic [83] and elastic [84] wave scattering. He expressed the incoming and scattered wavefield in terms of a series of "basic functions". The coefficients for the scattered field and those of the incoming field were linked by a matrix: Transition-matrix (T-matrix). The elements in the T-matrix can be computed by the surface integrals of the basic functions and their derivatives. Any orthogonal and complete set of functions can be selected as the basic functions. Subsequently, Ingenito [32] and Hackman [29] used T-matrix approach to produce the waveguide reverberation, where multiple scattering is accounted for through a scattering series.

Full discrete method such as Finite Difference approach has been applied to bottom scattering [14] and Arctic ice keel scattering [25, 26, 24]. Finite Difference and Finite Element [52] methods are very general because of their flexibility regarding the shape of facets. But they tend to be extremely computationally intensive since the entire environment has to be discretized by a mesh whose size is small compared to the wavelength. Thus these methods are limited to short range scattering even in two-dimensional case.

Compared to FD and FEM, Boundary Element Method (BEM) has the distinct advantage in that only the surface of the facet needs to be discretized, thus reducing the computational intensity substantially. The radiation conditions which create problems for FEM and FD in the frequency domain are automatically included in the wavefield representation. Schuster and Smith [65] combined a boundary integral method with a wavenumber integration approach to analyze scattering by rigid inclusions in a stratified fluid waveguide. Dawson and Fawcett [13, 21, 12, 20] used a similar approach to address the reverberation from the waveguide boundaries. However, both were limited to fluid waveguide and ideal, homogeneous boundary conditions.

Gerstoft and Schmidt [27] and Kawase [36, 37, 38] developed 2-Dimensional WI-BEM models capable of treating the full elastic media. In Gerstoft and Schmidt's model, both the exterior and interior domains may be stratified with any combination of acoustic, elastic and transversely isotropic layers.

The WI-BEM approach will be used in modeling the facet scattering in this thesis. Other than the reasons mentioned above, since the background ocean waveguide is horizontally stratified, the three-dimensional elastic Green's functions needed in the WI-BEM formulation can be computed efficiently by means of the existing SAFARI code. Since both the inner and outer domains can be stratified elastic media, the importance of out-of-plane elastic scattering by facets can be analyzed.

1.3.2 Diffuse Scattering

For the diffuse scattering caused by rough interface, a fair amount of models have been developed using various approaches. Among them are Rayleigh method [56, 55], the so-called boss approach [76, 77, 78, 79, 75], the Kirchhoff Approximation [40, 43] and the method of small perturbations [73, 41, 63], to name a few. Detailed descriptions and comparison will be given in Section 5.2. As described there, we here choose to use perturbation approach to model the diffuse scattering.

There have been several perturbation models developed for acoustic scattering, for example, Dacol and Berman [11] developed a second order perturbation approach to the scattering from a randomly rough interface between a fluid and an elastic half-spaces. However, their formulation is not easily generalized to predict the scattered field in a waveguide environment.

Schmidt and Kuperman [41, 63] overcame this problem by combining the physics of scattering from a rough interface and the wave guide physics governing the mean field propagation. Their self-consistent perturbation approach can be used to predict the effect of rough interfaces on the mean field as well as the higher-order statistics of waveguide reverberation. This philosophy works well with our objectives and it will be the choice of approach for our modeling of diffuse scattering.

1.4 Thesis Organization

In chapter 2, terminologies are defined. The types and causes of known ocean acoustic reverberation are described. Some of the modeling approaches are reviewed. Then we describe the Acoustic Reverberation Special Research Project (ARSRP) experiment. Finally, the central issues of this thesis are discussed.

In chapter 3, the motivation of treating the two-and-half dimensional facet reverberation problem is given and the exact problem is defined. Then the formulation of the 3-D extension of the existing 2-D WI-BEM model developed by Gerstoft and Schmidt [27] is presented.

The numerical simulation of a canonical problem is presented in chapter 4, where the scatterer is an elastic cylinder submerged in a homogeneous elastic medium. The solution is compared to an analytic solution. The result validates our 2-1/2D WI-BEM model and code. Then the reverberation from a sediment covered ridge is presented to address the effect of sediment cover. The significant wave type conversion associated with elasticity is observed in the scattered field. Subsequently, a shallow water scenario is shown. The three-dimensional effects and the modal excitation are highlighted, showing the versatility of our model.

We turn to diffuse scattering in chapter 5 and 6. The 3-D perturbation formulation is presented in chapter 5, with brief descriptions of various approaches of rough interface scattering. A fixed cylindrical coordinate representation is introduced. It enables the incorporation of waveguide effects and the efficient computation of the scattered far field.

In chapter 6, the modeling of the interface roughness is discussed. Then the scattering from a rough patch in the environment representing some scenarios in the Acoustic Reverberation Special Research Program (ARSRP) experiment is presented. We use realization for the patch profile, both isotropic and anisotropic. This problem, especially the anisotropic patch one, is inherently three-dimensional. The dependence of the scattered field on the roughness spectrum is shown. After that, patch scattering in a shallow water environment is treated with emphasis on the roles of elasticity and

waveguide effects. Finally, Lambert's law is discussed, and it is shown that in general it does not hold in scenarios we considered.

A summary of the thesis and suggestion for future work are given in chapter 7.

Chapter 2

Ocean Acoustic Reverberation

2.1 Classical Reverberation Terminologies

2.1.1 Sonar Equation

The many phenomena and effects peculiar to underwater sound produce a variety of quantitative effects on the design and operation of sonar equipment. These diverse effects can be conveniently and logically grouped together quantitatively in a small number of units called the **sonar parameter**, which, in turn, are related by the **sonar equations**. These equations are the working relationships that tie together the effects of the medium, the target, and the equipment; they are among the design and prediction tools available to the engineer for underwater sound applications.

For monostatic active sonar operating on the reverberation background, the sonar equation is

$$DT = [SL - 2TL + TS] - RL, \tag{2.1}$$

where

- parameters determined by the equipment are:
  projector source level SL, detection threshold DT,
- parameters determined by the medium are:
  transmission loss TL, reverberation level RL,

- parameter determined by the target is:
  target strength TS.

On the right hand side of the sonar equation, the terms within the bracket is the received signal level. Essentially, if the sonar is used as detection device, when the input signal-to-noise ratio is above the detection threshold DT, a decision will be made that a target is present. Otherwise, the decision will be made that the target is absent. Sonar equation corresponds to the condition that the target is just being detected.

As we mentioned before, the reverberation could be either signal or noise, depending on the circumstances. As signal, the discrete or diffuse scattering effects will be included in target strength TS. As noise, these effects will be included in reverberation level RL. In what follows, we shall define some quantities that describe these scattering effects.

2.1.2 Scattering-Strength

The fundamental ratio in the classical reverberation description is called **scattering strength**. It is the ratio, in decibel units, of the intensity of the sound scattered by a unit area or volume, referred to a unit distance, to the incident plane-wave intensity; specifically,

$$S = 10 \log \frac{I_{scat}}{I_{inc}}. \tag{2.2}$$

In the equation above, I_{inc} is the intensity of the incident plane wave. I_{scat} is the intensity of the sound scattered by an unit area or volume, measured at unit distance from the scatterer.

It is obvious that the scattering-strength is a function of the scattering direction. Traditionally, due to the monostatic usage of sonar (same sonar as both transmitting and receiving array), only the back scattering is concerned. In the back scattering direction, S is termed backscattering strength.

A related terminology is the **scattering cross section** (m_v for volume scattering

and m_s for surface scattering). It was originally used in radar applications. As the name suggested, it has the unit of area, given by the ratio of scattered power to the intensity incident upon the unit area or volume of the scatterer. Intuitively, it can be imagined to be the area spanned by the scatterer, which captures all the energy going through and reradiates it in different directions.

Scattering strength is the measure of scattering in one particular direction, while the scattering cross section is the measure of the total scattering. If it is assumed that the scattering is uniformly distributed over a sphere (for volume scattering strength S_v) or hemisphere (for surface scattering strength S_s), it follows that

$$S_v = 10 \log \frac{m_v}{4\pi}, \tag{2.3}$$

$$S_s = 10 \log \frac{m_s}{2\pi}. \tag{2.4}$$

Another concept frequently used in sonar engineering is the **equivalent plane-wave reverberation level**. This is the level of the axially incident plane wave which produces the same hydrophone voltage across the hydrophone terminals as that produced by the received reverberation.

2.1.3 Target-Strength

In active sonar the parameter **target strength** refers to the echo returned by an underwater target. Such targets may be objects of military interest, such as submarines and mines, or they may be schools of fish sought by fish-finding sonar. Excluded from the category of "targets" are inhomogeneities in the sea of indefinite extent, such as scattering layers and the ocean surface and bottom, which, because of their indefinite size, return sound in the form of **reverberation** instead of as **echoes**.

In the context of the sonar equations, target strength is defined as 10 times the logarithm to the base 10 of the ratio of the intensity of the sound returned by the target, at a unit distance from its "acoustic center" in some direction, to the incident intensity from a distant source;

$$TS \equiv 10log\frac{I_r}{I_i}, \tag{2.5}$$

where I_r is the intensity of return at unit distance and I_i is the incident intensity.

As we can see, the target strength was originally used in connection with the echoes produced by discrete targets, while scattering strength as defined here was intended to be used in connection with reverberation from extended inhomogeneities. Other than that, target strength is similar to the scattering strength in the backscattering direction.

2.1.4 Limitations of the Classical Descriptors

The sonar equations are not always adequate in many scenarios. One limitation is produced by the nature of the medium in which the sonar operate. The sea is a moving medium containing inhomogeneities of various kinds, together with irregular boundaries, one of which is in motion. Multipath propagation is the rule. As a result, many of the sonar parameters fluctuate irregularly with time, while others change because of unknown changes in the equipment and the platform on which it is mounted. Because of these fluctuations, a "solution" of the sonar equations is no more than a best-guess time average of what is to be expected in a basically stochastic problem.

Another problem is that the sonar equation is a relationship in terms of intensities. There is no phase information. In many applications, for example, matched filed processing, phase information is extremely important. This is one of the reasons that in this thesis, we do not use the classical reverberation descriptors. Instead, all the field components (displacements and tractions) and their phases are considered.

2.2 Types and Causes of Reverberation

The reverberation-producing scatterers in the sea are of three basically different classes. One type of scatterer occurs within the water column or the sea-bed and

produces **volume reverberation. Sea-surface reverberation** is produced by scatterers located on or near the sea surface (such as surface bubbles), and **bottom reverberation** originates at scatterers on or near the sea bottom. Sometimes the last two can be analyzed similarly as rough interface scattering, but bottom reverberation involves volume reverberation from inside the sediment or seabed [45].

2.2.1 Volume Reverberation

One kind of scatterers responsible for volume scattering appear to be biological in nature; that is, they are a part of the marine life existing in the sea. Nonbiological sources such as dusts and sand particles, thermal microwakes, have been shown to be insignificant contributors to the scattering strength observed at sea [54]. It was also observed [19] that the volume scatterers were not uniformly distributed in depth, but tended to be concentrated in a diffuse layer called the **deep scattering layer** (DSL) caused by schools of marine life.

At frequencies in excess of 20 kHz, the scatterers responsible for the DSL are likely to be zooplankton, or the smaller marine animals that feed upon the phytoplankton and are in turn fed upon by small pelagic fish. Examples are siphonophores and cephalopods. At lower frequencies from about 2 to 10 kHz, the dominant scatterers are the various types of fish that possess a swim bladder. It amounts to an internal air bubble that becomes resonant at a frequency which depends on the size and depth of the fish.

It was observed that the DSL showed the diurnal migration with depth. That is, it shifts upward at sunset and downward at sunrise. It is likely due to the marine animals that causes the volume reverberation migrating to keep the intensity of light illumination constant at the depth of the layer.

Another source of volume scattering is internal-waves. Garrett and Munk [3] modeled the space-time scales of internal waves. Subsequently, Flatte, Dozier and Tappert [22, 15] examined the scattering effect of internal waves.

2.2.2 Sea-Surface Reverberation

Because of its roughness and the possibility of the occurrence of entrapped air bubbles just beneath it, the sea surface is a profound scatterer of sound. This scattering has long been noted to be responsible for the reverberation received in horizontally pointing sonar under conditions such that the sound beam is not carried down into the depths of the sea by refraction.

Experiments [82] shows that the scattering strength S_s increases with wind speed at low grazing angles, but decreases with wind speed at high angles near normal incidence, with a "crossover" near 80^0. This peculiar behavior was attributed [80] to different processes responsible for the backscattering over different ranges of angle. At low angles ($< 30^0$), the scattering was attributed to a layer of air bubbles just beneath the sea surface, for which observational evidence was presented; at intermediate angles (30^0 to 70^0), scattering from the rough interface was invoked as the dominant process, and at high angles (70^0 to 90^0), the return was postulated to originate as reflection from normally inclined wave facets acting as tiny acoustic mirrors.

2.2.3 Sea-Bottom Reverberation

Like the sea surface, the bottom is an effective reflector and scatterer of sound and acts to redistribute in the ocean above it a portion of the sound incident upon it.

It was observed at an early date that the reverberation from the seabed was greater over rocky bottoms than over mud bottoms. It has since become customary to relate bottom scattering strength to the type of bottom, such as mud, silt, sand, boulders, rock, even though it is realized that the size of the particles comprising a sedimentary bottom is only an indirect indicator of acoustic scattering. Actually, the roughness of the sea bottom appears to be the dominant mechanism determining characteristics of the backscattering.

However, since the sea bottom is partly transparent to sound, in the sense that a portion of the incident acoustic energy is transmitted to the earth below, bottom type must in part determine the partition of energy between the water above and the

bottom beneath. As a matter of fact, this thesis has in-depth investigation about the effects on the reverberation of the seabed properties, such as elasticity.

In addition to the roughness, other processes may, in some circumstances, play a significant role in the scattering process. One is the particulate nature of sedimentary bottoms, where each sedimentary particle may itself be imagined to be a scatterer of sound, and where the return of sound from the bottom is produced by a form of volume reverberation within the bottom itself.

2.3 Other Reverberation Models

To present a more complete picture, here we describe some of the reverberation models that were not covered in Chapter One, and have some relevance to the thesis one way or the other. It is by no means exhaustive.

2.3.1 Lambert's Law

Lambert's law [30] is a simple classical model of rough surface scattering of sound and light.

The typical rough interface scattering scenario is shown in Fig. 2-1. Sound of intensity I_i is incident at angle θ on the small surface area dA. The power intercepted by dA will be $I_i \sin\theta dA$. This power is assumed to be scattered proportionately to the sine of the angle of scattering, so that the intensity at unit distance in the direction ϕ will be,

$$I_s = \mu I_i \sin\theta \sin\phi dA, \tag{2.6}$$

where μ is a proportionality constant. For a unit area we have, on taking 10 times the logarithm of each side,

$$10log\frac{I_s}{I_i} = 10\log\mu + 10\log(\sin\theta\sin\phi). \tag{2.7}$$

In the backward direction, for which $\phi = \pi - \theta$,

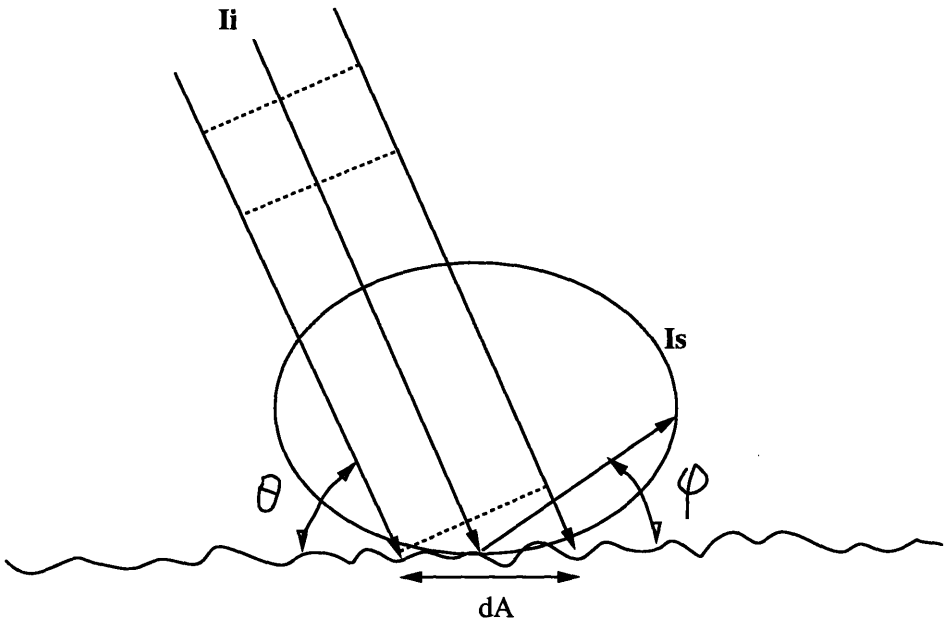

Figure 2-1: Scattering of a Plane Wave on a Rough Surface

$$S_B = 10 \log \mu + 10 \log \sin^2 \theta. \tag{2.8}$$

Thus, by Lambert's law, the backscattering strength must vary as the square of the sine of the grazing angle. If all the incident acoustic energy is redistributed into the upper medium, with none lost by transmission into the medium below, then it can be shown by integration that $\mu = \frac{1}{\pi}$; the normal-incidence backscattering strength would therefore be $10 \log(\frac{1}{\pi}) = -5dB$. It should be emphasized that the law rests on a particular assumption concerning the redistribution of the scattered energy in space. Although many materials follow Lambert's law closely in scattering light, none does so exactly. Lambert's law applies specifically to the radiation of light by radiant, absorptive materials [30]; the "law" should properly be called Lambert's "rule" for scattering. Nevertheless, it has been shown to be a good description of the backscattering of sound by very rough bottoms.

2.3.2 Volume Scattering Models

As one of the pioneers in developing models for volume scattering, Stockhausen [68] derived a volumetric backscattering strength expression assuming that the water-sediment interface is flat and refracting, and with the homogeneous sediment containing a uniform set of solid spherical particles which act to scatter the acoustic energy. Treating the small spheres as uncorrelated point scatterers, he employed Morse's expression [51] which is valid for scattering from spheres much smaller than a wavelength. In his model, Stockhausen represented all the scattering processes by a single volume backscattering cross section without further exploring any physical mechanism.

There is experimental evidence that the backscattering strength has very weak frequency dependence over the frequency range 1-100 kHz and has an angular dependence proportional to $\sin\theta$ for grazing angles θ from 5 to 50 degrees. To interpret this, Ivakin and Lysanov [34, 33] proposed that the scattering is due to the sharply anisotropic random inhomogeneities, which are large-scale in the horizontal plane and small-scale in depth in the sediment. They used the Born approximation to derive an expression for the equivalent scattering strength.

Tang [69] in his thesis and Tang and Frisk [70, 71, 72] in later papers discussed in detail the scattering from a random layer or half-space where the sound speed is assumed to be a constant plus a small random component. An integro-differential equation method was applied. An interesting point was that the spatial correlation length of the scattered field could be used to infer the correlation length of the scatterers. This provides a way of inverting for the bottom parameters critical to bottom scattering by measuring the scattered field using multiple receivers. Also taken into consideration was the anisotropy of the scatterers. Besides examining the combination of interface roughness and volume inhomogeneity effects, an attempt was made to solve the near-field problem in low-frequency scattering when the far-field assumption was not appropriate anymore.

2.3.3 Normal Mode Reverberation Models

In shallow water, the waveguide plays a very important role in the scattering and reverberation process. So normal modes will be a good approximation in the far field. Bucker and Morris [9] introduced the basic idea of using normal modes for reverberation calculations. It was developed further by Zhang and Jin [85]. In these models, normal modes were used to calculate the acoustic energy propagating from the source to the scattering area, and from the scattering area to the receiver. At the scattering patch each mode is decomposed into up- and down-going waves, then ray-mode analogies and empirical scattering functions were used to compute the scattering energy.

In a recent paper, Ellis [16] extended this work by using group velocities to obtain the travel times for each mode pair, and by further developing the ray-mode analogy. Ellis examined the effects of summing the modes coherently or incoherently and of including the time spreading due to the modal group velocities. Calculations show excellent agreement with some ray-based models, and using the Lambert bottom-scattering coefficient as the only adjustable parameter, good agreement is obtained with some measured shallow-water reverberation.

In essence, these models are still classical reverberation models in the sense that they are dealing with terms in sonar equation.

2.4 ARSRP Experiment

Beginning in 1989, the Office of Naval Research (ONR) initiated a Acoustic Reverberation Special Research Program (ARSRP). The objectives are three-fold: (1) to develop and expand the physics of low frequency acoustic scatter from the air/sea boundary zone and the ocean bottom/subbottom; (2) to quantify the essential environmental properties that govern or control the low frequency acoustic scattering; and (3) to provide the theoretical and numerical tools to properly predict low frequency acoustic reverberation.

In July 1993, the Main Acoustics Experiment (MAE) of the ARSRP was carried

out on the western flank of the Mid-Atlantic Ridge (MAR). Two research vessels were used to obtain mono- and bistatic reverberation from select bathymetric features of geomorphology characteristic to the MAR. Naturally occurring bottom morphology was exploited in the experimental design to minimize ambiguity in the receiving-array measurements and provide corridors for both direct-path (within 1/2 convergence zone (CZ)) and longer range waterborne propagation to these select sites.

In the MAE, acoustic waveforms were transmitted from the vertical source array of a slowly moving research vessel (RV) to probe scattering sites spread over wide areas on the western flank of MAR. Echo returns are measured with horizontally towed line arrays.

75% of MAE involves what is known as the B'-C' Corridor Experiments (Fig. 2-2). The B'-C' corridor is the western portion of a much longer segment valley that extends to the MAR proper. The western end of the corridor is curtailed by a highly lineated outside-corner ridge roughly 30 km in length known as B'. The eastern end is sealed by a rounded inside-corner promontory known as C'. The water-column sound-speed structure coupled with the source depth leads to a conjugate depth of 3800m for the RV CORY CHOOUEST transmissions, and a 1/2 CZ range of roughly 33km.

The B'-C' corridor was selected for a variety of reasons. First, it became clear that bathymetry to the west of the sites has greater excess depth and is therefore far more conducive to multiple CZ reverberation studies. Second, the B'-C' corridor is roughly 2 CZ in length, and generally much deeper than the conjugate depth, except for B' and C' that protrude well above the conjugate depth contour at either end. This corridor morphology was a windfall for experimental design. A source within the corridor 1/2 CZ from B' is also $1\frac{1}{2}$ CZ from C' and vice versa. Therefore direct-path returns can be simultaneously measured from B' while $1\frac{1}{2}$ CZ returns are measured from C', and vice versa. Furthermore, the ambiguous returns from along the corridor axis can be easily resolved at 1/2 CZ range for either feature due to excess depth within the corridor, and at $1\frac{1}{2}$ CZ due to interaction with B' or C' at 1/2 CZ.

Makris et. al. [48] documented the deterministic relationship between low-frequency reverberation and detailed geomorphology for wide-area insonification of

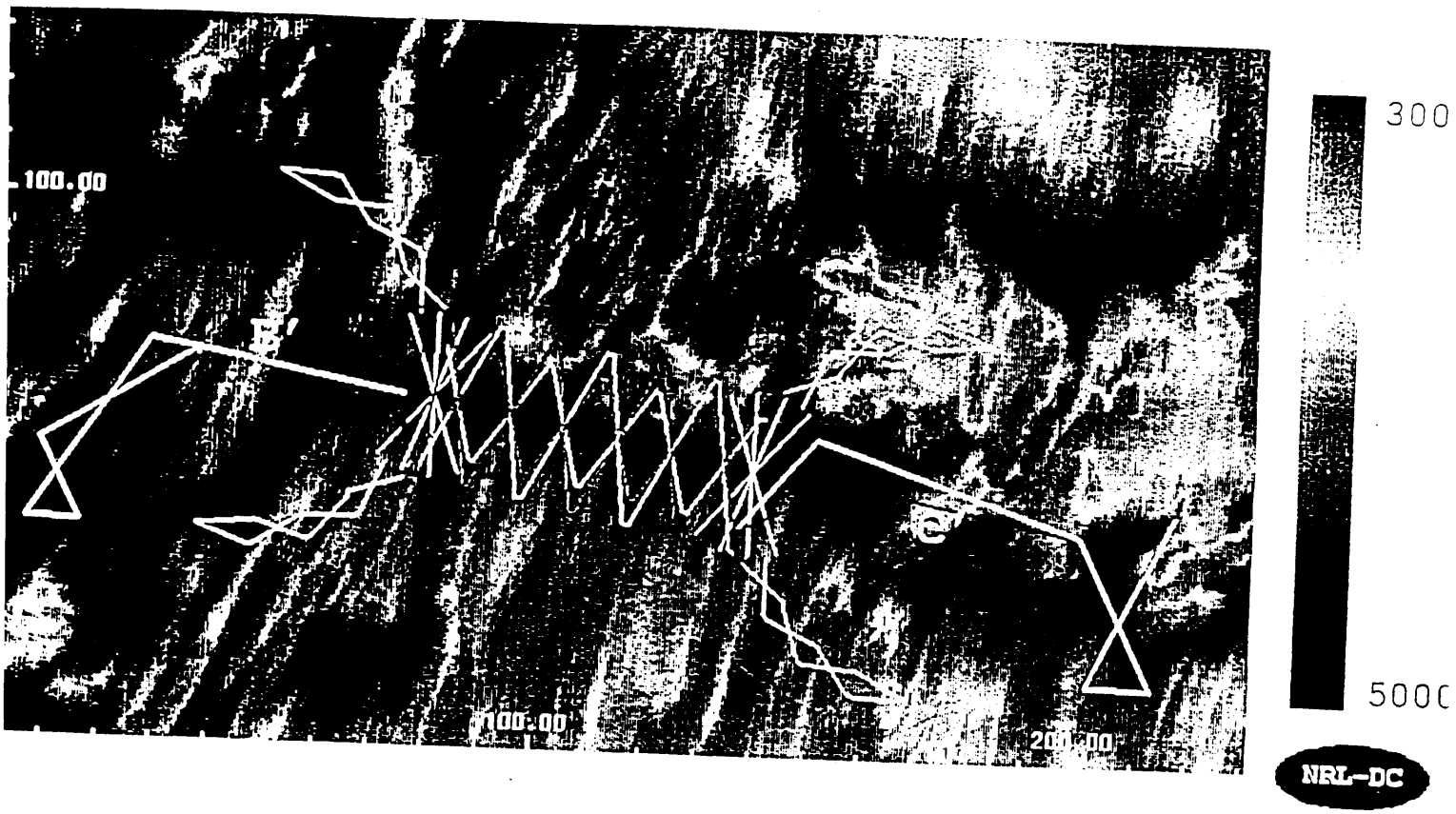

Figure 2-2: The B'-C' Corridor Experiment. The levels of contour plot represent the depth of ocean bottom. B' and C' sites are marked on the figure. Research ships travel along the lines indicated.

the B'-C' experiment. Charted reverberation registers precisely with extended ridges and has a high correlation with negative transmission loss. For a given ridge, prominent returns come from steep escarpments and cliffs that face the bistatic source and receiving arrays. Monostatic and bistatic returns form the same lineated ridge at $\frac{1}{2}$, $1\frac{1}{2}$ and $2\frac{1}{2}$ CZ ranges were used to document the registration with steep scarps.

In the B'-C' corridor, range-independent model is adequate except for the two ridges. This is exactly the kind of environment our scattering models assume.

2.5 The Issues

There are a number of scientific issues for the ARSRP. Some pertain to ocean acoustic reverberation in general while others are unique to the particular region and frequency band for the ARSRP. Some of the issues are:

- Is the concept of "scattering Strength" as used in the sonar equation useful for quantifying reverberation with a high resolution system?
- What is a good representation of the seafloor? Is the "fractal", or self similar model adequate at the small scales needed for backscattering predictions?
- What is the role of the insonification in the near field, at 1/2 CZ distances and greater?
- What are the important mechanisms for rough seafloor reverberation? Can experiments be designed to test these mechanism?
- How does the sloping seafloor affect the reverberation field?

As we stated, a good model serves as a controlled experiment. It should enable us to avoid unnecessary complexity, while retaining those basic physical process. So it is essential to examine what the important and not well-understood issues are in the ocean seismo-acoustic reverberation.

Three important issues will be addressed throughout this thesis:

- **Three-Dimensional Effects.**

  The discrete as well as diffuse scattering in the ocean environment is inherently three-dimensional, just as the geometry of the real world is three dimensional. Thus, even if the insonification is one-dimensional, such as plane wave, the reverberation field could be more complex. For example, specular as well as out-of-plane scattering occurs. Because the different sound speed in various layers, the scattering directions become more complex. The two-dimensional models are too restrictive to cover all the possibilities.

- **Elasticity.**

  Many models treat the bottom as fluid to reduce the conceptual and numerical complexity. But the real ocean bottom consists of stratified elastic layers. It is interesting to examine the effect of elasticity on the seismo-acoustic reverberation. It is shown in this thesis that elasticity plays a significant role in both discrete and diffuse scattering process. One way it affects the reverberation is through wave type conversion.

- **Waveguide Physics.**

  In the long range source/scatterer or source/receiver separation, the waveguide affects the reverberation process tremendously. It in effect acts as a filter in both the incoming and scattering wavenumber domain, and thus changes the scattering pattern as well as the level of the reverberation. It would be desirable to incorporate the waveguide physics in the reverberation model, so the short as well as long range field can be treated consistently.

So, all three of these effects might be important to the seismo-acoustic wave scattering in the ocean environment. These effects can not be treated separately and cascaded together. Rather, they are integrated parts of one problem. The models we develop must incorporate these effects in a unified formulation.

Chapter 3

2-1/2 Dimensional WI-BEM Approach

3.1 Statement of the Problem

In this and the next chapter, we will address one of the important scattering and reverberation mechanism in an ocean environment: **the discrete reverberation**.

The discrete reverberation is caused by the distinctive features in the ocean environment (the **facet**). The scattering from the facet is most substantial when the wavelength of the incoming acoustic (elastic) wave is close to the the dimension of the facet. The discrete reverberation is extremely sensitive to the signal frequency and the angle of insonification and observation. A simple analogy: a pilot in the airplane (receiving array) trying to find a mirror on the ground (facet). Most of the time the pilot won't identify the mirror. What he sees is the rivers, mountains, office buildings, etc., i.e., the background. But at a certain point, a strong glare will come into his eyes. And he deduce that there is a mirror where the glare comes from.

Although this is not the exact optical parallel to the acoustic and elastic facet scattering, it does highlight some points. Suppose we are towing a sonar array in the ocean. The received signals as appeared on the screen will be like this: over the relatively constant background, some spikes come up from time to time. The relative constant background is caused by the white electronic noise and diffuse scattering,

among other things, while the spikes are most likely caused by the facet scattering. Most of the time the scattering effect of a particular facet is insignificant compared to that of the diffuse mechanism. But at a certain angle, the facet effect will be so strong that it will overshadow virtually all other effects, just like the glare from the mirror.

Traditionally, the scattering effects were studied in the context of backscattering strength. Only the backward direction was considered. But considering the reverberation and bistatic sonar deployment, it is necessary to study **the whole scattered field** rather than just one direction.

Discrete scattering in the ocean environment is inherently **three dimensional**. Though two dimensional models can be used to solve some simple scenarios, it is quite restrictive. A case in point: the out of plane scattering effect can not be treated by a two dimensional model. Another traditional assumption often made in the scattering model is that the environment is well represented by fluid media. The sea bed is modeled either as a liquid medium or rigid body. This simplification was prompted by the limitation of the computer power, since the elastic model introduces extra equations to be solved. Some argue that the elastic effect is not important in the ocean scattering problem anyway. But we will show in the next chapter how elasticity affects the scattered field.

So, it comes down to this: we would like to model the facet scattering problem where the **full scattered field** can be simulated, and the **3-D** and **elastic** effects are considered. Also, we would like to incorporate the **waveguide physics** into our scattering formulation, so that we can integrate the scattering mechanism and the propagation process in a unified framework.

To fulfill all these criteria in a model, the computational effort would be enormous. As an intermediate step between 2-D and the full 3-D model, in this thesis we will deal with the so called $2\frac{1}{2}-D$ model. We will address the scenario where the environment is 2-dimensional, i.e., it's invariant along one direction, but the source is 3-dimensional, i.e., the source position or strength is the function of all three coordinates. Thus the field (both the incoming field and the scattered field) is inherently 3-dimensional.

The model combines the 2 dimensional environment and the 3 dimensional source and field, thus the name $2\frac{1}{2}D$. By intuition, it is natural to think that somehow this problem would be easier to cope with than the full blown three dimensional case. And as will be shown later in the chapter, it is true. There are ways to further simplify the $2\frac{1}{2} - D$ problem.

Besides the reduced computational requirement, the $2\frac{1}{2}D$ model shows clearly some of the basic physics involved in the 3 dimensional scattering effects. In the full 3 dimensional scenario, the environment and the incoming and scattered field might be too complicated for us to isolate and identify many different factors and effects. For example, with the different parts of the scatterer having various tangential planes and orientations, it would be hard to identify which part of the field is caused by the specular reflection and which was caused by the out of plane scattering. In the $2\frac{1}{2}D$ case, on the other hand, we have a relatively simpler shaped scatterer [1], and it's clearly which direction is specular and which direction is out of plane.

One might be lead to believe that the $2\frac{1}{2}D$ model is just for the theoretical investigation without any practical applications. Not so. In the real ocean environment, there are many elongated features, such as ice keel, sea mounts, salt domes, diapirs, etc. When the length of relative invariation is much bigger than the wavelength of the incoming and scattered acoustic (elastic) waves, we can practically treat the feature as infinitely long for many applications. And when the diameter of the feature is of the order of the wavelength of the incoming wave, the facet scattering effects will be significant. Our $2\frac{1}{2}D$ elastic scattering model can address this kind of problem perfectly.

Now, let's define in detail the problem we will treat in this and the next chapter.

We model the ocean environment as range-independent horizontally stratified media [2]. By that we mean the environmental properties are the same on the same horizontal plane. Media properties are functions of the depth only. The bottom is modeled as elastic layers, allowing for the sediment layers and the basement struc-

[1] one less dimension of freedom

[2] sometimes referred to as vertical stratified media in other communities.

tures. So actually, the environment is one dimensional without the scatterer. With the scatterer, an additional dimension is introduced. Without the loss of generality, we will assign a Cartesian coordinate system such that the Y-axis is parallel to the axis of invariation of the scatterer. (Fig. 3-1) So, now the Y axis is the only direction along which the environment is invariant. Thus, the environment becomes two dimensional.

The position and the strength of the source will be functions of all three coordinates. In Fig. 3-1, just to illustrate, we put a point source in the water column. Since we are simulating the whole field, rather than just the scattered amplitude in some particular direction, in effect, we have multiple horizontal and vertical receiver hydrophone arrays placed throughout the water column. Since the elastic effects are considered, the geophone arrays can be deployed anywhere on the water-seabed interface and throughout the seabed layers.

3.2 Review of the Two Dimensional Hybrid WI-BEM Method

In boundary element methods, approximations are made only on the boundary of the domain to be analyzed. At every interior point of the domain the governing partial differential equations are satisfied exactly. This contrasts with the finite element method, in which there is not in general pointwise satisfaction of the governing differential equations, resulting for example in the computation of a displacement field which corresponds to a residual body force distribution, not present in the original problem to be solved. In consequence of approximations being made only on the boundary, no interior mesh of elements need be specified, and in a numerical implementation there are no unknowns associated with interior points of the domain.

Boundary element methods can be applied only if a Green's function of the governing partial differential equations is known. A Green's function is a function that satisfies the differential equation with zero right hand side (body force) at every

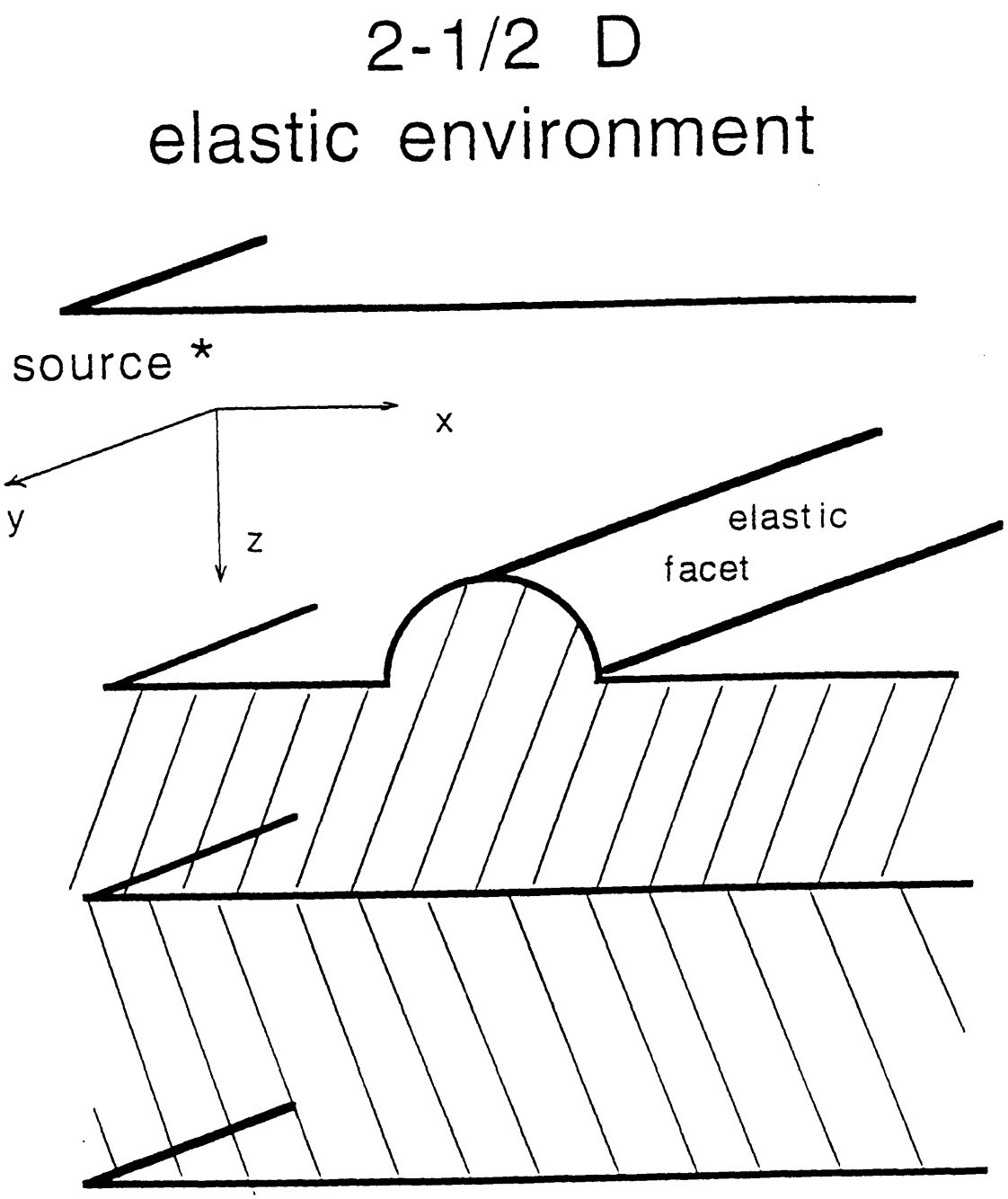

Figure 3-1: Illustration of the 2-1/2D Problem. The environment is two-dimensional. But the source and the resulting scattering field is three-dimensional

point of an infinite domain except at one point known as the source, at which the right hand side is infinite. Generally, Green's function are known for homogeneous materials, whether isotropic or not, and so boundary element methods are applicable to the analysis of homogeneous and piecewise homogeneous two and three dimensional domains.

In this thesis, the ocean environment is modeled as horizontally stratified media. And the Green's function in this environment can be efficiently computed by Wavenumber Integration (WI) method using the Direct Global Matrix (DGM) approach [59, 64]. Thus a hybrid Wavenumber Integration - Boundary Element Method (WI-BEM) approach is used.

This part of the thesis is a continuation of the work by Gerstoft and Schmidt [27]. They developed the hybrid WI-BEM approach to solve the two dimensional ocean seismo-acoustic facet reverberation problem. In this section, a review of the method is given.

3.2.1 Boundary Integral Formulation

Consider a volume V bounded by a surface S. Suppose under body force $\vec{f}(\vec{x})$ and surface traction $\vec{t}(\vec{x_s})$, the displacement field in the volume is $\vec{u}(\vec{x})$. Under a different set of body force $\vec{f^*}(\vec{x})$ and surface traction $\vec{t^*}(\vec{x_s})$, the displacement field is $\vec{u}(\vec{x})$. Here, we omitted the time dependence factor $e^{-i\omega t}$.

From the reciprocity theorem, the work done by the forces of the first system on the displacements of the second system equals the work done by the forces of the second system on the displacements of the first system:

$$\int_S t_i^* u_i dA + \int_V f_i^* u_i dV = \int_S t_i u_i^* dA + \int_V f_i u_i^* dV, \tag{3.1}$$

where the t_i, etc, are the components of the vectors $\vec{t}$, etc. $\int_S dA$ and $\int_V dV$ are the surface and volume integrals over the region, respectively.

Now, to make use of the Green's functions, we assume the first field is due to a unit force at a point $\vec{x'}$ inside the volume, $f_i^* = \delta_i(\vec{x} - \vec{x'})$, then t_j^* and u_j^* correspond

to the Green's functions $H_{ji}(\vec{x}, \vec{x'}, ; \vec{n_s}(\vec{x_s}))$ for tractions on a surface with outgoing normal vector $\vec{n_s}$ and $G_{ji}(\vec{x}, \vec{x'})$ for displacements at point $\vec{x}$. Thus Eq. (3.1) becomes

$$u_i(\vec{x}) + \int_S H_{ji}(\vec{x_s}, \vec{x}; \vec{n_s}(\vec{x_s}) dS = \int_S G_{ji}(\vec{x_s}, \vec{x}) t_j(\vec{x_s}; \vec{n_s}(\vec{x_s}) dS + \int_V G_{ij}(\vec{x}, \vec{x_V}) f_j(\vec{x_V}) dV, \tag{3.2}$$

where $u_j(\vec{x_s})$ and $t_j(\vec{x_s}; \vec{n_s})$ are the j components of displacements and tractions on the surface S, respectively. $G_{ji}(\vec{s_s}, \vec{x})$ is the displacement in the j direction at $\vec{x_s}$ due to a force in the i direction at $\vec{x}$ and $H_{ji}(\vec{x_s}, \vec{x}; \vec{n_s})$ is the traction in the j direction at the point x_s on the surface S with outgoing normal vector $\vec{n_s}$, due to a force in the i direction at a point $\vec{x}$ inside the volume.

Letting the field point $\vec{x}$ approach a point $\vec{x_s}$ on the boundary S, Eq. (3.2) becomes an integral equation for the tractions and displacements on the boundary:

$$u_i(\vec{x_s}) = \oint_S [G_{ji}(\vec{x_s}, \vec{x'}) t_j(\vec{x_s}; \vec{n_s}) - H_{ji}(\vec{x_s}, \vec{x_s'}; \vec{n_s}) u_j(\vec{x_s})] dS + \int_V G_{ij}(\vec{x_s'}, \vec{x_V}) f_j(\vec{x_V}) dV. \tag{3.3}$$

After integrating around the singularity in the $H_{ji}(\vec{x_s}, \vec{x_s'}; \vec{n_s})$ at $\vec{x_s'} = \vec{x_s}$, the integral equation become

$$C_{ij} u_j(\vec{x_s}) = \oint_S [G_{ji}(\vec{x_s}, \vec{x'}) t_j(\vec{x_s}; \vec{n_s}) - H_{ji}(\vec{x_s}, \vec{x_s'}; \vec{n_s}) u_j(\vec{x_s})] dS + \int_V G_{ij}(\vec{x_s'}, \vec{x_V}) f_j(\vec{x_V}) dV, \tag{3.4}$$

for a smooth boundary, $C_{ij} = \delta_{ij}$.

It can be easily shown that the surface integral will always vanish along parts of the boundary where the chosen Green's functions satisfy the boundary conditions. So for the typical ocean environment we are dealing with, we can choose the Green's function that satisfies the horizontally stratified boundary conditions. Then we need only to perform the surface integration on the surface that deviate from the stratified scenario, i.e., the facet. And fortunately, this kind of Green's functions are readily available from the code SAFARI [59].

After solving for the boundary displacements $\vec{u}(\vec{x_s'})$ and tractions $\vec{t}(\vec{x_s'}; \vec{n_s})$ from Eq. (3.4). The displacement fields in the region can be calculated by Eq. (3.3). The

associated stress fields can be calculated using Hooke's law.

3.2.2 Discretization

Collocation method is used to discretize Eq. (3.4). The boundary S is approximated by M linear elements, connected in M nodes, with node number m at $\vec{x}^m$ connecting elements number m and $m+1$ [3]. A local coordinate $y \in [-1,1]$ is introduced for the element. So the coordinates of points on the element can be written in terms of coordinates of the center point of the element (z_m^c, x_m^c) and y

$$\left\{ \begin{array}{c} z_m(y) \\ x_m(y) \end{array} \right\} = \left\{ \begin{array}{c} z_m^c \\ x_m^c \end{array} \right\} + \frac{l_m}{2} \left\{ \begin{array}{c} -sin\theta_m \\ cos\theta_m \end{array} \right\} y, \tag{3.5}$$

where l_m is the length of the element.

Linear shape function $N(y) = \frac{1-y}{2}$ is used to approximate the displacement and the stress distribution along the element

$$\left\{ \begin{array}{c} u(y) \\ t(y) \end{array} \right\} = \left\{ \begin{array}{c} u^{m-1} \\ t^{m-1} \end{array} \right\} N(y) + \left\{ \begin{array}{c} u^m \\ t^m \end{array} \right\} N(-y). \tag{3.6}$$

Using Eq. (3.6), Eq. (3.4) is discretized into the form

$$C^n u_i^n = \sum_{m=1}^{M} \sum_{j=1}^{2} [G_{ji}^{mn} t_j^m - H_{ji}^{mn} u_j^m] + \hat{u}_i^n, n = 1, ..., M, i = 1, 2. \tag{3.7}$$

The source contribution to the node displacements $\hat{u}_i^n$ is obtained from the volume integral in Eq. (3.4). Influence matrix elements G_{ji}^{mn} and H_{ji}^{mn} are

$$G_{ji}^{mn} = \frac{l_m}{2} \int_{-1}^{1} G_{ji}(\vec{x}_m(y), \vec{x}^n) N(-y) dy + \frac{l_{m+1}}{2} \int_{-1}^{1} G_{ji}(\vec{x}_{m+1}(y), \vec{x}^n) N(y) dy; \tag{3.8}$$

$$H_{ji}^{mn} = \frac{l_m}{2} \int_{-1}^{1} H_{ji}(\vec{x}_m(y), \vec{x}^n; \vec{n}_m) N(-y) dy + \frac{l_{m+1}}{2} \sum_{-1}^{1} H_{ji}(\vec{x}_{m+1}(y), \vec{x}^n; \vec{n}) N(y) dy. \tag{3.9}$$

[3] subscript is used to indicate element number and superscript is used to indicate node number

The kernel $G_{ji}(\vec{x}_m(y), \vec{x}^n)$ represents the displacement in the j direction at a point $\vec{x}_m(y)$ on element m, due to a virtual unit force in the i direction at the node at $\vec{x}^n$ for the exterior layered media without the facet. Similarly, the kernel $H_{ji}(\vec{x}_m(y), \vec{x}^n; \vec{n}_m)$ represents the j component of the tractions on the m-th element with outgoing normal vector $\vec{n}_m$. These kernels can be efficiently computed by the Direct Global Matrix (DGM) method of Schmidt [64, 61]. In section 3.4), I will describe a 3D version of the DGM method [60, 39].

Similarly for the interior region, a discretized boundary integral equation like Eq. (3.6) can be established, with all the quantities replaced by those of the interior region (indicated by a overbar). The node displacements and tractions in the two regions must satisfy the continuity conditions:

$$\begin{cases} \bar{\vec{u}}^m = \vec{u}^m; \\ \bar{\vec{t}}^m = -\vec{t}^m. \end{cases} \tag{3.10}$$

Now we have a system of linear equations that can be solved for the node tractions and displacements,

$$\begin{bmatrix} H & -G \\ \bar{H} & \bar{G} \end{bmatrix} \begin{Bmatrix} u \\ t \end{Bmatrix} = \begin{Bmatrix} \hat{u} \\ \hat{\bar{u}} \end{Bmatrix}. \tag{3.11}$$

Once we solved the nodal tractions and displacements, the displacement field in the external region can be determined by the discretized form of Eq. (3.3)

$$u_i(\vec{x}) = \sum_{m=1}^{M} \sum_{j=1}^{2} [G_{ji}^m(\vec{x}) t_i^m - H_{ji}^m(\vec{x}) u_j^m] + \hat{u}_i(\vec{x}), i = 1, 2. \tag{3.12}$$

The stress field follow from Hooke's law.

3.3 Reduction of the 2-1/2 D Problem

In this section, we will try to reduce the 2-1/2 D WI-BEM problem into a series of 2D problems. It is shown that the invariance of boundary conditions in one direction is instrumental in this procedure. That is the main reason we chose 2-1/2 D problem.

In 2-1/2 dimensional facet scenario, the boundary become a surface instead of a line. So Eq. (3.4) becomes

$$C_{ij}u_j(\vec{X}'_s) = \int\int_s [G_{ji}(\vec{X}_s;\vec{X}'_s)t_j(\vec{X}_s;\vec{n}_s) - H_{ji}(\vec{X}_s;\vec{X}'_s,\vec{n}_s)u_j(\vec{X}_s)]ds + \int_V G_{ij}(\vec{X}'_s;\vec{X}_s)f_j(\vec{X}_V)dV, \tag{3.13}$$

where $i,j = 1,2,3$. And position vectors $\vec{X}_s = (z_s, x_s, y_s)$ is three-dimensional, so are $\vec{X}'_s$ and $\vec{X}_V$.

The environment is invariant in the Y direction. So the Green's functions should be "stationary" in Y coordinates. That is:

$$G_{ji}(z_s, x_s, y_s; z'_s, x'_s, y'_s) = G_{ji}(z_s, x_s, y_s + \xi; z'_s, x'_s, y'_s + \xi); \tag{3.14}$$

$$H_{ji}(z_s, x_s, y_s; z'_s, x'_s, y'_s, \vec{n}_s(z_s, x_s)) = G_{ji}(z_s, x_s, y_s + \xi; z'_s, x'_s, y'_s + \xi, \vec{n}_s(z_s, x_s)). \tag{3.15}$$

So the Green's functions can be written as

$$G_{ji}(\vec{X}_s;\vec{X}'_s) = G_{ji}(z_s, x_s, y_s - y'_s; z'_s, x'_s), \tag{3.16}$$

and

$$H_{ji}(\vec{X}_s;\vec{X}'_s,\vec{n}_s) = H_{ji}(z_s, x_s, y_s - y'_s; z'_s, x'_s, \vec{n}_s(z_s, x_s)). \tag{3.17}$$

Apply Fourier Transform:

$$G_{ji}(z_s, x_s, y_s - y'_s; z'_s, x'_s) = \int_{-\infty}^{+\infty} \tilde{G}_{ji}(z_s, x_s; z'_s, x'_s, \vec{n}_s, k_y)e^{-ik_y(y_s - y'_s)}dk_y; \tag{3.18}$$

$$H_{ji}(z_s, x_s, y_s - y'_s; z'_s, x'_s, \vec{n}_s) = \int_{-\infty}^{+\infty} \tilde{H}_{ji}(z_s, x_s; z'_s, x'_s, \vec{n}_s, k_y)e^{-ik_y(y_s - y'_s)}dk_y; \tag{3.19}$$

$$u_j(z_s, x_s, y_s) = \int_{-\infty}^{+\infty} \tilde{u_j}(z_s, x_s; k'_y)e^{-ik'_y y_s}dk'_y. \tag{3.20}$$

Since the environment is independent of y coordinate, some simplification can be made:

$$\int\int_s H_{ji}(\vec{X}_s;\vec{X}'_s,\vec{n}_s)u_j(\vec{X}_s)ds$$

$$
\begin{aligned}
&= \int_c \int_{-\infty}^{+\infty} \int_{-\infty}^{+\infty} \tilde{H}_{ji}(z_s, x_s; z'_s, x'_s, \vec{n_s}, k_y) e^{ik_y y'_s} \tilde{u_j}(z_s, x_s; k'_y) \\
&\quad [\int_{-\infty}^{+\infty} e^{-iy_s(k_y+k'_y)} dy_s] dk_y dk'_y dl \\
&= 2\pi \int_c \int_{-\infty}^{+\infty} \tilde{H}_{ji}(z_s, x_s; z'_s, x'_s, \vec{n_s}, -k'_y) \tilde{u_j}(z_s, x_s; k'_y) e^{-ik_y y'_s} dk'_y dl. \qquad (3.21)
\end{aligned}
$$

Here we used the property of the delta function:

$$
\delta(x) = \frac{1}{2\pi} \int_{-\infty}^{+\infty} e^{ikx} dk. \qquad (3.22)
$$

Similarly,

$$
\begin{aligned}
&\int \int_s [G_{ji}(\vec{X_s}; \vec{X'_s}) t_j(\vec{X_s}; \vec{n_s})] ds \\
&= 2\pi \int_c \int_{-\infty}^{+\infty} \tilde{G}_{ji}(z_s, x_s; z'_s, x'_s, -k_y) \tilde{t_j}(z_s, x_s; \vec{n_s}, k_y) e^{-ik_y y'_s} dk_y dl. \qquad (3.23)
\end{aligned}
$$

Define

$$
\hat{u_i}(\vec{X'_s}) = \int_V G_{ij}(\vec{X'_s}; \vec{X_s}) f_j(\vec{X_V}) dV, \qquad (3.24)
$$

and apply Fourier Transform: $\frac{1}{2\pi} \int_{-\infty}^{+\infty} e^{ik_y y'_s} dy'_s$. Now Eq. (3.13) becomes:

$$
\begin{aligned}
&C_{ij} \tilde{u_j}(x'_s, z'_s; k_y) \\
&= 2\pi \int_c [\tilde{G_{ji}}(z_s, x_s; z'_s, x'_s, -k_y) \tilde{t_j}(z_s, x_s; \vec{n_s}, k_y) \\
&\quad - \tilde{H}_{ji}(z_s, x_s; z'_s, x'_s, \vec{n_s}, -k_y) \tilde{u_j}(z_s, x_s; k_y)] dl + \tilde{\hat{u}_i}(z'_s, x'_s; k_y). \qquad (3.25)
\end{aligned}
$$

Thus, the $2\frac{1}{2}$ dimensional problem has been reduced to a series of 2D problems with k_y as a parameter. So we can develop a $2\frac{1}{2}$-D model based on the existing 2D WI-BEM model. Additional elastic boundary conditions need to be incorporated into the BEM formulation. And the WI-DGM model used in the kernel and field computation must be capable of treating the full three-dimensional scenario. Such a model is developed and is the topic of the next section.

3.4 3-D DGM formulation

Schmidt and Glattetre [60] and Kim [39] developed 3-D DGM formulation in the cylindrical coordinate system. For WI-BEM approach, a Cartesian coordinate system is more suitable, so I developed a 3-D Cartesian DGM formulation. The outline of the formulation will be presented in this section. The detailed derivation is in Appendix A.

3.4.1 Homogeneous Solution

The displacement field can be described by a scalar potential and a vector potential:

$$\vec{u} = \nabla\phi(x,y,z) + \nabla \times \vec{\psi}(x,y,z), \tag{3.26}$$

where the vector displacement potential can be further expanded as:

$$\vec{\psi}(x,y,z) = \nabla \times (0,0,\Lambda) + (0,0,\psi_z). \tag{3.27}$$

Under such a representation, the wavefield is explicitly expressed as basic wave type components. ϕ corresponds to compressional wave; ψ_z corresponds to horizontally polarized shear wave (SH wave); Λ corresponds to the vertically polarized shear wave (SV wave).

The stresses relate to the displacement field as

$$\begin{cases} \sigma_{zz}(x,y,z) = \lambda(\frac{\partial u}{\partial x} + \frac{\partial v}{\partial y} + \frac{\partial w}{\partial z}) + 2\mu\frac{\partial w}{\partial z} = (\lambda+2\mu)\frac{\partial w}{\partial z} + \lambda(\frac{\partial u}{\partial x} + \frac{\partial v}{\partial y}), \\ \sigma_{zx}(x,y,z) = \mu(\frac{\partial w}{\partial x} + \frac{\partial u}{\partial z}), \\ \sigma_{zy}(x,y,z) = \mu(\frac{\partial w}{\partial y} + \frac{\partial v}{\partial z}). \end{cases} \tag{3.28}$$

For homogeneous part of the field, the displacement potentials satisfy the Helmholtz equations:

$$\begin{cases} (\nabla^2 + K_p^2)\phi(x,y,z) = 0, \\ (\nabla^2 + K_s^2)\Lambda(x,y,z) = 0, \\ (\nabla^2 + K_s^2)\psi_z(x,y,z) = 0, \end{cases} \tag{3.29}$$

where K_p is the compressional media wavenumber, and K_s the shear media wavenumber.

It can be shown (Appendix A) that the homogeneous solutions for the displacement potentials in the wavenumber domain are:

$$\begin{cases} \phi(k_x, z; k_y) = A^-(k_x, k_y)e^{-\alpha z} + A^+(k_x, k_y)e^{\alpha z}, \\ \psi_z(k_x, z; k_y) = B^-(k_x, k_y)e^{-\beta z} + B^+(k_x, k_y)e^{\beta z}, \\ \Lambda(k_x, z; k_y) = C^-(k_x, k_y)e^{-\beta z} + C^+(k_x, k_y)e^{\beta z}, \end{cases} \tag{3.30}$$

where $\alpha = \sqrt{k_x^2 + k_y^2 - k_p^2}$, and $\beta = \sqrt{k_x^2 + k_y^2 - k_s^2}$.

When α is imaginary, A^- is the amplitude of a down-going compressional plane wave of a particular direction; A^+ is the amplitude of the up-going compressional plane wave. Different wavenumber (k_x, k_y) corresponds to different horizontal directions. The process of Fourier transforming the potential from spatial domain $\phi(x, y, z)$ into wavenumber domain $\phi(k_x, k_y, z)$ is no more than decomposition of the complex wave field into a series of plane wave component. For plane waves, the derivative operations with respect to coordinates become simply a multiplication by some wavenumber dependent constants. Thus, differential equations are simplified to linear equations, which are much easier to solve.

Now we have represented the potentials in terms of unknown plane wave amplitudes, the displacement and stress fields can be represented by the same set of amplitudes through Eq. (3.26) and Eq. (3.28). The exact forms of these representation are given in Appendix A.

3.4.2 Source Field

Compressional Point Source

An explosive source in a homogeneous medium will not generate a shear wave. The compressional wave it generates has the displacement potential $\hat{\phi}(x, y, z)$ that satisfies

the following equation,

$$(\nabla^2 + k_p^2)\hat{\phi}(x,y,z) = -S_w\delta(x)\delta(y)\delta(z-z_s), \tag{3.31}$$

where S_w is the source strength. By Fourier transform the above equation, it is easy to show that the potential in the wavenumber domain is,

$$\hat{\phi}(k_x,z;k_y) = \frac{S_w}{8\pi^2\alpha}e^{-\alpha|z-z_s|}. \tag{3.32}$$

Point Force Source of Arbitrary Direction

Assume the source is (F_x, F_y, F_z), define

$$\begin{cases} \phi_0(k_x,z;k_y) = -\frac{1}{\rho\omega^2}\frac{1}{8\pi^2\alpha}e^{-\alpha|z-z_s|}, \\ \psi_0(k_x,z;k_y) = -\frac{1}{\rho\omega^2}\frac{1}{8\pi^2\beta}e^{-\beta|z-z_s|}. \end{cases} \tag{3.33}$$

The displacement potentials for the source field are

$$\begin{cases} \phi(x,y,z) = \vec{F} \bullet \nabla\phi_0(x,y,z), \\ \vec{\psi}(x,y,z) = \nabla \times (-F_x\psi_0(x,y,z), -F_y\psi_0(x,y,z), -F_z\psi_0(x,y,z)). \end{cases} \tag{3.34}$$

So,

$$\phi(k_x,z;k_y) = \frac{ik_xF_x}{\rho\omega^2}\frac{1}{8\pi^2\alpha}e^{-\alpha|z-z_s|} + \frac{ik_yF_y}{\rho\omega^2}\frac{1}{8\pi^2\alpha}e^{-\alpha|z-z_s|} + \frac{F_z}{\rho\omega^2}sign(z-z_s)\frac{1}{8\pi^2}e^{-\alpha|z-z_s|}, \tag{3.35}$$

$$\begin{aligned} \vec{\psi}(k_x,z;k_y) \;=\; & \{\vec{e}_x[0 + \beta sign(z-z_s)F_y - ik_yF_z] \\ & + \vec{e}_y[-\beta sign(z-z_s)F_x + 0 + ik_xF_z] \\ & + \vec{e}_z[ik_yF_x - ik_xF_y + 0]\}\frac{1}{\rho\omega^2}\frac{1}{8\pi^2\beta}e^{-\beta|z-z_s|}. \end{aligned} \tag{3.36}$$

3.4.3 Global Equation

So far in this section, we have represented the displacement and stress fields in terms of a series of plane waves, whose amplitudes are yet to be determined. Thus, in each layer, the displacement and stress fields can be written as:

$$\begin{bmatrix} \omega \\ u \\ v \\ \sigma_{zz} \\ \sigma_{zx} \\ \sigma_{zy} \end{bmatrix} = [A][B] + [R]. \tag{3.37}$$

In the equation above, [B] is the aggregate of the unknown amplitudes of the plane waves;

$$[B] = \begin{bmatrix} A^- \\ SC^- \\ B^- \\ A^+ \\ SC^+ \\ B^+ \end{bmatrix}; \tag{3.38}$$

[A] is a wavenumber dependent matrix that relates the plane wave amplitudes to the homogeneous solution of the displacement and stress fields; [R] is the field contribution by physical sources.

To solve for the unknown plane wave amplitudes, we consider the boundary conditions. In the spatial domain, the boundary condition is the constraint that the displacements and stresses must be continuous across the boundaries. For a boundary of arbitrary shape, this doesn't mean that the wavenumber transforms of the displacements and stresses should be continuous across the boundaries. In other words, plane waves traveling at different directions might be coupled at the boundary. In that case, decompositing the wavefield into plane wave components does not

simplify the solution of the problem, although the equation of motions are simplified.

Fortunately, here we are dealing with **horizontally stratified** media. All boundaries are planes perpendicular to the Z axis. In this kind of scenario, plane wave traveling at different directions in a layer are decoupled. So we can solve for the unknown plane wave amplitudes at each horizontal wavenumber pair (k_x, k_y) separately.

The plane wave amplitudes in all layers have to be solved simultaneously. To do that, a global equation is set up. Assume there are N layers,

$$\begin{bmatrix} [A_{1,l}] & [-A_{2,u}] & & \\ & [A_{2,l}] & [-A_{3,u}] & \\ & & & \\ & & [A_{N-1,l}] & [-A_{N,u}] \end{bmatrix} \bullet \begin{bmatrix} B_1 \\ B_2 \\ \vdots \\ B_N \end{bmatrix} = \begin{bmatrix} R_{2,u} \\ R_{3,u} \\ \vdots \\ R_{N,u} \end{bmatrix} - \begin{bmatrix} R_{1,l} \\ R_{2,l} \\ \vdots \\ R_{N-1,l} \end{bmatrix}. \tag{3.39}$$

We can see that the global matrix at the left hand side is rather sparse; only some sub-matrices near axis are populated. B_i is a vector with elements correspond to the unknown plane wave amplitudes in layer i. The exact forms are shown in Appendix A.

After solving the amplitudes of various plane waves in each layer, the corresponding displacement and stress fields can be calculated following Eq. (3.37). A summation of the effects of these plane waves at various direction (inverse Fourier transform) will give the total field in the spatial domain.

Chapter 4

Numerical Simulations of 2-1/2D Facet Reverberation

4.1 A Sanity Check: Comparison with Analytic Solution

To make sure our model and code work properly, comparison with other independent solution is in order. As stated earlier, no existing model is capable of dealing with the three dimensional scattering with elastic effect. So the only thing we can do is to reduce the complexity of the problem we deal with and compare with some other method that is capable of solving that reduced problem.

A very simple environment is chosen, where an elastic cylinder is submerged in a homogeneous elastic environment. A line array parallel with the cylinder generates an acoustic beam whose main lobe lies between 35^0 and 54.6^0 with the axis. It is worthwhile to emphasize that the beam pattern is rotational symmetric (Fig. 4-1). We derive an analytical solution for this problem and compare it with numerical solutions from our model.

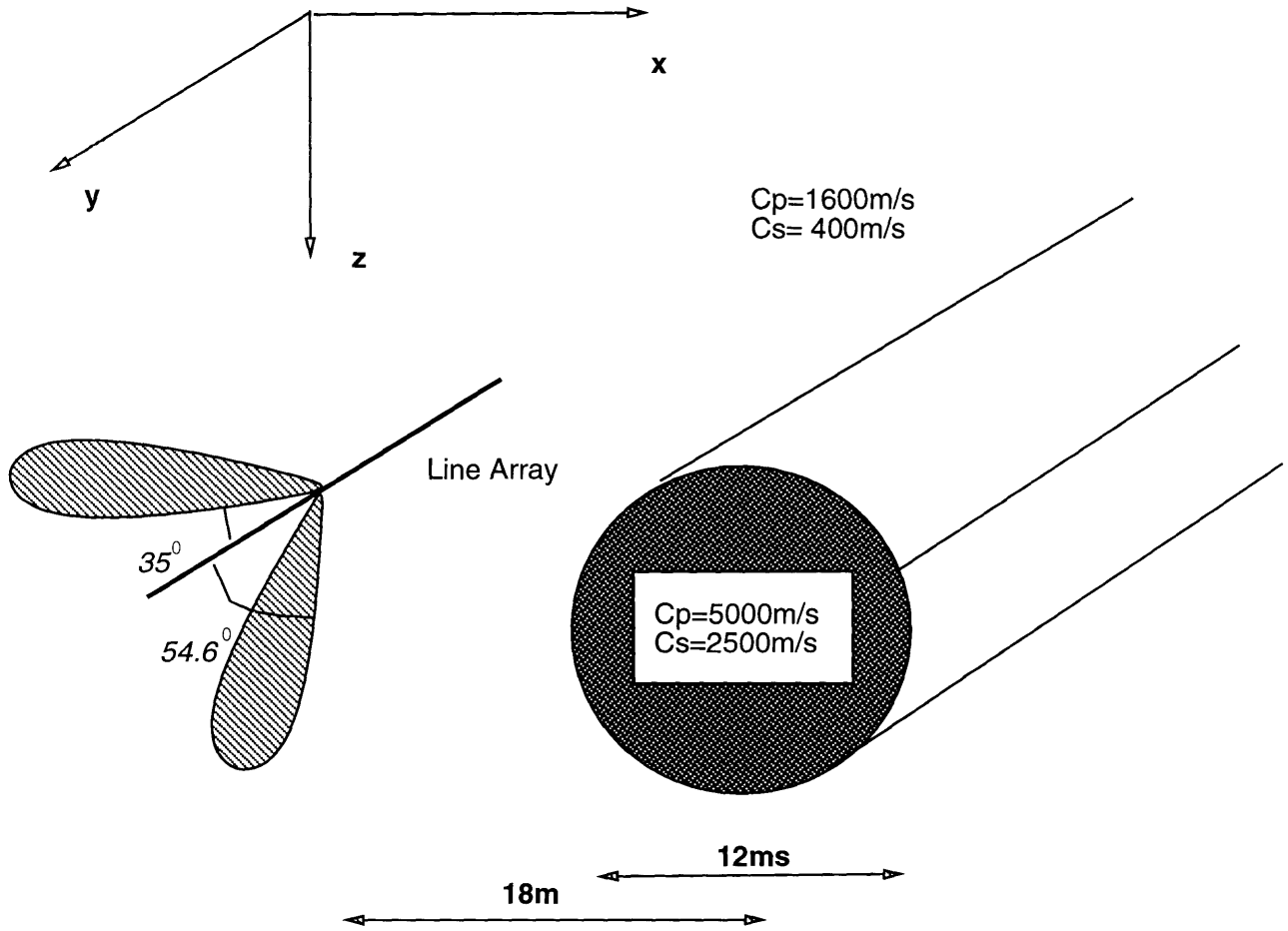

Figure 4-1: Geometry of the Test Case. A basalt cylinder is submerged in the silt. A line array parallel to the cylinder generates sound waves that insonifies on the cylinder.

4.1.1 The Analytic Solution

Naturally, for this problem, cylindrical coordinates should be used. The governing equation for the homogeneous displacement field $\vec{U}(r,\theta,z,t)$ is :

$$(\lambda+2\mu)\nabla\nabla\bullet\vec{U}-\mu\nabla\times\nabla\times\vec{U}=\rho\frac{\partial^2\vec{U}}{\partial t^2}. \tag{4.1}$$

The displacement field is assumed to be harmonic:

$$\vec{U}(r,\theta,z,t)=\vec{u}(r,\theta,z)e^{-i\omega t}. \tag{4.2}$$

The displacement field can be represented by three potential fields $\phi(r,\theta,z)$, $\Lambda(r,\theta,z)$ and $\psi(r,\theta,z)$:

$$\vec{u}(r,\theta,z)=\nabla\phi+\nabla\times\nabla\times(0,0,\Lambda)+\nabla\times(0,0,\psi), \tag{4.3}$$

which satisfy Helmholtz equations:

$$\begin{cases}(\nabla^2+K_p^2)\phi(r,\theta,z)=0;\\(\nabla^2+K_s^2)\Lambda(r,\theta,z)=0;\\(\nabla^2+K_s^2)\psi_z(r,\theta,z)=0.\end{cases} \tag{4.4}$$

In the equation above, K_p and K_s are media compressional and shear wavenumber, respectively.

Now, we transform the quantities:

$$g(r,\theta,z)=\sum_{m=-\infty}^{\infty}\int_{-\infty}^{\infty}\tilde{g}(r,m,k_z)e^{ik_z z}dk_z, \tag{4.5}$$

where k_z is the wavenumber measured in the axial direction. g can be any one of ϕ, ψ, Λ, $\vec{u}$ or σ.

After the transform, the Helmholtz equations will separate and can be solved easily. The solutions are as follows

$$\begin{cases} \tilde{\phi}(r,m,k_z) = A^+ H_m^{(1)}(h_r r) + A^- H_m^{(2)}(h_r r); \\ \tilde{\Lambda}(r,m,k_z) = B^+ H_m^{(1)}(k_r r) + B^- H_m^{(2)}(k_r r); \\ \tilde{\psi}(r,m,k_z) = C^+ H_m^{(1)}(k_r r) + C^- H_m^{(2)}(k_r r). \end{cases} \tag{4.6}$$

h_r and k_r are radial wavenumbers for compressional and shear waves, respectively:

$$\begin{cases} h_r^2 = k_p^2 - k_z^2, \\ k_r^2 = k_s^2 - k_z^2. \end{cases} \tag{4.7}$$

In Eq. (4.6), the Hankel functions of the first kind $H_m^{(1)}(h_r r)$ and $H_m^{(1)}(k_r r)$ represent outgoing compressional waves and shear waves, respectively. And Hankel functions of the second kind $H_m^{(2)}(h_r r)$ and $H_m^{(2)}(k_r r)$ represent incoming waves toward the axis. [1] $A^+, A^-, B^+, B^-, C^+, C^-$ are unknown amplitudes to be determined that are functions of k_z.

Notice that, unlike the horizontally stratified media case, where we Fourier transformed the Helmholtz equation with respect to X and Y, here we perform the transform with respect to Z. This is due to the geometry of the boundary. In the horizontally layered case, the interface between layers are planes. k_x and k_y are continuous across the boundaries. In the case where the cylinder is submerged in the horizontally stratified media (Fig. 3-1), the only wavenumber component that remains constant across all boundaries is k_y, so Fourier transform with respect to Y was performed. Here in our scenario, Z is the only direction along which environment stays unchanged. So, only k_z is continuous across boundary between layers with different elastic properties. Fourier transform with respect to Z should be performed.

Now, to complete the problem and solve for the unknown amplitudes of the various wave components, we state the boundary condition.

The boundary condition is that the displacement and stress components should be continuous across the boundaries. To link the boundary conditions to the un-

[1] Which kind of the Hankel functions represent outgoing or incoming waves depends on the choice of the time dependency representation. Here, time dependency is assumed to be $e^{-i\omega t}$. If we reverse the sign in the exponential, the role of the two kinds of Hankel functions will be reversed.

known amplitudes, we can express the displacements and stresses in terms of the displacement potentials:

$$\begin{cases} \tilde{u_r}(r,m,k_z) = \frac{\partial\tilde{\phi}}{\partial r} + \frac{im}{r}\tilde{\psi} + \frac{ik_z}{K_s}\frac{\partial\tilde{\Lambda}}{\partial r}, \\ \tilde{u_\theta}(r,m,k_z) = \frac{im}{r}\tilde{\phi} - \frac{\partial\tilde{\psi}}{\partial r} - \frac{mk_z}{K_s r}\tilde{\Lambda}, \\ \tilde{u_z}(r,m,k_z) = ik_z\tilde{\phi} + \frac{k_r^2}{K_s}\tilde{\Lambda}, \end{cases} \tag{4.8}$$

and

$$\begin{cases} \tilde{\sigma_{rr}}(r,m,k_z) = -\lambda K_p^2\tilde{\phi} + 2\mu(\frac{\partial^2\tilde{\phi}}{\partial r^2} - \frac{im}{r^2}\tilde{\psi} + \frac{im}{r}\frac{\partial\psi}{\partial r} + \frac{ik_z}{K_s}\frac{\partial^2\tilde{\Lambda}}{\partial r^2}), \\ \tilde{\sigma_{r\theta}}(r,m,k_z) = \mu[\frac{2im}{r}(-\frac{\tilde{\phi}}{r} + \frac{\partial\tilde{\phi}}{\partial r}) - \frac{m^2}{r^2}\tilde{\psi} + \frac{1}{r}\frac{\partial\tilde{\psi}}{\partial r} - \frac{\partial^2\tilde{\psi}}{\partial r^2} + \frac{2mk_z}{K_s r}(\frac{\tilde{\Lambda}}{r} - \frac{\partial\tilde{\Lambda}}{\partial r})], \\ \tilde{\sigma_{rz}}(r,m,k_z) = \mu[2ik_z\frac{\partial\tilde{\phi}}{\partial r} - \frac{mk_z}{r}\tilde{\psi} + \frac{k_r^2-k_z^2}{K_s}\frac{\partial\tilde{\Lambda}}{\partial r}]. \end{cases} \tag{4.9}$$

The Treatment of the Source

Ricks [58] developed the source field solution for the ring forces. It could be in radial, circumferential or axial direction. Here we use a point explosive source located at $(r_0, \theta_0 = 0, z_0 = 0)$. The equations for the source potentials are

$$\begin{cases} \frac{1}{r}\frac{\partial}{\partial r}[r\frac{\partial}{\partial r}\hat{\phi}(r,\theta,z)] + \frac{1}{r^2}\frac{\partial^2}{\partial\theta^2}\hat{\phi}(r,\theta,z) + \frac{\partial^2}{\partial z^2}\hat{\phi}(r,\theta,z) = -S_w\delta(r-r_0)\delta(\theta)\delta(z); \\ \hat{\psi}(r,\theta,z) = 0; \\ \hat{\Lambda}(r,\theta,z) = 0. \end{cases} \tag{4.10}$$

By applying the transforms $\frac{1}{2\pi}\int_{-\pi}^{\pi} e^{-im\theta}d\theta$ and $\frac{1}{2\pi}\int_{-\infty}^{\infty} e^{-ik_z z}dz$ on Eq. (4.10), we get

$$\begin{cases} \frac{1}{r}\frac{\partial}{\partial r}[r\frac{\partial}{\partial r}\tilde{\hat{\phi}}(r,m,k_z)] - \frac{m^2}{r^2}\tilde{\hat{\phi}}(r,m,k_z) + h_r^2\tilde{\hat{\phi}}(r,m,k_z) = -\frac{S_w}{4\pi^2}\delta(r-r_0); \\ \tilde{\hat{\psi}}(r,m,k_z) = 0; \\ \tilde{\hat{\Lambda}}(r,m,k_z) = 0. \end{cases} \tag{4.11}$$

Because the source is explosive, only compressional waves are generated. So the shear potentials are all zero. The resulting compressional potentials can be solved to

be:

$$\tilde{\hat{\phi}}(r,m,k_z) = \begin{cases} \frac{S_w}{4\pi^2} J_m(h_r r_0) H_m^{(1)}(h_r r) & \text{for } r > r_0; \\ \frac{S_w}{4\pi^2} H_m^{(1)}(h_r r_0) J_m(h_r r) & \text{for } r < r_0. \end{cases} \tag{4.12}$$

From this source generated potential, and using the relationship between the potentials and the displacements and stresses, we get the source influence on the boundary. Those are the discontinuities of the displacements and the stresses of the homogenous field (Right Hand Side).

To this point, we have obtained a system of linear equations for A^+, A^-, B^+, B^-, C^+ and C^-. Now we can proceed to solve for these amplitudes of the various wave types.

The Result of the Analytic Solution

To produce the cone-like beam, the wavenumber spectrum of the source field was filtered such that the resulting beam form a 45^0 angle with the cylinder axis.

The scattered field (incoming field excluded) is calculated in the zero azimuth plane where the source located. The result is shown in Fig. 4-2. Two wave types are clearly present.

Simple calculations can be performed to identify these wave types appearing in the scattered field. The incoming beam is compressional and is 45^0 to the cylinder axis. So the axial wavenumber is

$$k_z^{in} = K_p \cos 45^0. \tag{4.13}$$

The axial wavenumber k_z^{scat} for any scattered wave should be the same as that of the incoming wave. So the scattered compressional and shear wave will have different radial wavenumber:

$$\begin{cases} (h_r^{scat})^2 = K_p^2 - (K_z^{scat})^2 = K_p^2(1 - cos45^0); \\ (k_r^{scat})^2 = K_s^2 - (K_z^{scat})^2 = K_s^2 - K_p^2 cos^2 45^0. \end{cases} \tag{4.14}$$

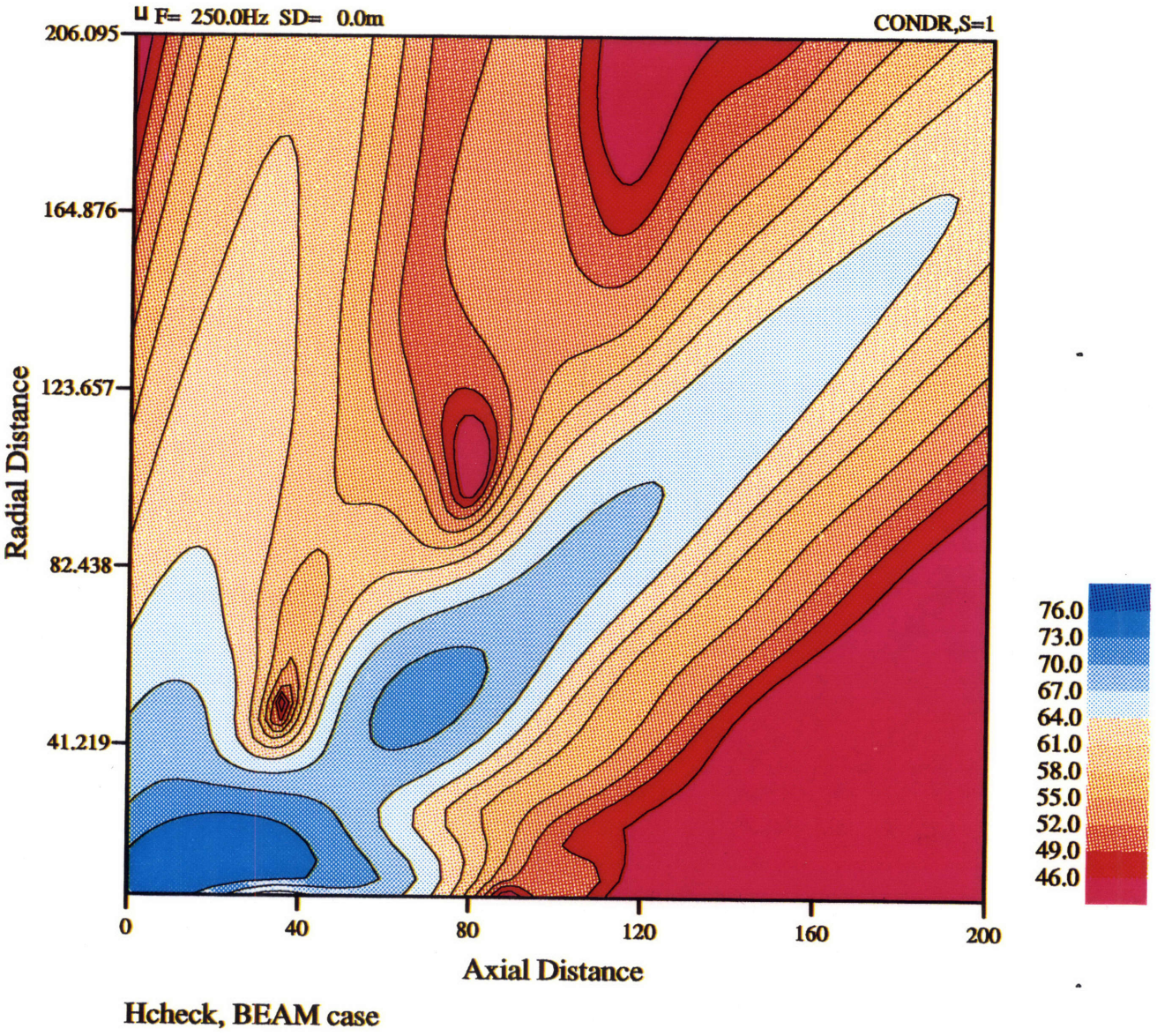

Figure 4-2: The Scattered Field in the Zero Azimuth Plane Calculated Using Analytic Solution

The most strongly scattered compressional wave is at 45^0 to the cylinder (the specular scattering). While the direction of the shear wave form an angle with the cylinder which satisfies:

$$\alpha^{shear} = \arccos(\frac{K_p}{K_s} cos45^0) = \arccos(\frac{C_s}{C_p\sqrt{2}}) = \arccos(\frac{400}{1600 * \sqrt{2}}) = 79.82^0. \quad (4.15)$$

From Fig. 4-2, we see the direction of the two strong wave types are approximately around those two angles. This confirms that for this compressional insonification case, both compressional and shear scattering waves are excited.

4.1.2 WI-BEM Simulation

The 2-1/2 D WI-BEM is very computational intensive. So we shall be careful to choose the scenario in the testing stage, at least. To reduce the computational intensity, we want to reduce the grid size for the kernel computation. That is, reduce the number of k_x and k_y samples.

Among the two, the number of k_y samples is more vital. As described in the last chapter, the way we approach the 2-1/2D problem is to reduce it to a series of two dimensional problems, one for every k_y value. So, for each k_y sample, a miniature of two dimensional WI-BEM problem has to be solved from scratch. All the computations of influence matrices, nodal values and scattered field have to be done again. But it is a different story for k_x samples. Since the computation and integration of the k_x samples are separated for the three parts. Even if a large number of k_x samples are required for the scattered field computation, we only has to do that for the last part. The most time-consuming influence matrices computation can be performed using limited k_x samples.

Thus, it is desired to use small number of k_y samples. First, we will use as coarse a sampling rate as possible. But it has a lower limit associated with the maximum axial distance of the scattered field we want to compute. The other resort is to reduce the extent of the integration on k_y. From the first glance, the range of integration is

dictated by the desired resolution of scattered field in Y direction. But fortunately we can do better.

We notice that in the 2-1/2 D problem, there is no mechanism to destroy the k_y continuity. If a part of the k_y wavenumber spectrum of the source is zero, it will still be zero in the scattered field. Thus, by confining the extent of k_y spectrum of the source, we can greatly reduce the number of k_y samples need to be computed.

As evident in Fig. 4-3, for a fixed k_y, all possible directions of the acoustic beams form a cone surface. So, for a narrow range of k_y, possible directions of beams will be confined by two closely spanned cones. That is why we choose the source field in Fig. 4-1.

We use Cartesian coordinate for WI-BEM calculation of the problem, where Y axis is aligned with the cylinder axis. And Z axis is chosen such that the depth' of both the cylinder axis and the source is zero. So the coordinates of the source is $(0, 0, 0)$, while that of the cylinder axis is $(x = 18m, z = 0)$.

First, to make sure we did generate the desired beam pattern, the background field of normal stress and its wavenumber spectrum in the $Z = 0$ plane is calculated (Fig. 4-4 and Fig. 4-5). Essentially, this is how the field would look like without the facet scatterer (cylinder).

Before we go into the details of these results, it is worthwhile to compute some benchmark wavenumbers for future reference.

In Fig. 4-3, it is shown that all propagating P-waves are confined within a cone, and it is similar for the S-wave, just the confining cone is bigger since the shear media wavenumber is larger. Mapped onto the $k_x - k_y$ plane, we get Fig. 4-6. All the propagating P-waves in the outer medium have wavenumbers within two center lines (P-P). Outside, P-waves become evanescent. Propagating S-waves is confined between the two outer lines (S-S). Outside these two lines, all waves become evanescent.

It is noted that the lines are inward tilted. The reason can be seen from

$$\begin{cases} k_z^p = \sqrt{K_p^2 - k_y^2 - k_x^2}; \\ k_z^s = \sqrt{K_s^2 - k_y^2 - k_x^2}. \end{cases} \tag{4.16}$$

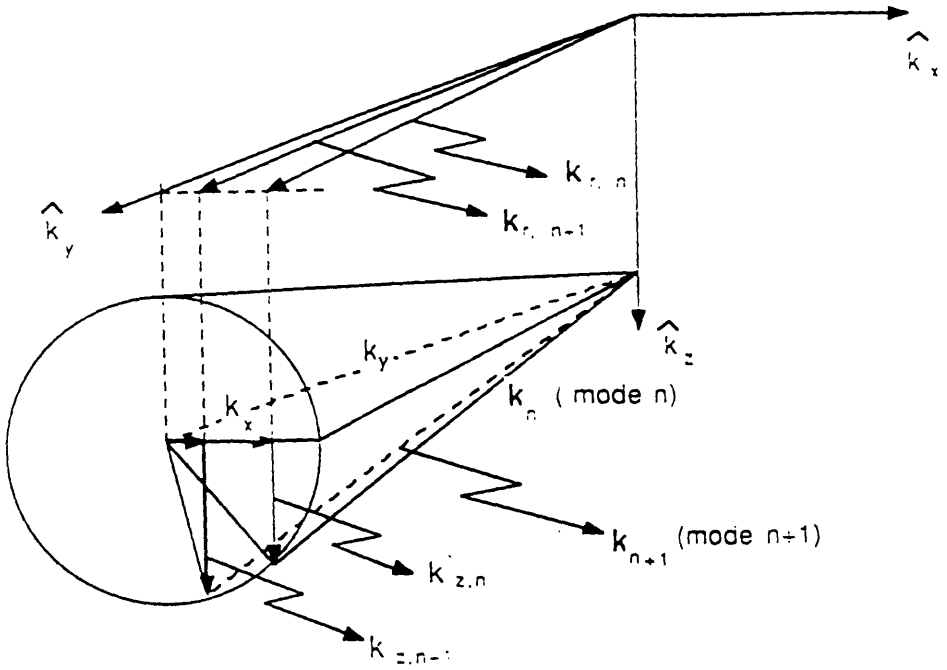

$$k^2 = k_x^2 + k_y^2 + k_z^2 \qquad k \text{ is } k_p \text{ or } k_s$$

for mode n, $k_{z,n}$ is a constant,

$$k_{x,n}^2 + k_y^2 = k_{r,n}^2 = k^2 - k_{z,n}^2$$

when $k_y < k_{r,n}$, $k_{x,n}$ is real,

the n' th mode exists.

when $k_y > k_{r,n}$ $k_{x,n}$ is imaginary,

the n'th mode is cut off.

Figure 4-3: The Three Dimensional Geometry of the Wavenumber Vectors in a Waveguide

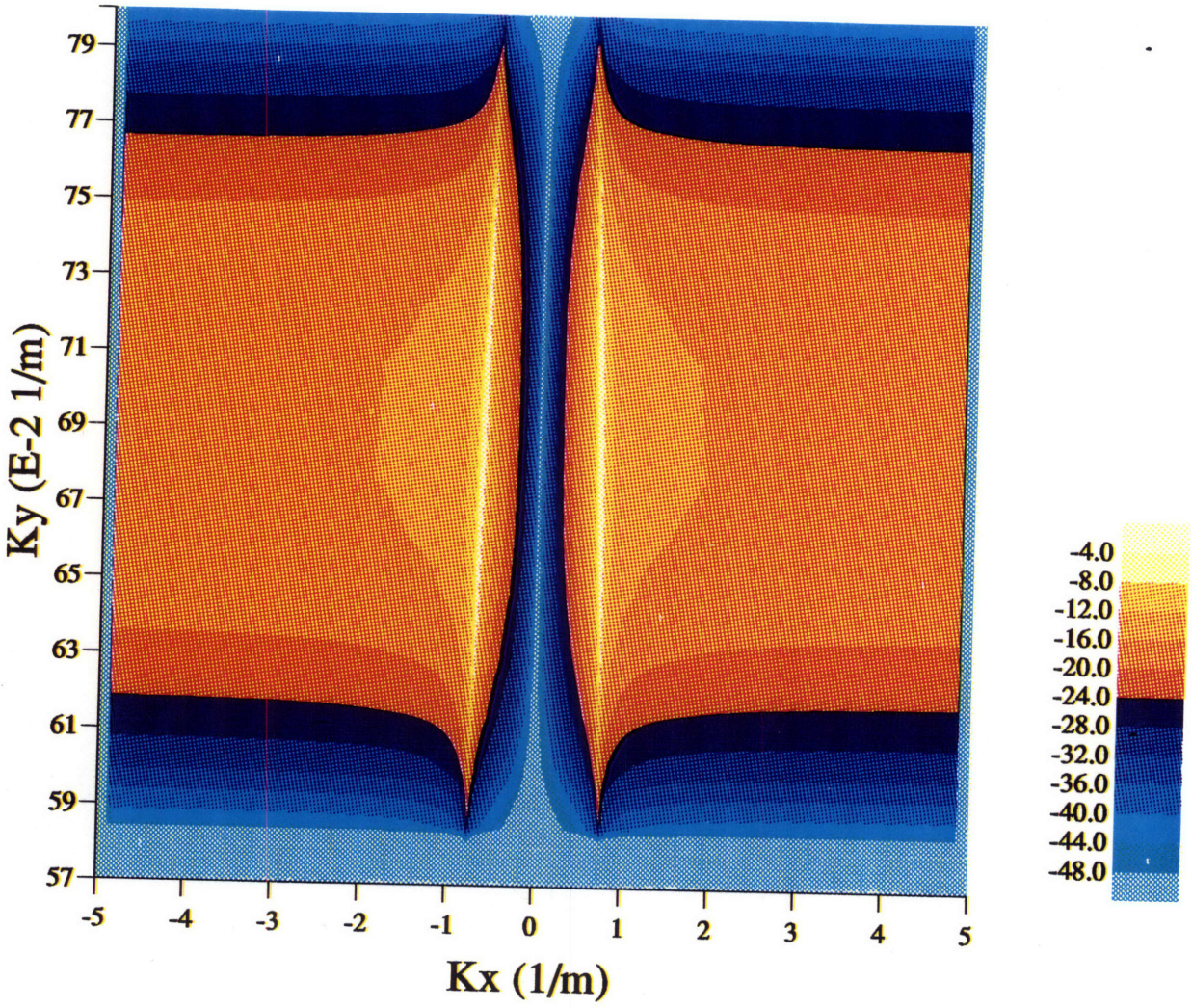

Figure 4-4: Source Normal Stress Wavenumber Spectrum in the Z=0 plane, calculated by WI-BEM

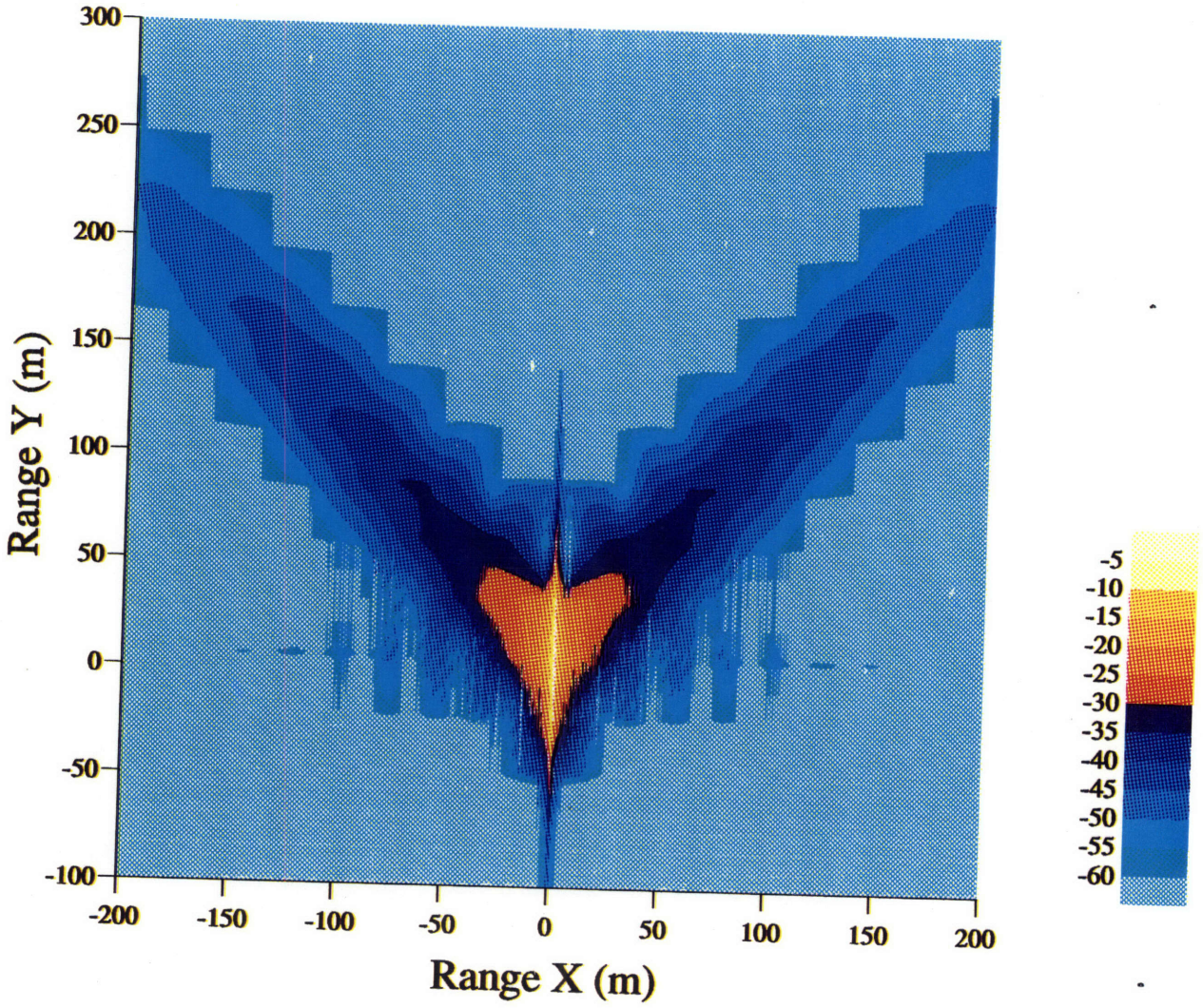

Figure 4-5: Source Normal Stress Field in the Z=0 plane, calculated by WI-BEM

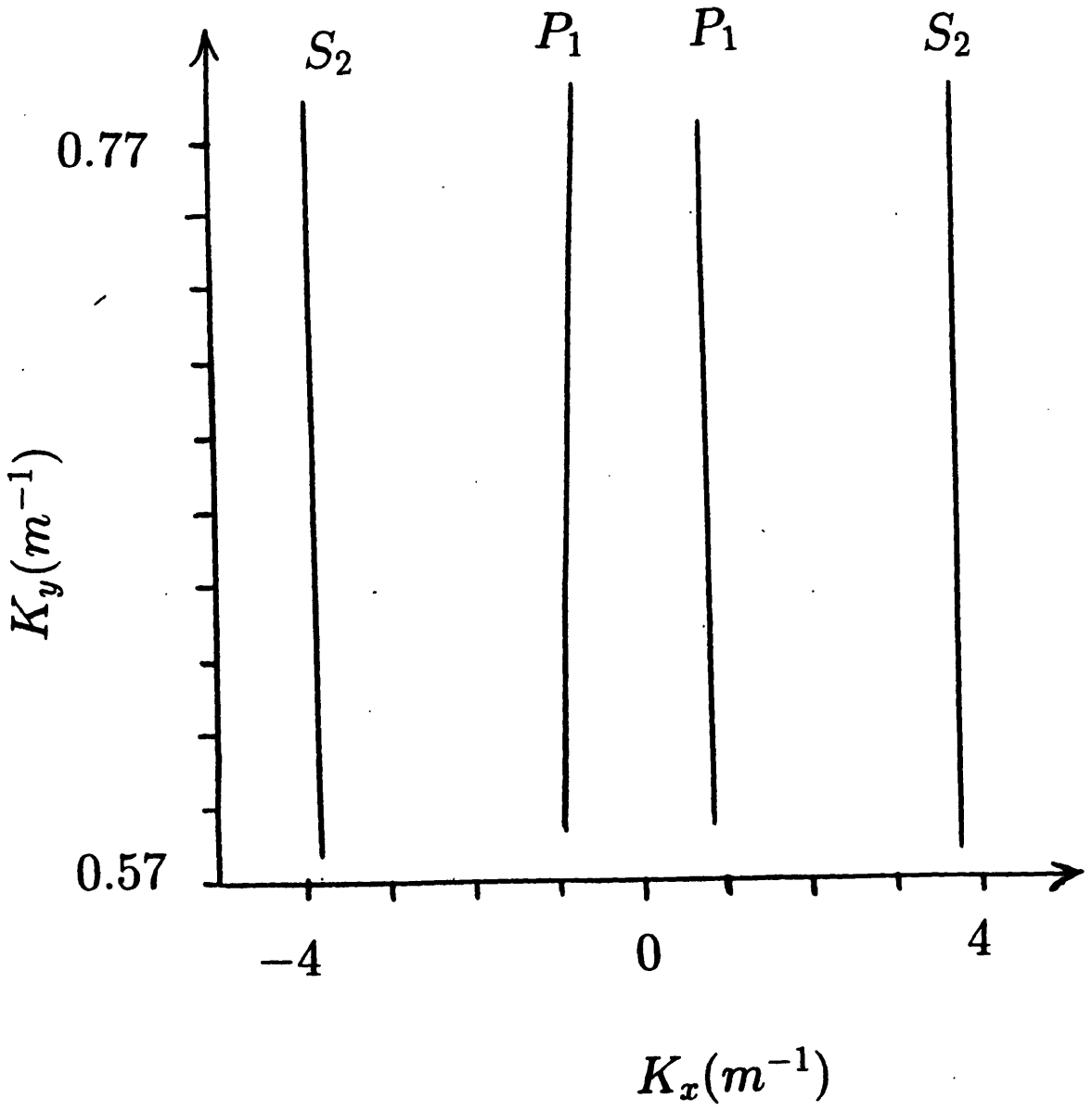

Figure 4-6: The Benchmarks of the Wavenumbers for the Outer Medium

The bigger k_y is, the smaller the maximum value of k_x is needed to keep k_z real.

Physically, we anticipate the source field on the Z=0 plane being a cut through the center of the cone. That is exactly shown in Fig. 4-5. Two beams of 45^0 with the Y axis is present. One traveling towards the cylinder, which located at $12m \leq X \leq 24m$. The other traveling away from the cylinder. On the plot of the kernel (Fig. 4-4), it is evident that only the compressional wave is present, which is what we anticipated with the explosive source.

In Fig. 4-5, the main beams in 45^0 are outlined by stair-line contour. They are caused by the coarse sample rate in k_y direction. As stated earlier, it is very expensive to compute new k_y values. Only 16 samples are calculated in this case. Also present in Fig. 4-5 are some thin lines. They are the aliases caused by the relative steep cut off in k_x and k_y direction.

Fig. 4-7 and Fig. 4-8 show the scattered normal stress field and its wavenumber spectrum on the $Z = 0$ plane. Again, it should be emphasized that the incoming field is excluded in these figures. If hydrophones are deployed in that plane, what they receive would be the sum of the scattered field shown here and the incoming field shown in Fig. 4-5.

On the scattered kernel plot (Fig. 4-7), several wave components are present. By far the strongest one is the P-wave traveling in the forward direction. This is the wave component that creates the "shadow zone" behind the cylinder. On the field plot (Fig. 4-8), it can be seen that this wave component overlaps with the forward traveling incoming field in Fig. 4-5. They more or less canceled out and create a relatively "quiet" zone behind the cylinder.

Now, let's return to Fig. 4-7. Though much weaker than the forward traveling P-wave, S-wave and P-wave traveling backward from the cylinder can be seen. On Fig. 4-8, we can see the backward traveling P-wave at 45^0 and the S-wave at 80^0 with the Y-axis. This agrees with the result of the analytic solution and our analysis in the last subsection.

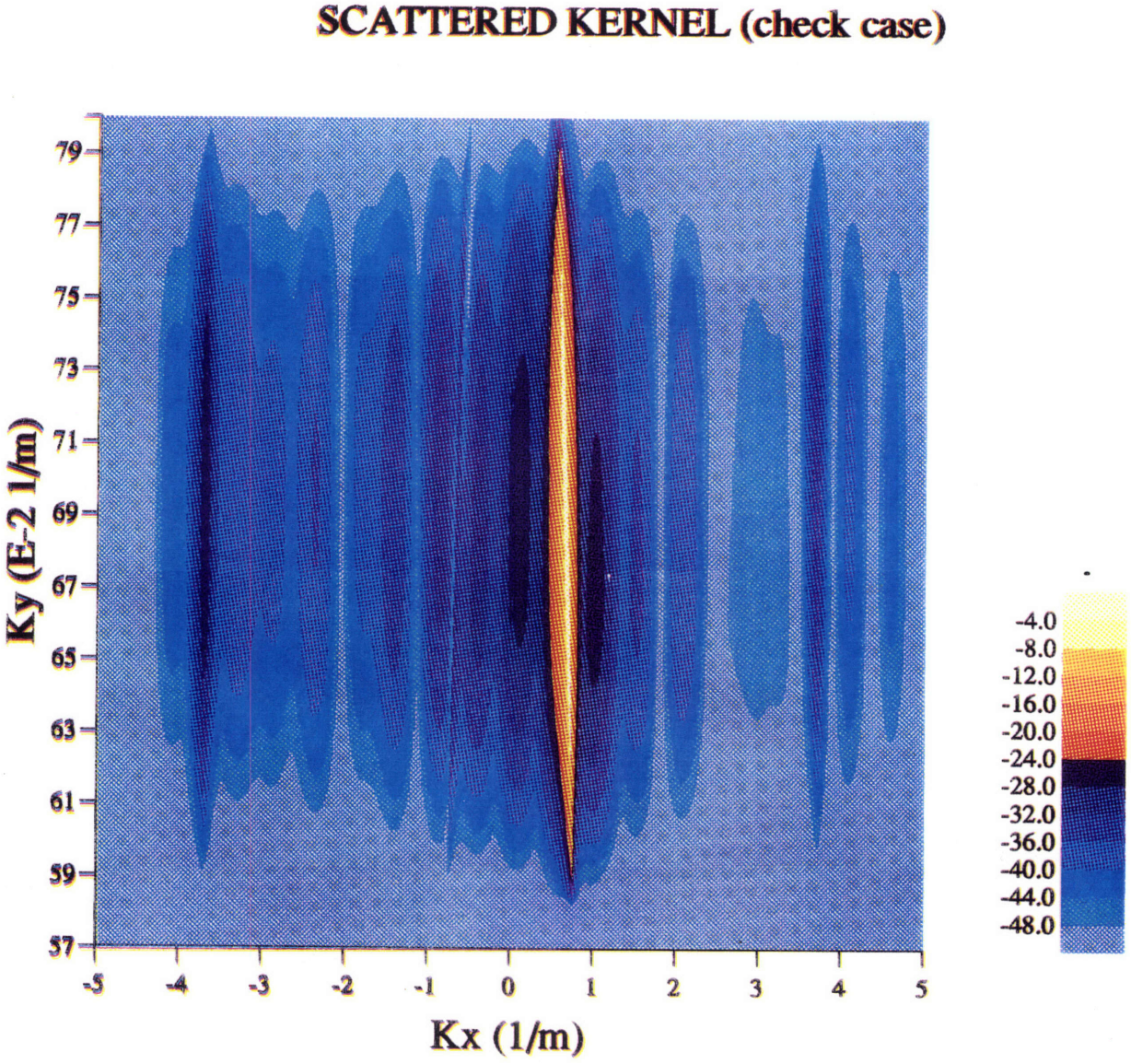

Figure 4-7: Scattered Normal Stress Kernel in the Z=0 plane, calculated by WI-BEM

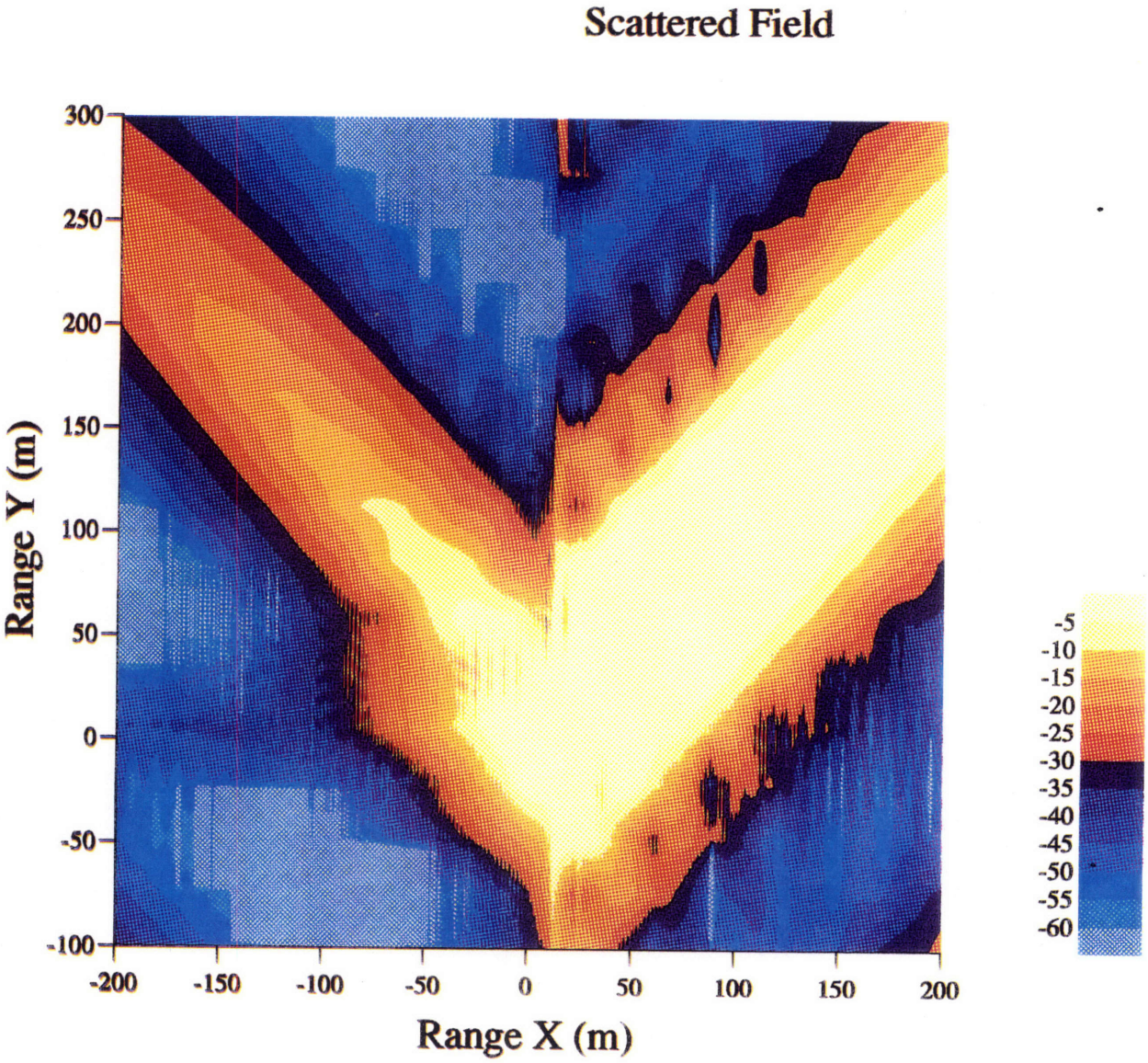

Figure 4-8: Scattered Normal Stress Field in the Z=0 plane, calculated by WI-BEM

4.2 Sediment Covered Ridge: Wave Type Conversion

Now that we have checked our 2-1/2D model and code, next we can use it to solve a much more realistic scenario. The environment is shown in Fig. 4-9. The sea bed consists of two layers, a 10-meter thick slower sediment layer overlays on top of the faster rock bottom. To investigate the effects of elasticity on the discrete scattering, a half cylinder ridge consists of rock protrude into the sediment layers. This destroys the environmental invariance along X direction and plays the role of the facet scatterer.

The source is 50m above the water column/sediment interface and 50m away horizontally form the cylinder axis. The source generates P-wave, and as in the last section, the beam pattern is confined between two cone surfaces. As before, this beam pattern is chosen to reduce the number of k_y samples required.

4.2.1 The Background Field

First, we remove the ridge and calculate the normal stress field in the plane 0.2 meters above the water column/sediment interface. It should be emphasized that this is not the source generated field in a homogeneous medium. The acoustic wave reflects from the first interface, and part of energy penetrates into the sediment and encounter the sediment/hard bottom interface and reflects and penetrates again, ...

Actually, some modes are excited in the sediment layer [2]. Because the P-wave speed in the water column is slower than that of the sediment, all of these modes leak into the water column. So we shall be able to notice these modes from the receiver array. For a particular k_y, these different mode corresponds to different directions of propagation. (Fig. 4-3)

The normal stress field in the horizontal plane 0.2 meters above the water column/sediment interface and its wavenumber spectrum are shown in Fig. 4-10 and Fig. 4-11.

[2] some of them might be S-wave modes

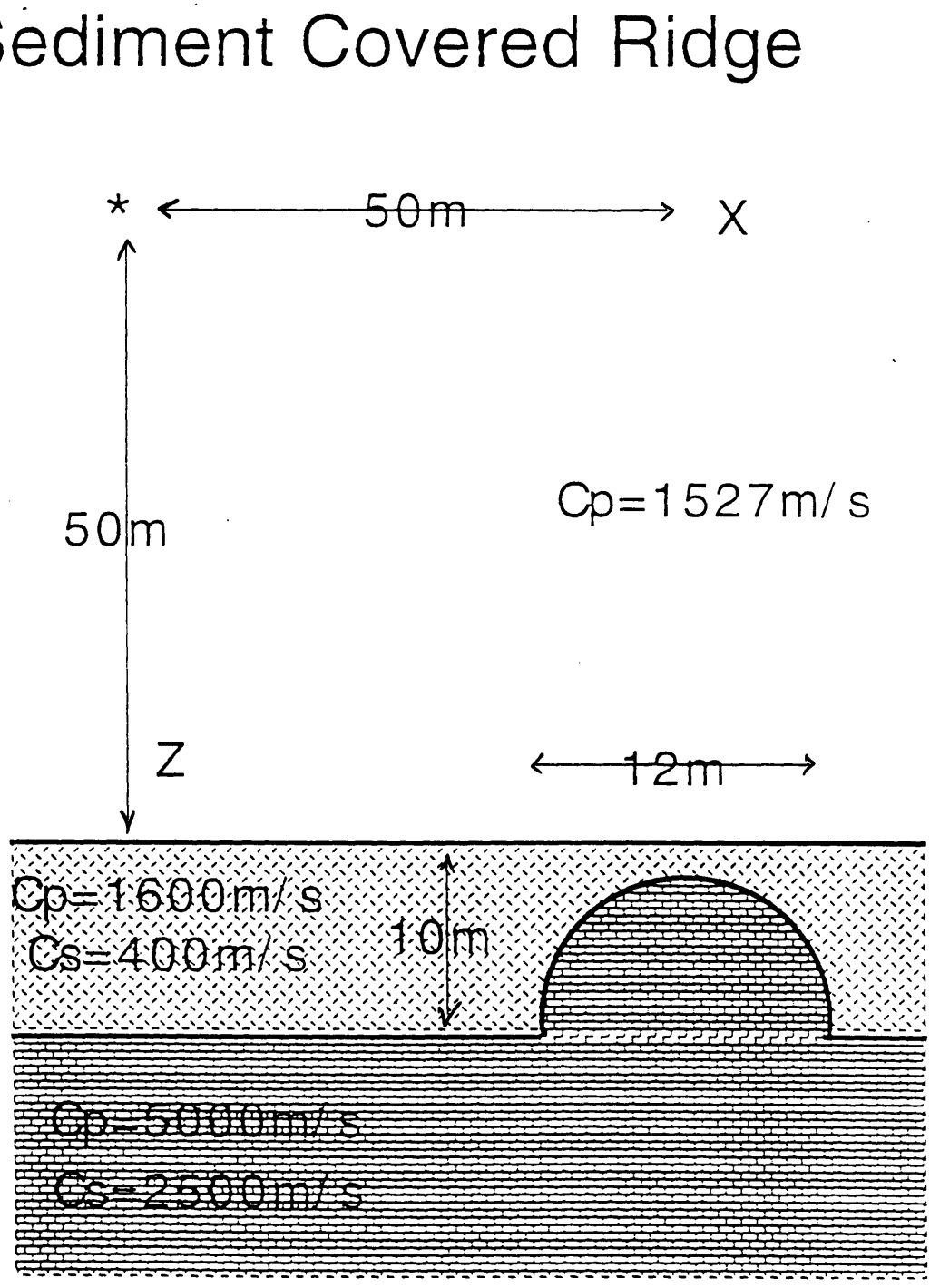

Figure 4-9: The Environment and Geometry of the Sediment Covered Ridge Case

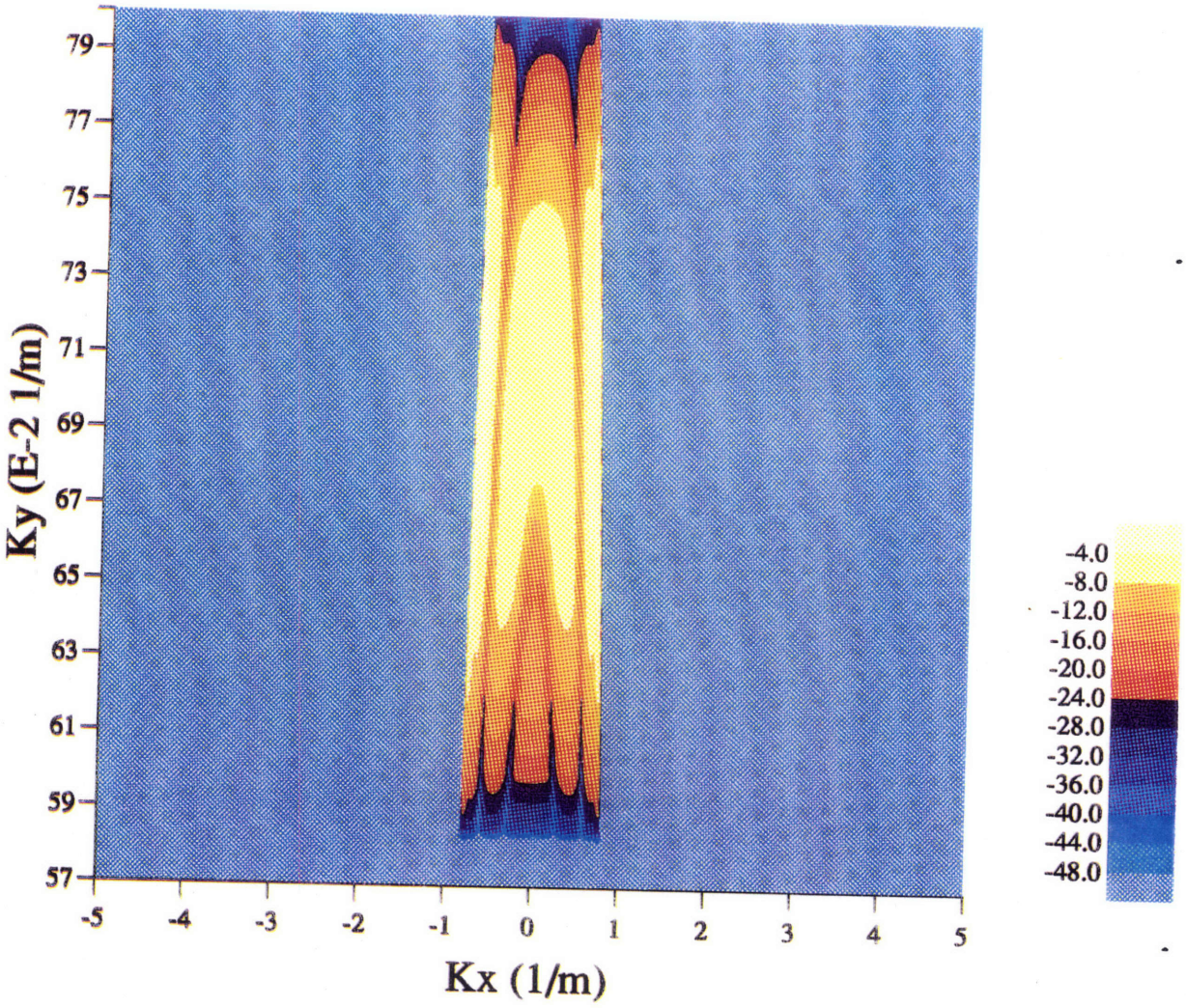

Figure 4-10: Background Pressure Wavenumber Spectrum in the Submerged Case, Received in the Plane 0.2 meters above the Water Column/Sediment Interface

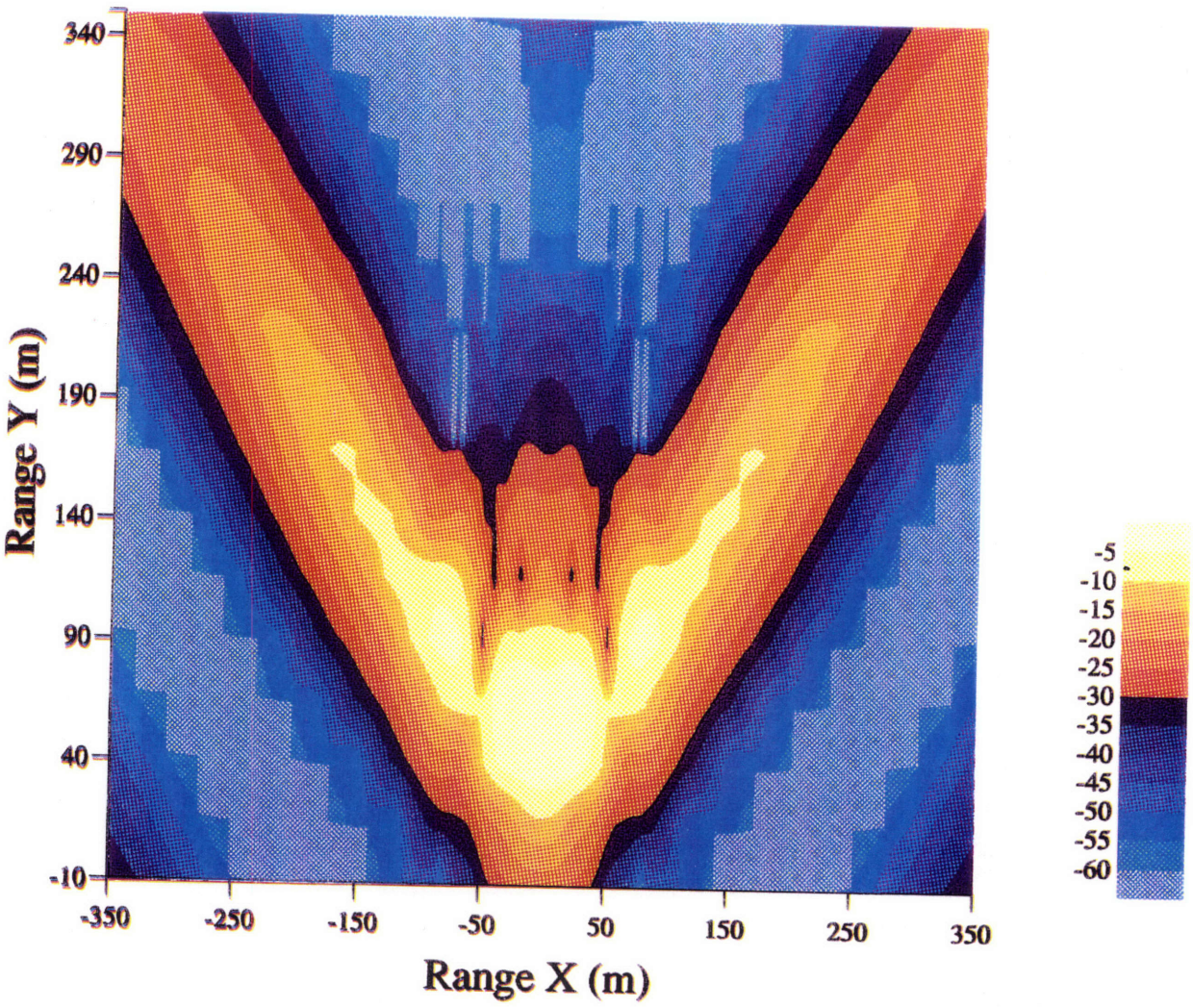

Figure 4-11: Background Pressure Field in the Submerged Case, Received in the Plane 0.2 meters above the Water Column/Sediment Interface

The multiple modes are clearly visible in the kernel plot as evidenced by the separated bright spots and lines (Fig. 4-10). It was noticed that the spectrum is confined between P lines in Fig. 4-6. The reason is that without the ridge, the environment is both Y and X invariant. There is no mechanism to "steer" one part of the spectrum on the $k_x - k_y$ map to another part from the source field to the reverberant field. And because in the water column, the source generates P-wave only, the propagating part of it is confined between P lines [3]. Thus, all the reflected and refracted spectrum in the water column, sediment and bottom are confined between P-lines.

Now, let's look at the field (Fig. 4-11). It is not as easy to identify the different modes here as in the kernel plot. Because the modes are so close together that they, together with the direct arrival and the first reflection form a wide blurred beam. Its direction form an angle a bit smaller than 45^0. Although the source cone has 45^0 angle, the water column/sediment interface cut the cone off-axis.

4.2.2 The Scattered Field

Now, we add the ridge into the picture, which turns it to a 2-1/2 Dimensional facet reverberation problem. The circumference of the cylinder is 37.70m. At 250Hz, the compressional and shear wavelengths in the sediments are 6.4m and 1.6m respectively. And the compressional and shear wavelengths in the ridge are 20m and 10m respectively. We placed 40 nodes around the cylinder, which is dense enough compared with these wavelengths.

First, we put our receiver arrays in the horizontal plane 0.2 meters above the water column/sediment interface. The received (more precisely, simulated) scattered pressure field and its wavenumber spectrum are shown in Fig. 4-13 and Fig. 4-12. To clarify, the figures show only the scattered field. If receiving arrays are placed in the water column, the received signal will be the sum of this scattered field and the background field as shown in Fig. 4-11.

[3] actually, water wave speed is slightly different from the P-wave speed in the sediment (1527m/s vs. 1600m/s). But the different location of P-lines will be hardly noticeable

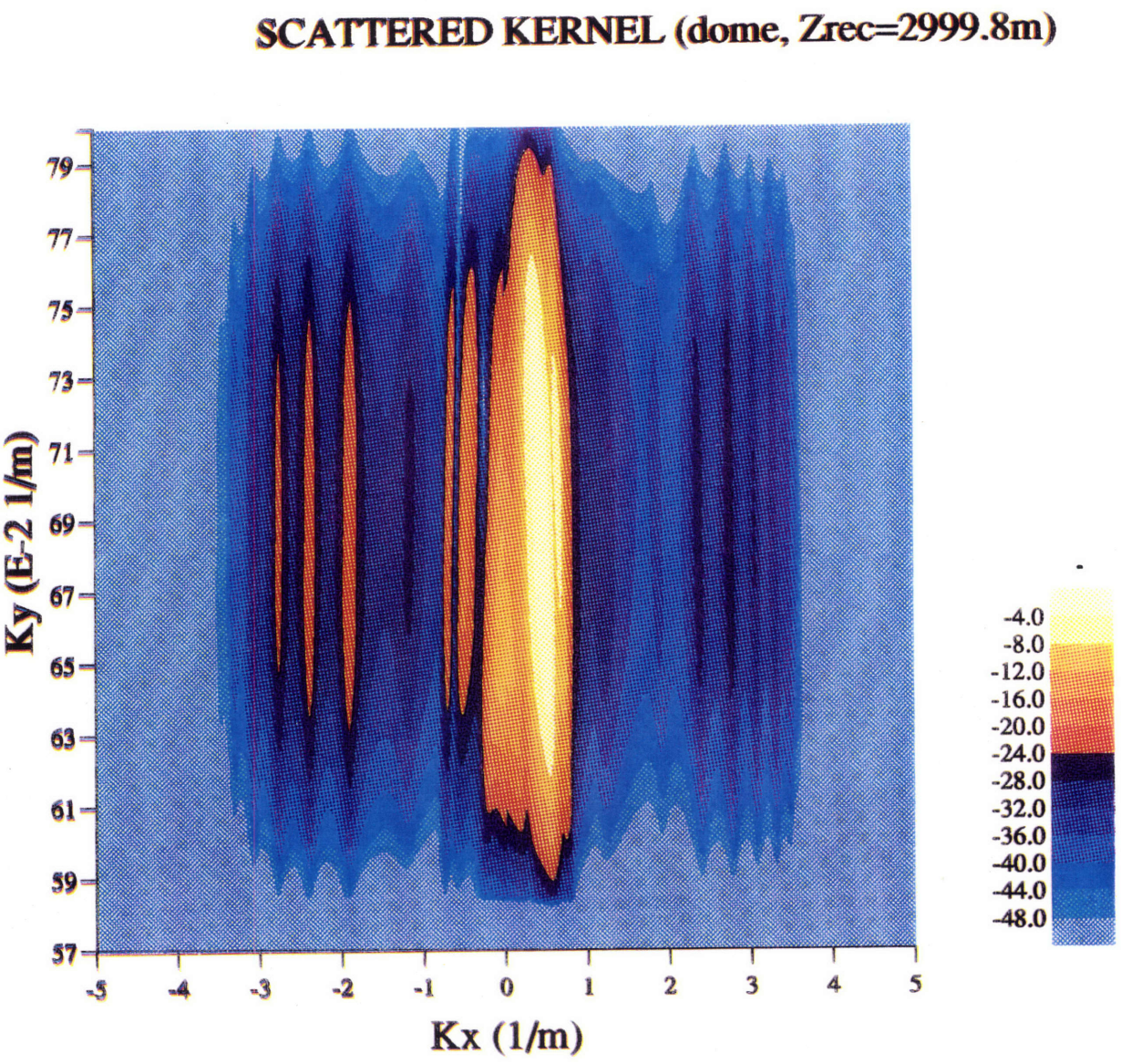

Figure 4-12: The Sediment Covered Ridge Case: the Scattered Pressure Wavenumber Spectrum on the Plane 0.2m Above the Water Column/Sediment Interface

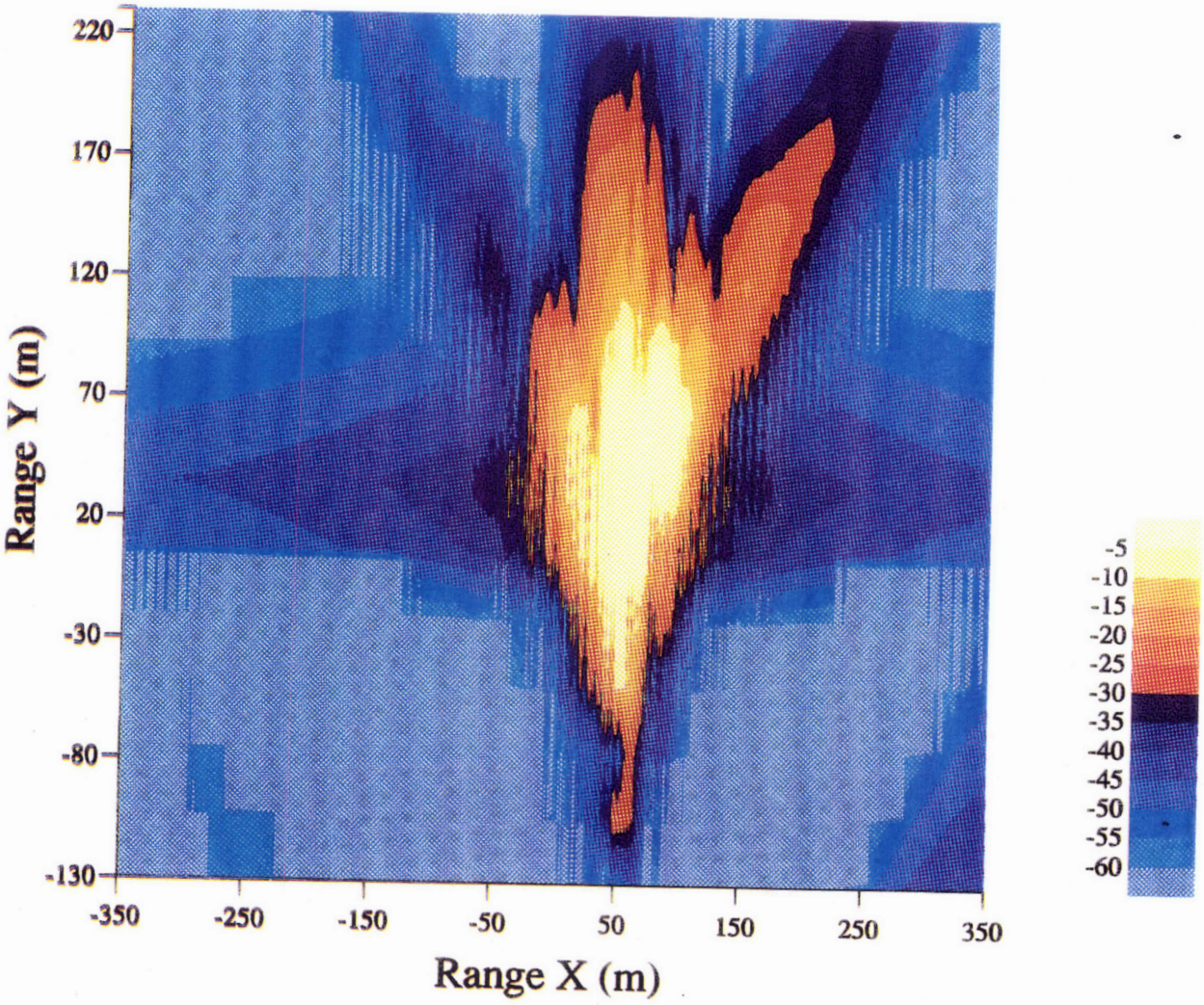

Figure 4-13: The Sediment Covered Ridge Case: the Scattered Pressure Field on the Plane 0.2m Above the Water Column/Sediment Interface

Again, the strongest component is the forward traveling P-wave (near the right P line) and the backward traveling P-wave (the specular reflection is also present).

It is interesting to note that the spectrum (Fig. 4-12) is no longer confined between P lines, as was the case for the kernel of the background field (Fig. 4-10). The reason is that the ridge destroyed the X invariance of the environment. In effect, it "steers" some energy from part of source spectrum (between P lines) into other part of the spectrum (outside P lines). Clearly, some of the S-wave modes are excited in the sediment layer, especially in the backward direction approximately between $k_x = -2m^{-1}$ and $k_x = -3m^{-1}$. These wavenumbers exceeded the water wavenumber, so these S-wave modes are trapped in the sediment layer. Its trace in the water column is evanescent from the interface, and the reason we can see it is that we are very close to the interface. For an estimation of the rate of decay along the Z-axis of the evanescent wave, here we calculate for one point on the mode, where $k_x = -2m^{-1}$, $k_y = 0.7m^{-1}$. The pressure field caused by it in the water column has a z-dependence of the form:

$$P \sim e^{ik_z Z} = e^{i\sqrt{K_w^2 - k_x^2 - k_y^2}Z} = e^{-\sqrt{k_x^2 + k_y^2 - K_w^2}Z} = e^{-\frac{Z}{0.540}}. \tag{4.17}$$

Our receiving plane here is 0.2m above the water colume/sediment interface. According to Eq. (4.17), the pressure field decayed to 0.69 of that on the interface. So we still can see the effects of these S-wave modes.

On the field plot (Fig. 4-13), the forward traveling P-wave is clearly visible. Much weaker, but still clearly visible is the backward traveling P-wave little less than 45^0 with the Y-axis. It is the result of the source wave penetrating into the sediment, specular reflected from the cylinder, and penetrating back into the water column.

The evanescent effect of the S-wave modes in the sediment travels in the direction little less than 90^0 from Y-axis. Because of their close vicinity and the limited resolution, they can hardly be identified separately.

Next, we move the receivers to the horizontal plane 30 meters above the water column/sediment interface. The scattered pressure field and its wavenumber spectrum

are shown in Fig. 4-14 and Fig. 4-15. The forward and backward traveling P-waves are still clearly present. But the sediment S-wave mode effect has decayed out as we are far removed from the interface (Eq. (4.17) gives a factor of $7.5 * 10^{-25}$).

This example clearly shows that the facet causes the wave type conversion. Without the presence of the cylinder, no shear wave is excited. But with the cylinder, a certain amount of energy is converted into shear waves in the sediment layers and the rock bottom. It accounts for the energy loss as well as changes the scattered field pattern, especially near the bottom. To have this wave type conversion, two factors are of essence: facet and elasticity. If we model the sediment layers and the bottom as fluid or rigid body, we would not be able to model the shear wave and the wave type conversion. Elasticity is crucial in this scenario.

4.3 Shallow Water Scenario

In shallow water facet scattering case, the excitation of the facet and the propagation of the scattered waves are strongly affected by the waveguide. So we should integrate the facet scattering mechanism and the waveguide physics in a unified approach. That is exactly what the hybrid WI-BEM is capable of doing. Here, a numerical example is given to illustrate these capabilities.

The environment is shown in Fig. 4-16. The water column is 20m deep, beneath which is a 5m sediment layer overlaying a hard bottom. The facet is a 6m diameter cylinder centered at the sediment/hard bottom interface. Its material properties are identical to that of the hard bottom. Sound speeds and densities of various layers are shown in the figure. It is assumed that the water column is lossless. And the compressional and shear attenuations in the sediment layer are $0.2dB/\Lambda$ and $0.5dB/\Lambda$ respectively. While the compressional and shear attenuations in the hard bottom are $0.1dB/\Lambda$ and $0.2dB/\Lambda$.

The source beam is similar to that in Fig. 4-1, with the inner cone at 38.4^0 and outer cone at 56.4^0. The scattered field is shown in Fig.4-17. We can see clearly the modal patterns. And the main feature are the two beams at 45^0 in the forward and

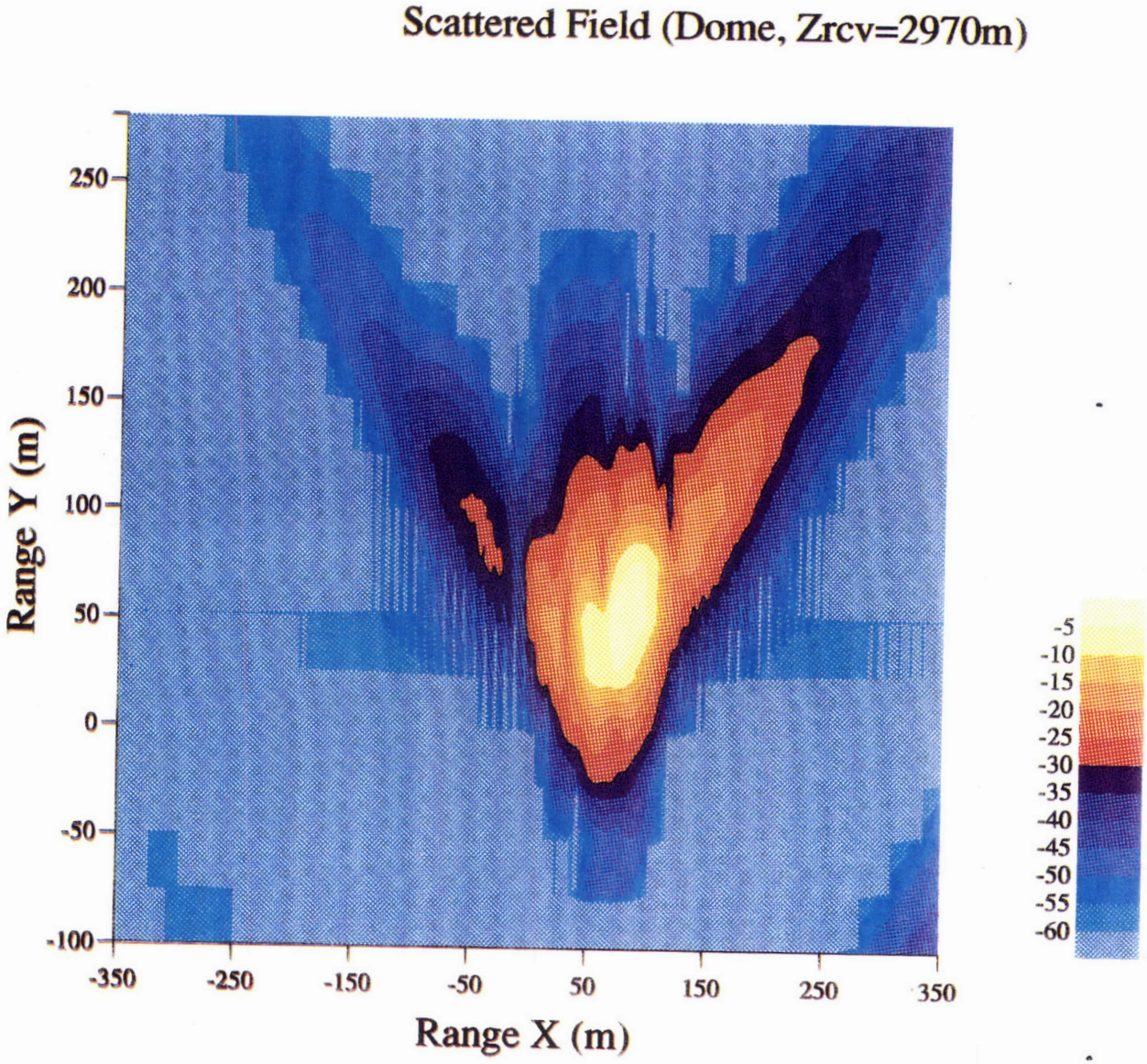

Figure 4-14: The Sediment Covered Ridge Case: the Scattered Pressure Field on the Plane 30m Above the Water Column/Sediment Interface

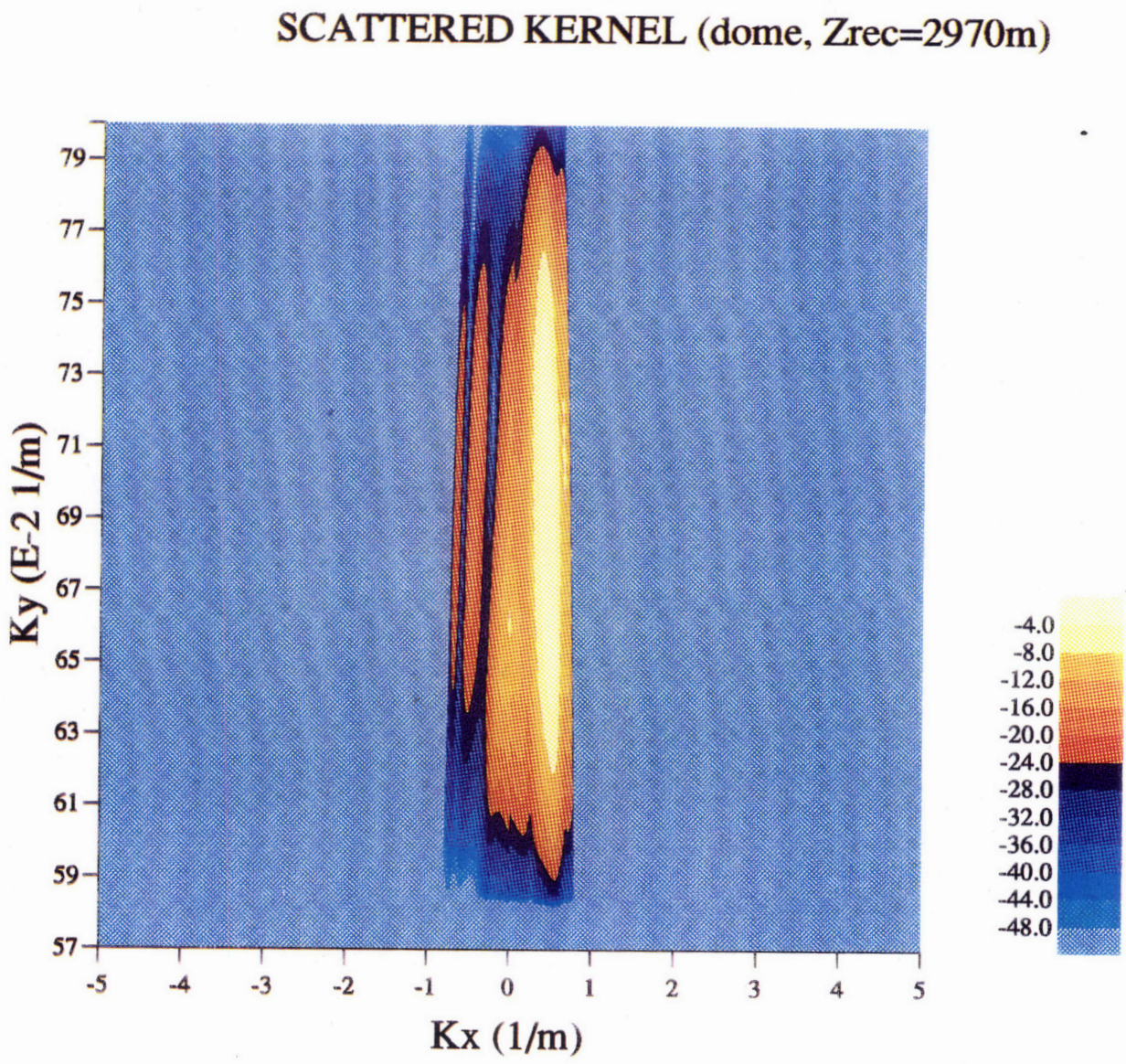

Figure 4-15: The Sediment Covered Ridge Case: the Scattered Pressure Wavenumber Spectrum on the Plane 30m Above the Water Column/Sediment Interface

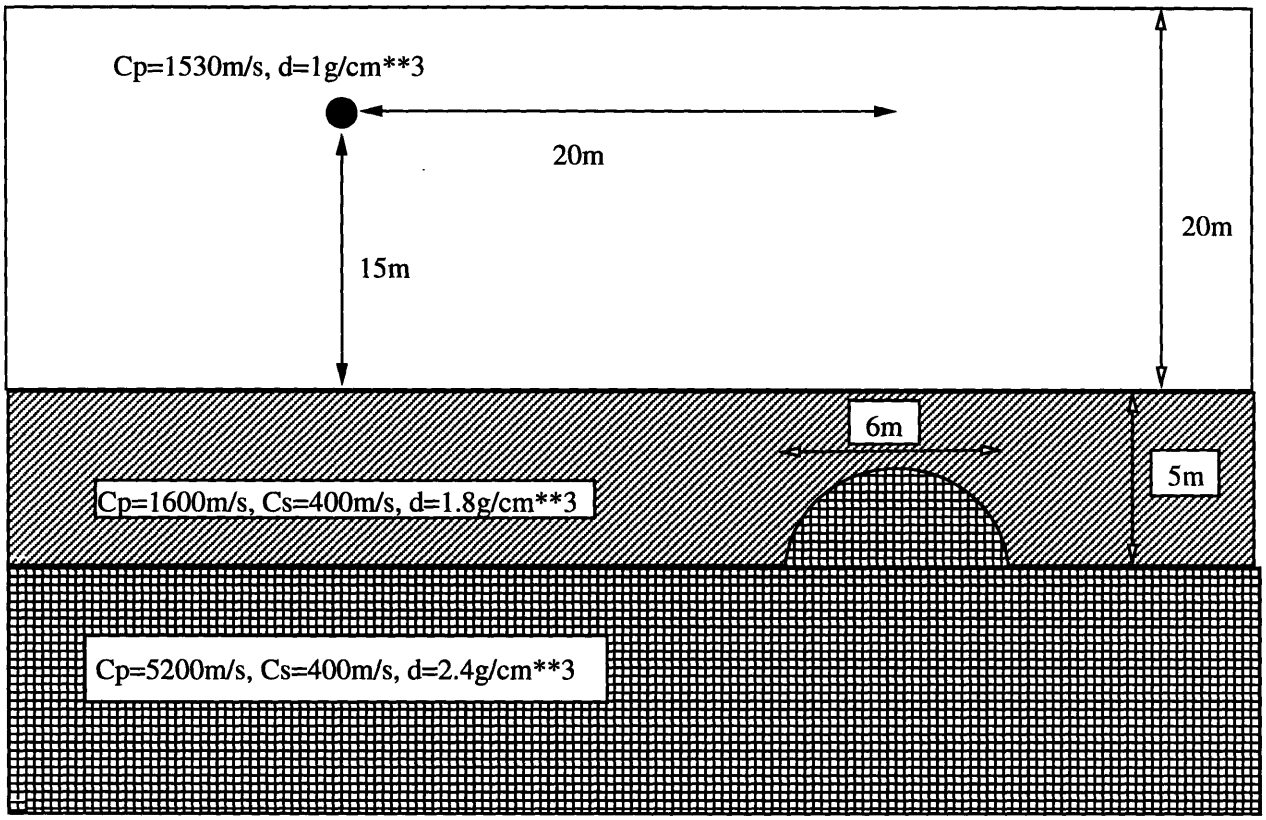

Figure 4-16: The environment for the shallow water facet scattering case

backward direction. What happens is that the incoming field hit the cylinder. And as a secondary source array, the cylinder emits a similar cone-like beam pattern. Of course, this beam pattern will not be rotational symmetric as the original source. As stated before, the k_y value will remain constant. So the portion of the scattered field in the water column will be a cone surface at approximately 45^0 from the Y-axis. As the receiver array is at the horizontal plane, what we get in Fig. 4-17 is the off-axis horizontal cut from this cone. That is why in the figure, towards the end, the two 45^0 beam curves up instead of continuing as straight lines (hyperbolae).

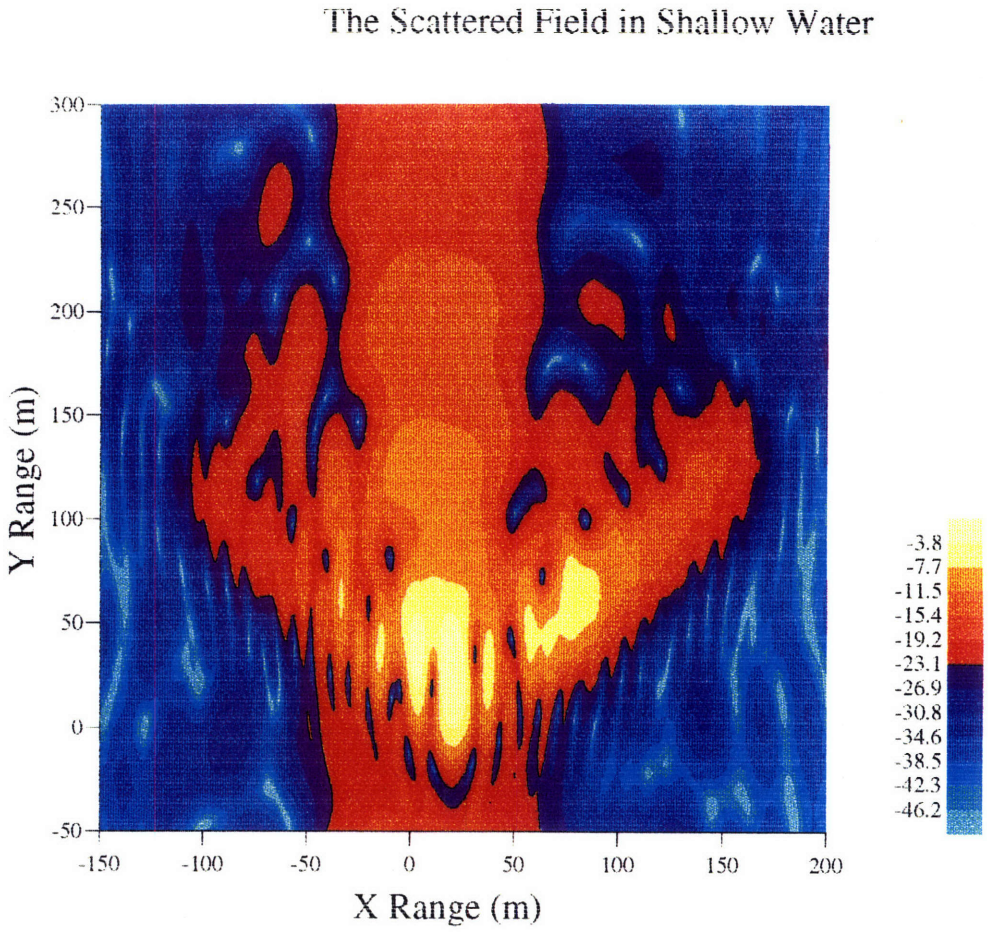

Figure 4-17: The scattered field in the shallow water case. The waveguide is 20m deep, source at 15m from the sediment interface and the receiver at 14m from the interface

Chapter 5

Perturbation Approach in the Diffuse Reverberation Problem

5.1 Statement of the Problem

In the actual reverberation problems occurred in sonar detection, only the interaction of sound wave with some small areas of sea bed (so called *Sonar Footprint*) matters. So, in this and the next chapters, we will confine the rough interface to a small area.

We model the ocean environment as a horizontally stratified (range independent) body of fluid with the seabed consisting of elastic layers. The number of layers and the thickness of each fluid (elastic) layer is arbitrary, so the sound speed profile and other environmental parameters can be approximated with desired accuracy, as long as computation power is sufficient. On top of this smooth picture, a finite area at the ocean body / seabed interface is rough with some particular statistics. By the finiteness and the possible roughness anisotropy, the problem is inherently three-dimensional.

We feel that by confining the rough area the computation time will be cut significantly. Practically, as stated earlier, this scenario is actually what needed in the sonar detection problem. Also, the scenario has theoretical significance. Our patch model provides a tool to isolate an area and investigate the effect of a particular roughness statistics on the scattered field, both at near field and far field.

Figure 5-1: The Rough Interface Patch Problem in the Ocean Waveguide

5.2 Choice of Approach

There have been a fair amount of research work on the general topic of wave scattering from rough surfaces [53]. In what follows, we shall try to explore their relative merits and shortcomings and select one approach that would suit our endeavor here.

5.2.1 Rayleigh Method

Since the first treatment of rough surface scattering by Rayleigh [55, 56] his method has been extended to plane waves of arbitrary angles of incidence and to scattering by random rough surfaces. For a wave of wavevector $\vec{k}$ incident onto a periodic surface given by

$$h(x) = \sigma cos(Kx), \tag{5.1}$$

the scattered field is assumed to be a sum of plane waves propagating in the directions θ_{2m}, where

$$sin\theta_{2m} = sin\theta_1 - mK/k. \tag{5.2}$$

We have, therefore, that the total field is given by

$$\psi(\vec{r}) = \psi^{inc}(\vec{r}) + \sum_{m=-\infty}^{\infty} A_m e^{i\vec{k}_m \bullet \vec{r}}. \tag{5.3}$$

Equation (5.3) is substituted into the appropriate boundary conditions and the resulting equation is expanded as a Fourier series. The resulting Fourier coefficients are equated, leading to an infinite set of linear equations which can be solved by iteration. In practice the series converges quickly only if $k\sigma << 1$. Rice [57] extended this work to random rough surfaces. He considers the scattering of electromagnetic waves and expands the rough surfaces as a Fourier series in which the coefficients themselves are random

$$h(x, y) = \sum_{m,n} P(m, n) e^{-iK(mx+ny)}, \tag{5.4}$$

where the P(m,n)'s are independent and distributed normally about zero. Evalua-

tion of the mean reflection coefficient is, in practice, feasible only for slightly rough surfaces. The Rayleigh method has, in general, no significant advantage over the Kirchhoff method (we will discuss it later in this section) for slightly rough surfaces. The only advantage of the Rayleigh method is that no restriction on surface radius of curvature is necessary. Surfaces for which the Kirchhoff method is inappropriate due to rapid changes in surface profile can therefore be considered using the Rayleigh method.

The major assumption of the Rayleigh method is that the scattered wave is composed of waves traveling away from the surface. This method cannot, therefore, include all multiple scattering, where waves traveling towards parts of the surface will also exist. In addition it has been shown that with this assumption of outward traveling waves it is impossible to satisfy the required boundary conditions exactly.

5.2.2 Boss Approximation

One school of interesting approaches to the rough surface scattering problem is to model the rough surface as a random array of scatterers. One approach was proposed by Ament, who described a rough surface as an array of planar facets with known reflection properties [4]. Spetner modeled the rough surface as an array of randomly placed point scatterers [67].

Along the similar line, a more general "boss" model was proposed. Biot modeled a rigid surface as an array of hemispherical bosses whose separation and size are both small relative to the incident wavelength [6]. Later Tolstoy generalized his theory to allow for non-spherical scatterers which form a rough surface separating two acoustic media of different density and wavespeed. Twersky took a slightly different approach to the problem of the scattering of waves by a rough surface of bosses. He used a Green function formulation to determine the effective coherent reflection coefficient and incoherent scattering cross section. In what follows, we will examine Twersky's Boss model in more detail. He has been developing this model for many years, and the results were reflected in a series of papers. [76, 77, 78, 79, 75]

Twersky modeled the random rough surface as completely rigid or free plane with

identical protuberances (bosses) distributed on it. The bosses had known shape and were symmetrical with respect to the mean plane. Together with its image it formed a ellipsoid, whose scattering characteristic is known. The randomness was introduced by the random distribution of the bosses on the mean plane.

As one of the results, Twersky predicted that when we had nearly grazing incidence, the reflection coefficient would approach -1, hence the total field near zero – the so called "zone of silence". This agreed with the results of Biot [6] and Howe [31].

Some assumptions were made in the boss theory. Their merits and implications are discussed in the following.

About Order of Scattering

It was assumed that the average field with two scatterers fixed was equivalent to that with one scatterers fixed. Here the recursive multi-order scattering method was used. It was equivalent to starting a successive scattering process with the average single scattered wave. This implied that each stage of scattering was averaged separately and thus prevented the occurrence of mutual path differences in subsequent stages of scattering. But no discussion of conversion of such recursive method was given.

Alternatively, we can regard this treatment as substituting one of the fixed bosses by one random placed boss. The error thus introduced was small since only one of the large number of bosses was altered. This is only a loose justification, a rigorous conversion study is still needed.

About Boss Excitation

When determining the excitation of bosses, the random part of the field scattered by all the other bosses was neglected. This treatment is not always legitimate and could lead to an erroneous result. Specifically, the average over the derivative of a function is not equivalent to the derivative of the average function.

About Boss Distribution Statistics

Twersky treated two kinds of statistical distribution of bosses: uncorrelated (lattice gas statistics) and pairwise correlated (Percus-Yevick function). A discussion of a more general distribution might be interesting and make the treatment complete. But considering this work will have limited practical application anyway, it's only the qualitative results that counts. It is probably not worthwhile to go through the troubles to consider more complex statistics.

Overall Evaluation

The boss model is far from realistic and has extremely limited practical application. Nevertheless it gave us some insight into one of the problems that have been hard to handle with other methods – multiple scattering. By intuition, we expect that the multiple scattering effect is more important as the incidence angle gets away from normal, which occurs frequently in underwater acoustics where we often have grazing incident on the seasurface and seafloor.

We anticipate that the boss model should generate good results when the rough surface spectrum approaches that of white noise.

5.2.3 Kirchhoff Approximation

Kirchhoff theory was originated from the study of light diffraction through an aperture by Kirchhoff [40, 5]. The formulation is based upon an exact integral formulation, but approximation to the wave field is made on the surface of the interface. The basic idea is that, at any point on an interface, the surface is treated as though it is part of an infinite plane, parallel to the local surface tangent. Thus the theory is exact for an infinite, smooth, plane scatterer but is approximate for scatterers that are finite-sized, non-planar, or rough. It is expected that the method performs well if the surface gradient changes slowly. There is no restrictions on the maximum surface height or gradient. A rule of thumb for the validity of Kirchhoff approximation is:

$$Kasin^3\theta_1 >> 1, \tag{5.5}$$

where K is the wavenumber of the incident wave, a is the local radius of curvature of the surface, θ_1 is the grazing angle.

A restriction is therefore placed on the radius of curvature of the surface, relative to the wavelength of the incident wave, the severity of this restriction being dependent on the angle of incidence. It is clear that any surface to which the approach is applied must have a height profile with no rapid changes in its gradient. No explicit restrictions on the magnitude of the height or gradient are required.

In the case of penetrable media additional difficulties arise. The main reason is that the transmitted field must also satisfy equation (5.5), which means that the transmitted field must not propagate at grazing incidence. The result is that the scattered field in penetrable media which has been calculated using the Kirchhoff approximation may quite seriously deviate from exact solutions when the local incident angle on the rough sourface θ_1 approaches the critical grazing angle of the second media. Thus a modified requirement in terms of the incident field and the media properties is:

$$K_1asin^2\theta_1 sin(\frac{K_1}{K_2}\theta_1) >> 1, \tag{5.6}$$

where K_1 and K_2 are the bulk medium wavenumbers in the first and second medium. With this modified version of the Kirchhoff criteria it is clear that when $\frac{K_1}{K_2}$ is large, as is the case with a fast bottom, the modified criteria is more stringent than its non-penetrable media counterpart.

The literature on Kirchhoff theory applied to acoustic wave scattering from rough surfaces is extensive. Application to elastic wave scattering is analogous but complicated by the presence of mode conversion and has not been so extensively developed.

In acoustic scattering problems there are two quantities to be specified on the scattering surface, the pressure (or potential) ϕ and its gradient relative to the surface normal, $\frac{\partial\phi}{\partial n}$. One of these is known from the boundary conditions satisfied at the surface. The second quantity is specified at the surface with the aid of the Kirchhoff

approximation. If the pressure is to be specified then we have that the scattered pressure may be replaced on the surface by the incident pressure multiplied by some reflection coefficient R, which may itself be a function of $\vec{r}$, the surface coordinate. The total potential on the surface is then given by

$$\phi(\vec{r}) = (1 + R)\phi^{inc}(\vec{r}). \tag{5.7}$$

If the gradient of the potential is to be specified, we have that

$$\frac{\partial\phi(\vec{r})}{\partial\vec{n}} = (1 - R)\frac{\partial\phi^{inc}(\vec{r})}{\partial\vec{n}}, \tag{5.8}$$

where $\vec{n}$ is the unit normal to the rough surface.[1]

The scattered field at some observation point away from the surface is written in terms of the field quantities on the surface using the Helmholtz scattering formula

$$\phi(\vec{r}) = \phi^{inc}(\vec{r}) + \int_{S_0}[\phi^{sc}(\vec{r_0})\frac{\partial G(\vec{r},\vec{r_0})}{\partial\vec{n_0}} - G(\vec{r},\vec{r_0})\frac{\partial\phi^{sc}(\vec{r_0})}{\vec{n_0}}]d\vec{S_0}, \tag{5.9}$$

where the integral is over S_0, the rough surface, and the quantity ϕ^{sc} appearing in the integral is the scattered field on the surface, $\vec{n}$ is the unit outer normal to the surface. By substitution of (5.7) or (5.8) into (5.9), together with the boundary conditions, an expression is obtained for the scattered field at some point $\vec{r}$, in terms of known quantities. This gives the general result of the scattering problem in the Kirchhoff approximation. The integral to be evaluated depends on the incident wave, the form of the rough surface and the nature of the reflection coefficient. We see that this approach is the next level of improvement on the theory based on geometric optics, where incident rays are assumed to be reflected in the "local specular" direction with unit amplitude.

[1]The negative sign of R arises from the reversal of direction of the incident and scattered waves, relative to the surface normal.

5.2.4 Perturbation Theory

The perturbation theory is particularly useful for low frequency wave scattering. The basic idea is that, since the roughness is "small" compared to the "scale" of the problem for slightly perturbed surfaces, the resulting wave field is expected to deviate from the unperturbed ones at most the order of the ratio of roughness to wave length. Thus, by Taylor expansion, the total field at a point may be expressed as an unperturbed solution with an addition of small correction due to the perturbation.

If the surface height and its gradient are "small", and the surface profile is slowly varying with no discontinuities, then the field scattered from the rough surface may be expanded in an infinite series:

$$\phi(\vec{x}) = \phi^{inc}(\vec{x}) + \sum_{n=0}^{\infty} \phi_n^{sc}(\vec{x}), \tag{5.10}$$

where $\phi^{inc}(\vec{x})$ is the incident wave field and $\phi_n^{sc}(\vec{x})$ is the nth-order approximation to the scattered field. The $n = 0$ term is given by the scattered field which would exist if the surface were smooth (the unperturbed solution). It is also assumed that if the boundary conditions obeyed on the rough surface are of the form

$$f(x, y, z) \mid_{z=h(x,y)} = 0, \tag{5.11}$$

then they may be expanded in a Taylor series about the mean plane $z = 0$, of the form

$$f(x, y, z) \mid_{z=h(x,y)} = f(x, y, z) \mid_{z=0} + h\frac{\partial f}{\partial z} \mid_{z=0} + \frac{h^2}{2}\frac{\partial^2 f}{\partial z^2} \mid_{z=0} + \ldots \tag{5.12}$$

Here $f(x, y, z)$ is, for example, the displacement or traction components on the rough surface. Effective boundary conditions may then be found for the smooth surface, z=0, the form of these depending on the true boundary conditions and on the order of the terms retained in equation (5.12).

Range of Validity

For the perturbation method to be valid, both the height and the slope of the rough surface have to be small:

$$\begin{cases} K|h| << 1; \\ \nabla h << 1. \end{cases} \tag{5.13}$$

Again, with K being the wavenumber of the incident wave, and $h(\vec{x})$ being the height of the rough surface.

Questions have been raised as to whether the smallness requirement in (5.13) guarantees the success of the perturbation theory, and what defines the explicit criterion. Thorsos and Jackson tried to address these issues.

In their paper [73], the authors used the perturbation method to study a two-dimensional acoustic wave scattering from a pressure-release surface with a Gaussian roughness spectrum. Emphasis was placed on the first-order perturbation theory, i.e. only two terms on the right-hand-side of Eq. 5.12 were retained. Using an integral equation method and higher-order analysis, the authors concluded that the often cited criterion (Eq. 5.13) is not sufficient to guarantee the success of the first-order perturbation theory. Another parameter Kl, where l is the roughness correlation length, plays an important role in defining the region of validity. There are cases which demonstrated that for a fixed value of kh, increasing kl (equivalently reducing the RMS slope) worsens the performance of the theory particularly for the backward scattering. The fact is that increasing kl will reduce the resonance wavenumber for the 4th order term, leading to a contribution larger than the 2nd order term. However, the performance of the lower order theory is in general very good in forward scattering. Moreover, it should be remembered that since their analysis is based upon the Gaussian roughness spectrum, the results may not necessarily apply to roughness spectra that exhibit power laws.

The explicit criteria which define the region of validity were established in the paper. An important guideline is that if Gaussian roughness spectrum is used the lower order analysis is appropriate for $Kh << 1$ and $Kl \leq 6$.

5.2.5 Comparison of the Approaches

These different approaches have their respective advantages and shortcomings. They shall be used with discretion, being aware of their range of validity. The different approaches are, in general, a compromise between the need for accurate predictions of the effects of surface roughness and the requirement for reasonable mathematical simplicity.

In Kirchhoff approximation, the mean and the scattered field are intrinsically combined in one solution, while in perturbation theory the total field is the superposition of the mean and scattered field along the mean interface. The fact that the field is collapsed to the interface highlights one of the limitations of the theory.

One strength of perturbation theory is that it does not require locally flat surfaces, so that scattering from fine detail is well modeled. Another strength of perturbation theory is its versatility at low grazing angles. It does not canonically fail near or at critical angles for penetrable media like the Kirchhoff approximation does, and the scattered cross section is never overpredicted for low angles of backscattering. A further accidental advantage of perturbation theory is that it is possible to incorporate into wavenumber domain models. This is because the expansion of the scattered field need not be evaluated along the scattering surface as in Kirchhoff theory, only along the mean interface. Thus for perturbation theory the surface integral over the rough interface is approximated by the summation of two straight line integrals, one for the mean field, which may be obtained easily by other method, and one for the scattered field which is a function of the boundary discontinuities.

There has always been some ambiguities about which result is better when the smallness condition is satisfied for both the perturbation theory and the Kirchhoff theory, but the results differ. Thorsos and Jackson [73] pointed out that if the surface is such that the Kirchhoff approximation is valid ($kl > 6$ for the Gaussian spectrum with average slope less than 20^0) and $Kh << 1$, then the complete Kirchhoff approximation is superior to the perturbation approximation. However, if $kh << 1$ and $kl \leq 6$, then the higher-order terms make little contribution, and thus perturbation

theory is the preferred approach.

Perturbation approach is the choice of method in this thesis because of the tremendous speed gains realizeable over full elastic solutions, and because of their ability to treat large extent roughness on waveguide boundaries. For general evaluations of scattering from fairly benign roughness features, distributed according to some law along an arguably mean interface (5.13), the perturbation theory performs beautifully. For larger, distinctive scattering features, WI-BEM method is well suited.

5.3 Previous Developments of Perturbation Theory as Applied in the Ocean Acoustics

The structure of the reverberant field from the interface scattering in a ocean fluid elastic waveguide should be studied using the combined physics of scattering from rough interface and the waveguide physics governing the mean field propagation. Along this line, Schmidt and Kuperman developed a self-consistent approach using perturbation method [41, 63]. Their model can be used to predict the effect of rough interfaces on the mean field as well as the the higher-order statistics of waveguide reverberation.

Subsequently, Liu et al. [47] combined the perturbation theory with a model of random surface sources to provide a unified theory for rough bottom scattering of ambient noise in the ocean, demonstrating the significance of scattering into seismic modes in shaping the spectral behavior of the deep ocean noise field observed experimentally. LePage et al. [42] used a full three dimensional implementation of the theory to model transmission loss in the Central Arctic, and based on excellent agreement with historical loss data, provided theoretical evidence for scattering into the flexural ice modes being the dominant loss mechanism in the Arctic.

5.4 An Overview of the Boundary Operator Expansion Approach

In the following we review one perturbation approach developed by Schmidt and Kuperman : the Boundary Operator Expansion Approach for rough interface scattering in stratified elastic waveguide [41, 44].

As we have described, the perturbation method does not appeal to the integral equations to model the effects of rough surface scattering. Instead a Taylor series expansion of the local boundary conditions in the parameter of surface height is used to seek a series solution for the scattered field. To each order the inhomogeneous equation for the scattered field are forced by terms which are effective source distributions spread along the mean scattering interface. Thus the boundary integral equations are no longer utilized, and instead the scattered field is determined through a volume integral over these sources and the free space Green's functions. The forcing terms at each order are generally functions of lower order solutions. Within the validity range of perturbation theory, higher order terms have less significant contributions to the total solution.

In a homogeneous and isotropic elastic medium, the seismo-acoustic field produced by one or more sources of time dependence $e^{-i\omega t}$ can be expressed in terms of three scalar displacement potentials,

$$\Phi(\vec{x}) = \begin{cases} \phi(\vec{x}), & \text{P waves} \\ \psi(\vec{x}), & \text{SV waves} \\ \Lambda(\vec{x}), & \text{SH waves} \end{cases} \tag{5.14}$$

satisfying Helmholtz equations of the form:

$$\nabla^2\Phi(\vec{x}) + K^2(z)\Phi(\vec{x}) = -\delta(\vec{x} - \vec{x_s}). \tag{5.15}$$

At each interface between layers, the potentials must satisfy the boundary conditions of continuity of tractions and displacements, which can be stated in an operator

form:

$$\begin{bmatrix} U & -U \\ T(\vec{n})U & T(\vec{n})U \end{bmatrix} \bullet \begin{bmatrix} \Phi^+ \\ \Phi^- \end{bmatrix} = - \begin{bmatrix} u_i \\ t_i(\vec{n}) \end{bmatrix}, \tag{5.16}$$

where Φ^+ is a vector of wavefield potentials in upper layer of the interface and Φ^- being that in the lower layer. U and T are matrices of differential operators, the number and type of which depends on the type of interface i (separating layers i and i+1). $\vec{n}$ is the local unit normal vector of the interface. u_i and t_i are the forcing of displacements and tractions on the interface caused by real sources. Here we used the term "real" to distinguish it from the "virtual" source which will be used later in the section.

In Eq.(5.16), the displacement operator is

$$U = \begin{bmatrix} \frac{\partial}{\partial x} & 0 & -\frac{\partial}{\partial z} \\ \frac{\partial}{\partial y} & \frac{\partial}{\partial z} & 0 \\ \frac{\partial}{\partial z} & -\frac{\partial}{\partial y} & \frac{\partial}{\partial x} \end{bmatrix}, \tag{5.17}$$

and the normal traction operator is

$$T(\vec{n}) = \begin{bmatrix} n_x & n_y & n_z \end{bmatrix} \bullet \begin{bmatrix} A & | & B & | & C \end{bmatrix}, \tag{5.18}$$

where

$$A = \begin{bmatrix} (\lambda+2\mu)\frac{\partial}{\partial x} & \lambda\frac{\partial}{\partial y} & \lambda\frac{\partial}{\partial z} \\ \mu\frac{\partial}{\partial y} & \mu\frac{\partial}{\partial x} & 0 \\ \mu\frac{\partial}{\partial z} & 0 & \mu\frac{\partial}{\partial x} \end{bmatrix}, \tag{5.19}$$

$$B = \begin{bmatrix} \mu\frac{\partial}{\partial y} & \mu\frac{\partial}{\partial x} & 0 \\ \lambda\frac{\partial}{\partial x} & (\lambda+2\mu)\frac{\partial}{\partial y} & \lambda\frac{\partial}{\partial z} \\ 0 & \mu\frac{\partial}{\partial z} & \mu\frac{\partial}{\partial y} \end{bmatrix}, \tag{5.20}$$

$$C = \begin{bmatrix} \mu\frac{\partial}{\partial z} & 0 & \mu\frac{\partial}{\partial x} \\ 0 & \mu\frac{\partial}{\partial z} & \mu\frac{\partial}{\partial y} \\ \lambda\frac{\partial}{\partial x} & \lambda\frac{\partial}{\partial y} & (\lambda+2\mu)\frac{\partial}{\partial z} \end{bmatrix}. \tag{5.21}$$

We can rewrite Eq. (5.16) in condensed notation:

$$B(\vec{x})\Phi^{\pm}(\vec{x}) = -f(\vec{x}). \tag{5.22}$$

It is well known that in a range-independent environment with smooth boundary, the problem is solved by Fourier transforming the Helmholtz equation into the depth-separated wave equation:

$$\frac{d^2\tilde{\Phi}(\vec{k},z)}{dz^2} - [k^2 - k_i^2(z)]\tilde{\Phi}(\vec{k},z) = -\frac{\delta(z-z_s)}{2\pi}, \tag{5.23}$$

with k_i being the compressional wavenumber for the compressional potential and shear wavenumber for the shear potentials. The solution of this equation can be expressed as a superposition of a particular solution satisfying the inhomogeneous equation and a linear combination of the two independent homogeneous solutions. The exact amplitudes of various terms are readily determined by the smooth boundary conditions and source terms.

Now, in our rough interface case, the wave equations are the same. But the boundary conditions (actually, boundary shapes) are not trivial.

The solution technique entails expanding the scattered potentials and the boundary operators at the rough interface in the series expansions in increasing order of the surface height parameter $\eta(\vec{x})$,

$$\Phi^{\pm}(\vec{x}) = \sum_{m=0}^{\infty} \phi_m^{\pm}(\vec{x}), \tag{5.24}$$

$$B(\vec{x}) = B_0(\vec{x}) + \frac{\partial B_0(\vec{x})}{\partial z} + \eta_{,j} \circ b_0|_{z=z_0} + O(\eta^2). \tag{5.25}$$

In Eq. (5.25), the rotational transformation has been incorporated into the operator b. The exact form of $\circ$ will be given in the next section.

Now, we can solve the resulting boundary value problems at various orders of the expansion parameter. So, the zeroth order solution corresponds to the unperturbed smooth elastic interface problem, while the first order solution contains the scatter-

ing behavior for small interface roughness, and the higher order solutions contain correction terms which account for larger roughness effects. When the roughness amplitudes are small compared to the acoustic wavelength, the higher order effects will be progressively less significant. In this thesis, only the zeroth and the first order effects are considered.

The zeroth order equation for the scattered field is simply the smooth boundary problem with inhomogeneous forcing by the real source on the RHS

$$B_0(\vec{x})\phi_0^{\pm}(\vec{x}) = -f(\vec{x}). \tag{5.26}$$

The first order equation for the scattered field incorporates the first effects of the roughness parameter both as a scalar multiplier in the translational term and a coupling term controlling the rotational operator:

$$B_0(\vec{x})\phi_1^{\pm}(\vec{x}) = [-\eta\frac{\partial B_0}{\partial z}\phi_0^{\pm}(\vec{x}) - \eta_{,j} \circ b_0\phi_0^{\pm}(\vec{x})]\delta(z - z_i), \tag{5.27}$$

where z_i is the depth of interface.

First, the following two terms are computed,

$$d(\vec{x}) = \frac{\partial B_0(\vec{x})}{\partial z}\phi_0^{\pm}(\vec{x}) = -\int iq\tilde{B}_0(\vec{k})\tilde{\phi_0^{\pm}}(\vec{k})e^{i\vec{k}\bullet\vec{x}}d\vec{k}; \tag{5.28}$$

$$r(\vec{x}) = b_0(\vec{x})\phi_0^{\pm}(\vec{x}) = -\int i\vec{k}\tilde{b}_0(\vec{k})\tilde{\phi_0^{\pm}}(\vec{k})e^{i\vec{k}\bullet\vec{x}}d\vec{k}. \tag{5.29}$$

These spatial displacement and rotation terms are then multiplied directly by the surface roughness height and gradient to yield the spatial boundary discontinuities in stress and strain that the scattered field must satisfy at each interface:

$$B_0(\vec{x})\phi_1^{\pm}(\vec{x}) = -\eta(\vec{x})d(\vec{x}) + \eta_{,j}(\vec{x})r(\vec{x}) = -f_v(\vec{x}). \tag{5.30}$$

Comparing this with equation (5.26), It is obvious that we can treat the first order rough interface scattering problem as if the boundaries were smooth, with distributed virtual sources replacing the interface roughness, while the virtual sources

are functions of the zeroth order potential.

5.5 The Perturbation Approach in the Rough Patch Scenario

5.5.1 Spatial Convolution Treatment of the Virtual Sources

As mentioned in last section, equation (5.30) shed light on the way we can solve for the scattered field. Thus, because of the form of of Eq. (5.30), the first order potential can be expressed as a spatial convolution of a simple potential term $\hat{\phi}$ and the virtual source distribution:

$$\phi_1^{\pm}(\vec{x}) = \int \hat{\phi}^{\pm}(\vec{x} - \vec{x_s}) f_v(\vec{x_s}) d\vec{x_s}. \tag{5.31}$$

$\hat{\phi}^{\pm}$ is the wavefield potential in the waveguide with smooth interfaces generated by a point interface discontinuity:

$$B_0(\vec{x})\hat{\phi}^{\pm}(\vec{x'}) = -\delta(\vec{x'}), \tag{5.32}$$

where $\vec{x'} = \vec{x} - \vec{x_s}$.

Eq. (5.31) has a straight-forward physical interpretation. For a particular field point $\vec{x}$, if we know the field generated by a unit source at each point on the patch $\hat{\phi}^{\pm}(\vec{x'})$, then the total field at $\vec{x}$ is simply the superposition of these point source fields, weighted by the actual source strength at each source point.

Convolution in the spatial domain translates into multiplication in the wavenumber domain, so,

$$\tilde{\phi_1}^{\pm}(\vec{k}) = \tilde{\hat{\phi}}^{\pm}(\vec{k}) \tilde{f}_v(\vec{k}). \tag{5.33}$$

Thus,

$$\phi_1^{\pm}(\vec{x'}) = \int e^{i\vec{k}\bullet\vec{x'}} \tilde{\hat{\phi}}^{\pm}(\vec{k}) \tilde{f}_v(\vec{k}) d\vec{k}. \tag{5.34}$$

The key to efficient computation is a hybrid spatial-wavenumber approach. The

virtual source distribution $f_v(\vec{x_s})$ is evaluated directly in the spatial domain. From Eq. (5.30), we can see that in spatial domain, the virtual source vanishes outside the patch. Thus this direction spatial domain evaluation is extremely numerically efficient. The wavenumber domain evaluations are used only to obtain derivatives of the various elastic boundary conditions and to efficiently obtain the Greens function for the layered media.

5.5.2 Cylindrical Representation of the Virtual Sources

For the moving coordinates used in last section, it is natural to choose Cartesian coordinate system. Such a model has been developed [44, 42] for the scattering from roughness patches on an interface separating a fluid and an elastic halfspace. However, due to numerical effort required, it allows for modeling of the scattered near field only. More importantly, it prohibits the incorporation of waveguide effects, thus totally unapplicable to the shallow water environment.

In this section, instead of the moving coordinates $(\vec{x'})$, we choose the fixed coordinates $(\vec{x})$. As virtual sources are confined in the small patch area, a cylindrical coordinate system with origin within the patch is a more natural choice:

$$\phi_1^{\pm}(r,\theta) = \sum_m [cos(m\theta) \int J_m(kr) \tilde{\hat{\phi}^{\pm}}_1^m(k) \tilde{f}_{v1}^m(k) dk + sin(m\theta) \int J_m(kr) \tilde{\hat{\phi}^{\pm}}_2^m(k) \tilde{f}_{v2}^m(k) dk]. \tag{5.35}$$

Representing the virtual sources in cylindrical coordinates overcomes the aforementioned shortcomings of the previous model. First, it is compatible with the 3-D version of the SAFARI code, which has can be modified to provide extremely efficient numerical simulation of the waveguide effect.

Second, this cylindrical representation greatly enhance the numerical efficiency of the scattered field computation, thus enable the far-field computation. This is because the smaller the area of source distribution, the lower the Fourier order we need to include to represent the field. The rule of thumb is that for a patch of radius a and media wavenumber k_0, the Fourier expansion terms of order $m > K_0 a$ have insignificant contribution to the field. For example, in the numerial examples

described later, the patch has maximum radius of approximately $100m$, and the water wavenumber is approximately $1m^{-1}$. We only need to calculated terms up to Fourier order 100. To avoid alias and at the same time cover the whole wavenumber spectrum, approximately 2000 samples in the wavenumber domain have to be calculated for the scattered field computation. If using Cartesian coordinate system, we have to compute 4,000,000 samples, but if using cylindrical coordinate system, only 200,000 samples are needed, translating into only 5% the computation time.

There is one caveat. Due to the simplicity to manipulate, the incident wave and the spatial domain discontinuities of displacements and tractions are most conveniently described in Cartesian coordinate system. The transform into cylindrical representation in a form that is compatible with the 3-D DGM is not a trivial mathematical excercise. In the following, we shall establish the relationship of the virtual sources (displacement and tractions discontinuities) under these two different coordinates.

5.5.3 The Coordinate System Transform

In cylindrical coordinates, the displacement $\vec{u}(r,\theta,z_0)$ at interface $z = z_0$ will be decomposed as:

$$\vec{u}(r,\theta,z_0) = \hat{e_r}u_r(r,\theta,z_0) + \hat{e_\theta}u_\theta(r,\theta,z_0) + \hat{e_z}u_z(r,\theta,z_0), \tag{5.36}$$

and the components will be further expanded as:

$$\begin{cases} u_r(r,\theta,z_0) = \sum_m [U^m_{r1}(r,z_0)cos(m\theta) + U^m_{r2}(r,z_0)sin(m\theta)], \\ u_\theta(r,\theta,z_0) = \sum_m [U^m_{\theta 1}(r,z_0)sin(m\theta) - U^m_{\theta 2}(r,z_0)cos(m\theta)], \\ u_z(r,\theta,z_0) = \sum_m [U^m_{z1}(r,z_0)cos(m\theta) + U^m_{z2}(r,z_0)sin(m\theta)], \end{cases} \tag{5.37}$$

in which

$$\begin{cases} U^m_{zi}(r,z_0) = \int Z^m_i(k_r,z_0)J_m(k_r r)k_r dk_r, \\ U^m_{ri}(r,z_0) + U^m_{\theta i}(r,z_0) = \int [R^m_i(k_r,z_0) + \Theta^m_i(k_r,z_0)]J_{m+1}(k_r r)k_r dk_r, \\ U^m_{ri}(r,z_0) - U^m_{\theta i}(r,z_0) = \int [R^m_i(k_r,z_0) - \Theta^m_i(k_r,z_0)]J_{m-1}(k_r r)k_r dk_r, \end{cases} \tag{5.38}$$

for $i = 1, 2$.

Note the way $U_{ri}^m(r, z_0)$ and $U_{\theta i}^m(r, z_0)$ are represented. Only the combinations of them give us single Bessel function orders in the integral. Of course, we can choose the representation arbitrarily, which corresponds to different definition of $R_i^m(k_r, z_0)$ and $\Theta_i^m(k_r, z_0)$. But $U_{ri}^m(r, z_0)$ and $U_{\theta i}^m(r, z_0)$ alone will introduce at least two orders of Bessel functions in the integral, which would severely complicate the expression and calculation. [62, 60]

Now, the displacement discontinuities is represented in Cartesian coordinate system as

$$\vec{u}(x, y, z_0) = \hat{e_x} u_x(x, y, z_0) + \hat{e_y} u_y(x, y, z_0) + \hat{e_z} u_z(x, y, z). \tag{5.39}$$

We proceed by taking the 2-Dimensional Fourier Transform to get

$$\tilde{\vec{U}}(k_x, k_y, z_0) = \hat{e_x}\tilde{U_x}(k_x, k_y, z_0) + \hat{e_y}\tilde{U_y}(k_x, k_y, z_0) + \hat{e_z}\tilde{U_z}(k_x, k_y, z_0), \tag{5.40}$$

then change variables from (k_x, k_y, z_0) to (k_r, β, z_0) and expand into Fourier series:

$$\begin{cases} \tilde{U_x}(k_r, \beta, z_0) = \sum_m [\tilde{X_1}^m(k_r, z_0) cos(m\beta) + \tilde{X_2}^m(k_r, z_0) sin(m\beta)]; \\ \tilde{U_y}(k_r, \beta, z_0) = \sum_m [\tilde{Y_1}^m(k_r, z_0) sin(m\beta) - \tilde{Y_2}^m(k_r, z_0) cos(m\beta)]; \\ \tilde{U_z}(k_r, \beta, z_0) = \sum_m [\tilde{Z_1}^m(k_r, z_0) cos(m\beta) + \tilde{Z_2}^m(k_r, z_0) sin(m\beta)]. \end{cases} \tag{5.41}$$

It can be shown that (see Appendix C) there is a very simple relationship between the expansion coefficients in cylindrical (Eq. (5.38)) and Cartesian (Eq. (5.41)) coordinate systems:

$$\begin{cases} Z_i^m(k_r, z_0) = 2\pi(-i)^{m\pm1} \tilde{Z_i}^m(k_r, z_0), \\ R_i^m(k_r, z_0) \pm \Theta_i^m(k_r, z_0) = 2\pi(-i)^{m\pm1} [\tilde{X_i}^{m\pm1}(k_r, z_0) \pm \tilde{Y_i}^{m\pm1}(k_r, z_0)], \end{cases} \tag{5.42}$$

where $i = 1, 2$.

5.5.4 Summary

To summarize, the algorithm is shown in Fig. 5-2.

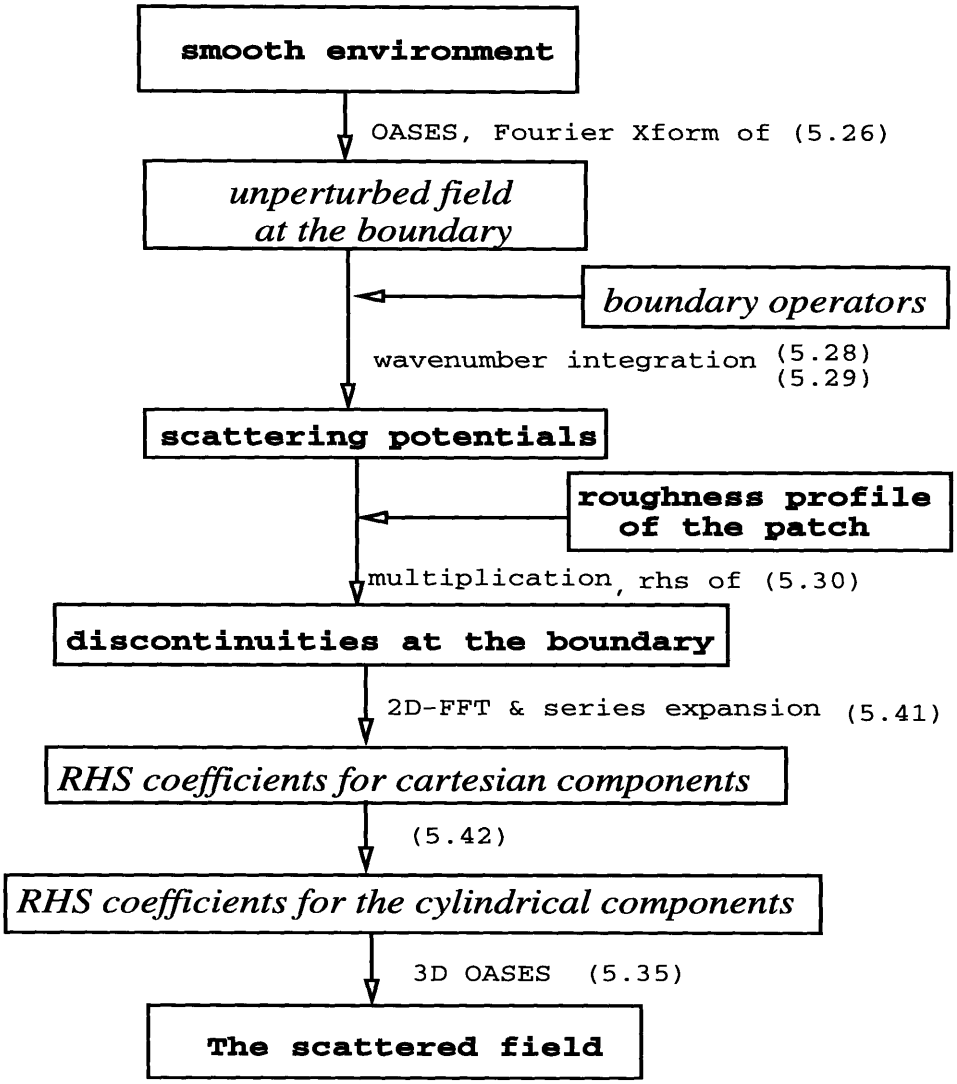

Bold - functions in spatial domain
Italic - functions in wavenumber domain

Figure 5-2: The Algorithm For Calculating the Scattered Field From a Rough Interface Patch, Using Hybrid Wavenumber-Spatial Domain Method

Chapter 6

Numerical Simulations of Three-Dimensional Diffuse Scattering from a Rough Interface Patch

In this chapter, we will use the model developed in last chapter to investigate the acoustic scattering from a rough interface patch. First, we discuss how to characterize and simulate the rough interfaces. Then, a deep water environment representing some scenarios in the ARSRP experiment is considered. How the roughness statistics affect the inherently 3-D scattering pattern is examined. In the following section, shallow water scenarios are considered, highlighting the waveguide effects on the scattering from the rough patch. The final section is engaged to the discussion of Lambert's law: its validity and its relationship with the roughness statistics and bottom material.

6.1 Simulating the Rough Interface

Representing the rough interface in the ocean environment is an interesting issue. We have quite good understanding of the mechanism that caused and continues to change the landscape of the seabed at scales larger than tens of kilometers, and

accurate bathymetry maps are available. But for small scale profiles, life is not that easy. First of all, to have accurate bathymetry maps with fine details, tremendous efforts are required. A global survey is impossible beyond a certain resolution. And again, no matter how fine the existing maps are, there are always finer details that are not covered.

A more important question is : is it worthwhile to produce such a fine scale map? The answer is **No**. The fine details of the ocean bottom are constantly changing. Unlike large scale features such as seamounts and fault scarps that stay constant for quite a long time, small scale features are changing so fast that the aforementioned map will be outdated very soon. To make matters worse, we are not sure how they evolve.

The only resort for the description of the small scale features is **statistical approach**. As Mandelbrot put it [49]:

"...the goal of achieving a full description is hopeless, should not even be entertained. In physics, for example the theory of Brownian motion, the key out of this difficulty lies in statistics. In geomorphology, statistics is even harder to avoid. Indeed, while the laws of mechanics affect molecular motion directly, they affect geomorphological patterns through many ill-explored intermediaries. Hence, even more than the physicist, the geomorpologist is compelled to forsake a precise description of reality and to use statistics."

Goff and Jordan [28] developed a stochastic model for the estimation of seafloor statistics that takes into account the finite precision, resolution, and sampling obtained by actual echo sounding systems. They modeled the seafloor as a stationary, zero-mean, Gaussian random field completely specified by its autocovariance function.

First, a bathymetry function $b(\vec{x})$ is introduced. It is defined as the depth of the seafloor as a function of the coordinate vector $\vec{x}$, which ranges over a two-dimensional domain M. Represented on the map $b(\vec{x}) : \vec{x} \in M$ will be the large scale bathymetric information associated with plate subsidence, major volcanoes, seismic ridges, oceanic plateaus, abyssal plains, the larger fracture zones, etc., as well as small scale features such as abyssal hills, small volcanic cones, lava flows, and sediment ponds. As we

mentioned earlier, geologically, the large scale features can be treated in a deterministic point of view. And acoustically, their scattering effect can be modeled by facet scattering models, provided their dimensions are close to the wavelength.

The small features, as aforementioned, are too variant to be treated deterministically, and numerous enough to be represented by their ensemble properties.

Thus the bathymetric function $b(\vec{x})$ can be partitioned into deterministic component $b_0(\vec{x})$ and a stochastic component $h(\vec{x})$:

$$b(\vec{x}) = b_0(\vec{x}) + h(\vec{x}). \tag{6.1}$$

The small scale seafloor topography is considered to be a random field, generalizing $h(\vec{x})$ from a particular function to a two dimensional stochastic process specified by a joint probability density function $f(h(\vec{x_1}), h(\vec{x_2}), ... : \vec{x_1}, \vec{x_2}, ... \in M)$.

Now, for stochastic modeling to be practicable, the statistics of $h(\vec{x})$ must be approximated as being spatially homogeneous or stationary. This is a tricky assumption. Obviously, the ocean bottom landscape varies. Not only the shapes of bathymetry change from area to area, more importantly, the trend and characteristics change, i.e., the stochastic process is by no means spatially stationary. But arguably we can assume that the change of the stochastic process is a function of the distance.

So, in the use of the stochastic model we should be extremely careful. The region over which the bathymetry is assumed stationary should be neither too large or too small. It has to be small enough so that the stationary assumption is still a good approximation. On the other hand, the region has to be large enough so that the stochastic ensemble of the bathymetry function is big enough to ensure the estimation of the parameters can be done with adequately small uncertainty.

The expected value of the bathymetry is taken to be the reference surface $b_0(\vec{x})$, so the topography $h(\vec{x})$ is defined to be a zero-mean process:

$$\langle h(\vec{x}) \rangle = \int_{-\infty}^{\infty} h(\vec{x}) f(h(\vec{x})) dh = 0. \tag{6.2}$$

Its higher-order properties are contained in the N-point moment functions

$$C_N(\vec{x_1},...,\vec{x_N}) = \langle h(\vec{x_1})...h(\vec{x_N})\rangle = \int_{-\infty}^{\infty}...\int_{-\infty}^{\infty} h_1...h_N f(h_1,...,h_N)dh_1...dh_N, \quad (6.3)$$

where $h_n = h(\vec{x_n})$.

As we assume the process is spatially stationary, the moments of seafloor topography are invariant with respect to spatial translation,

$$C_N(\vec{\xi}+\vec{x_1},...,\vec{\xi}+\vec{x_N}) = C_N(\vec{x_1},...,\vec{x_N}). \quad (6.4)$$

Because of this translational symmetry we can invoke an ergodic hypothesis to identify spatial averages with ensemble averages. That is, for any fixed set $\vec{x_n}$ we can construct an unbiased estimator of the form

$$\tilde{C_N}(\vec{x_1},...,\vec{x_N}) = \frac{1}{A}\int_M h(\vec{\xi}+\vec{x_1})...h(\vec{\xi}+\vec{x_N})dA(\vec{\xi}), \quad (6.5)$$

where the domain of integration M has an area A.

The Goff-Jordan model considers Gaussian processes. So the process is fully described by its first two moments. As mentioned earlier, the first moment, i.e., the expected value of the random part of the depth, is zero by definition. So that leaves us only the two - point moment, or autocovariance function. Translation symmetry allows us to write

$$C_{hh}(\vec{x}) = C_2(\vec{\xi},\vec{\xi}+\vec{x}) = \langle h(\vec{\xi})h(\vec{\xi}+\vec{x})\rangle. \quad (6.6)$$

Hence, for a stationary process, the autocovariance function depends only on the spatial lag vector $\vec{x}$. Given the autocovariance and the zero mean, the joint probability density function for $h_1 = h(\vec{x_1})$ and $h_2 = h(\vec{x_2})$ is

$$f(h_1,h_2) = \frac{1}{2\pi H^2\sqrt{1-\rho_{hh}^2}} e^{-\frac{h_1^2 - 2\rho_{hh}h_1h_2 + h_2^2}{2H^2(1-\rho_{hh}^2)}}, \quad (6.7)$$

where $\rho_{hh} \equiv H^{-2}C_{hh}(\vec{x_1}-\vec{x_2})$ is the correlation coefficient.

Alternatively, the Gaussian process can be specified by its power spectrum

$$P_h(\vec{k}) = \int_{-\infty}^{\infty}\int_{-\infty}^{\infty} C_{hh}(\vec{x})e^{-i\vec{k}\bullet\vec{x}}d^2\vec{x}. \tag{6.8}$$

A good model for the functional form of the power spectrum $P_h(\vec{k})$ or the auto-covariance $C_{hh}(\vec{x})$ should capture the general trends [1], and the parameters should be linked intuitively to the geological attributes of the rough interface. The reason we use Goff-Jordan [28] model is that they did a good job on this, as shown below.

They proposed the functional form of the power spectrum as

$$P_h(\vec{k}) = 4\pi\nu H^2 \frac{1}{\sqrt{\mid Q \mid}} \frac{1}{[u^2(\vec{k})+1]^{(\nu+1)}}. \tag{6.9}$$

In Eq. (6.9), Q is a positive-definite, symmetric matrix whose Cartesian elements q_{ij} have dimensions of $(length)^{-2}$. It can be expressed in terms of its normalized eigenvectors $\vec{e_n}$ and $\vec{e_s}$ and its ordered eigenvalues $k_n^2 \leq k_s^2$,

$$Q = k_n^2\vec{e_n}\vec{e_n}^T + k_s^2\vec{e_s}\vec{e_s}^T. \tag{6.10}$$

The Q matrix carries information about the orientation of the anisotropy of the random part of the bathymetry process. Specifically, $\vec{e_s}$ is the direction of the maximum correlation length, $\vec{e_n}$ the minimum, and k_s and k_n correspond to the inverses of the maximum and minimum correlation lengths respectively.

In Eq. (6.9) u is the dimensionless norm of $\vec{k}$ defined in terms of its modulus k and azimuth ζ,

$$u(\vec{k}) = [\vec{k}^T Q^{-1}\vec{k}]^{1/2} = \sqrt{(\frac{k}{k_s})^2 cos^2(\zeta-\zeta_s) + (\frac{k}{k_n})^2 sin^2(\zeta-\zeta_s)}, \tag{6.11}$$

[1] otherwise, too many parameters have to be introduced and estimated, and the use of the model becomes forbiddenly cumbersome. In fact, a model with infinite parameters can be fit on any experimental result. Then the introduction of the model doesn't say anything about the physics of the reality. On the other hand, too few parameters leave too few degrees of freedom. In effect, too much physics was read into the model. As a result, it would be too restrictive to have a meaningful range of validity. When constructing a model, we should say something about the physics, but not too much. The tradeoff is an art. It partly depends on the intended scope of the model.

where ζ_s is the azimuth of $\vec{e_s}$.

The roll-off rate of the power spectrum $-2(\nu + 1)$ can be related to the fractal (Hausdorff) dimension of such a stochastic process D as:

$$D = 3 - \nu. \tag{6.12}$$

Hence, decreasing the parameter ν increases the roughness, with the limiting cases of unity and zero corresponding to a random field with continuous derivative (Euclidean surface, D=2) and one which is "space-filling" (Peano surface, D=3), respectively. In this thesis, it is assumed that the rough interface has fractal dimension 2.

So, in the Goff-Jordan model, the random process of the bathymetry is fully described by the topographic amplitude H, orientation of the anisotropicity ζ_s, characteristic scale lengths of the elongations λ_s and λ_n, and the fractal dimension of seafloor roughness D.

In this chapter, we will consider five different roughness statistics. Their parameters are given below. For the sake of identifying, they are named "A", "B", "C", "D" and "E".

Table 6.1: The parameters for the roughness statistics used in this chapter.

statistics .	correlation length along major axis	correlation length along minor axis	RMS height	angle between maj. axis and X	fractal dimension
A	15m	15m	1m	45 deg.	2
B	20m	5m	1m	45 deg.	2
C	80m	1m	1m	45 deg.	2
D	80m	20m	1m	45 deg.	2
E	4m	1m	1m	45 deg.	2

6.2 The Deep Water Scenario with Beam Incidence

The first example concerns a ocean environment representing some scenarios in the Acoustic Reverberation Special Research Project (ARSRP) experiment. The water column is 4km deep and is assumed to be horizontally stratified, with the sound speed profile as measured in the experiment. A roughness area of size 150 meters by 150 meters is located at the water column/sea bed interface. The roughness profile is assumed to satisfy the Goff-Jordan statistics with fractal dimension 2 (Euclidean surface) and RMS height 1 meter [28]. To eliminate the edge effect, we apply a Hanning window on the roughness profile. (Fig. 6-1) A beam is insonified on the rough patch. The beam pattern has a wedge like shape, with its axis parallel to the y axis, and Gaussian tappered in the X-Z plane. The center beam aims at the center of the patch and has a 6^0 grazing angle. The insonification of the beam is shown in Fig. 6-2.

6.2.1 The Isotropic Patch Case

First we consider an isotropic patch. The correlation length is assumed to be 15 meters in both X and Y directions. We call this roughness statistics statistics A. A realization of the patch profile with statistics A is shown in Fig. (6-3) (profile A1). The scattered pressure field at 150m above the interface is shown in Fig. (6-4). Pressure in decibel is represented in color scale, which is plotted as a function of X ranges and Y ranges from the center of the patch. The result is normalized such that the insonification pressure is 1 at the center of the patch. We can see that the scattered pressure field is symmetric along the direction of the incoming wave (positive X axis), which is what we expected.

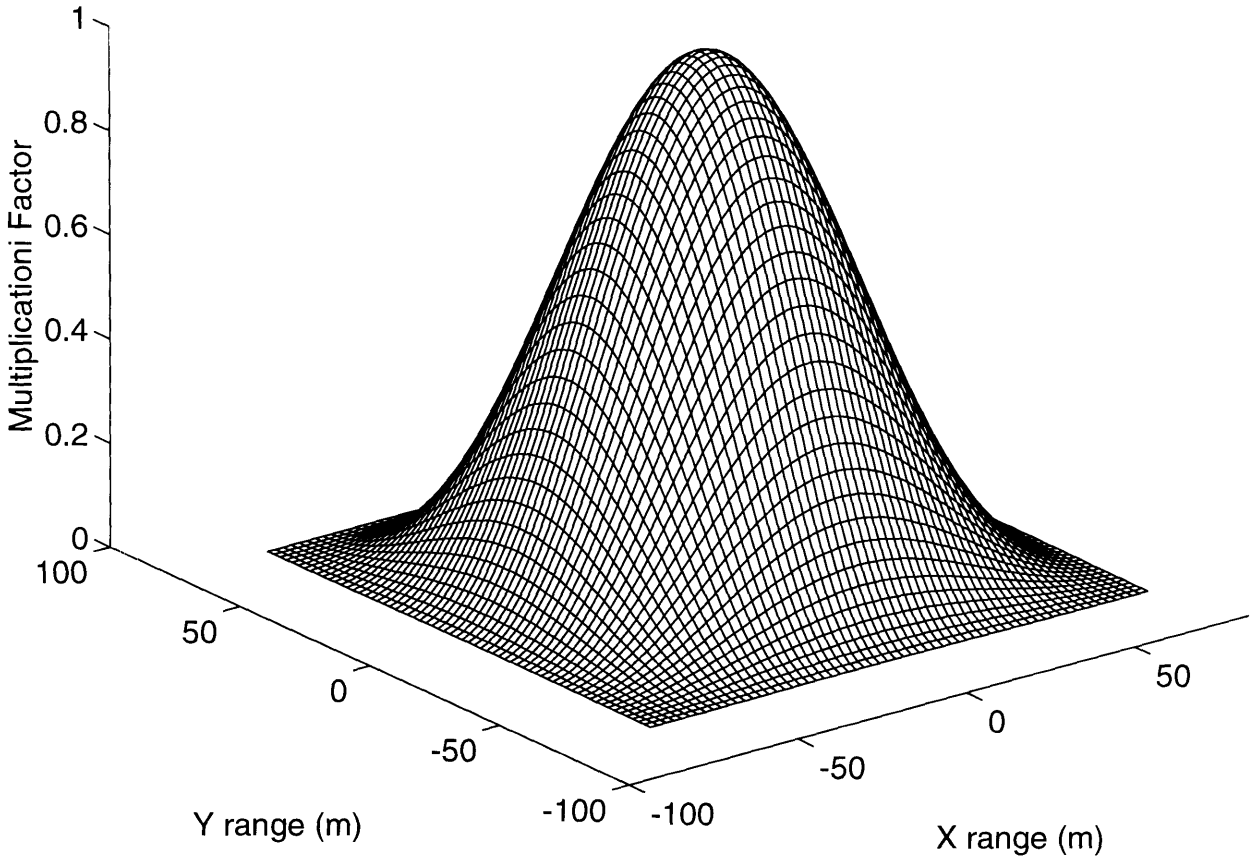

Figure 6-1: The Hanning Window Applied on the Rough Patch to Reduce the Edge Effect

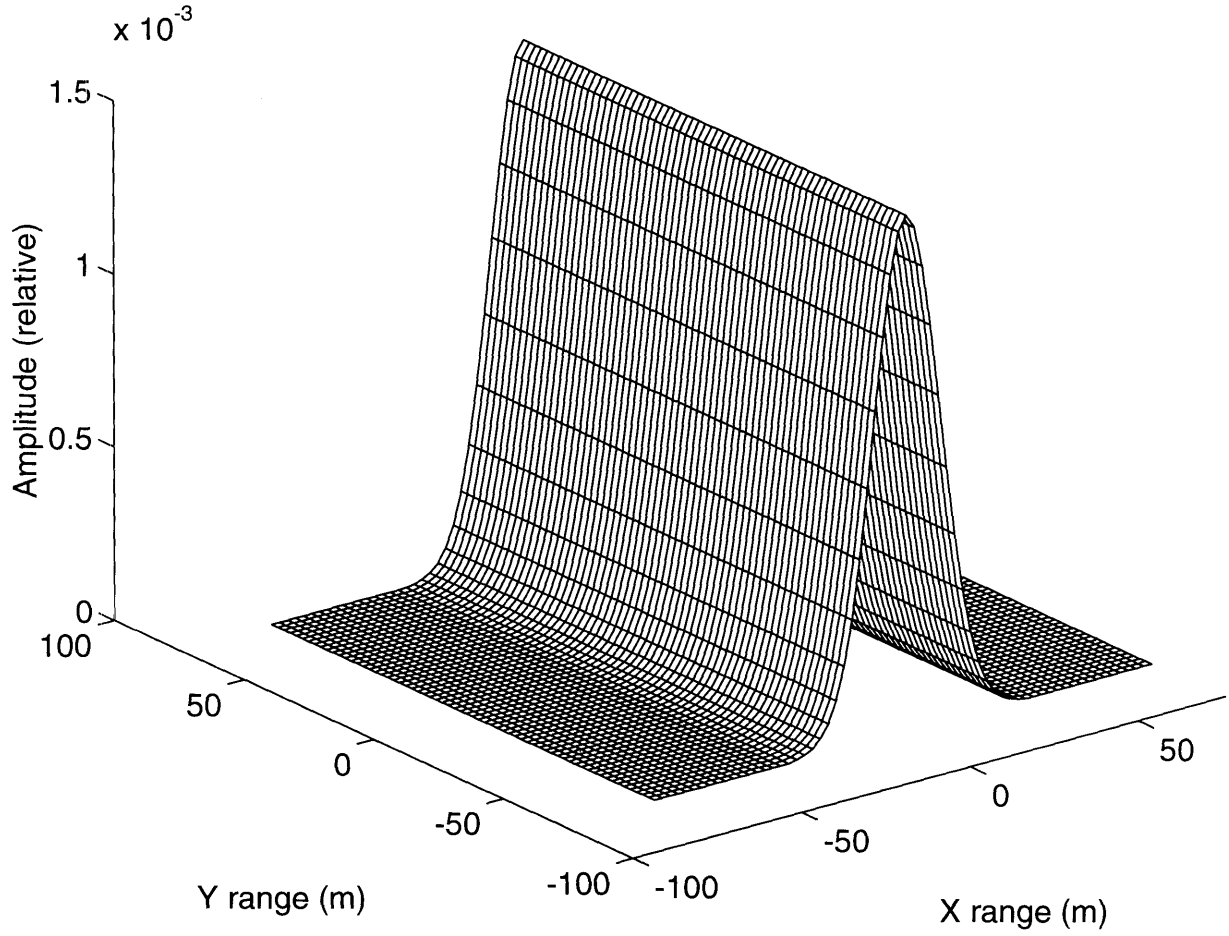

Figure 6-2: The Insonification on the Patch. This is Before the Normalization

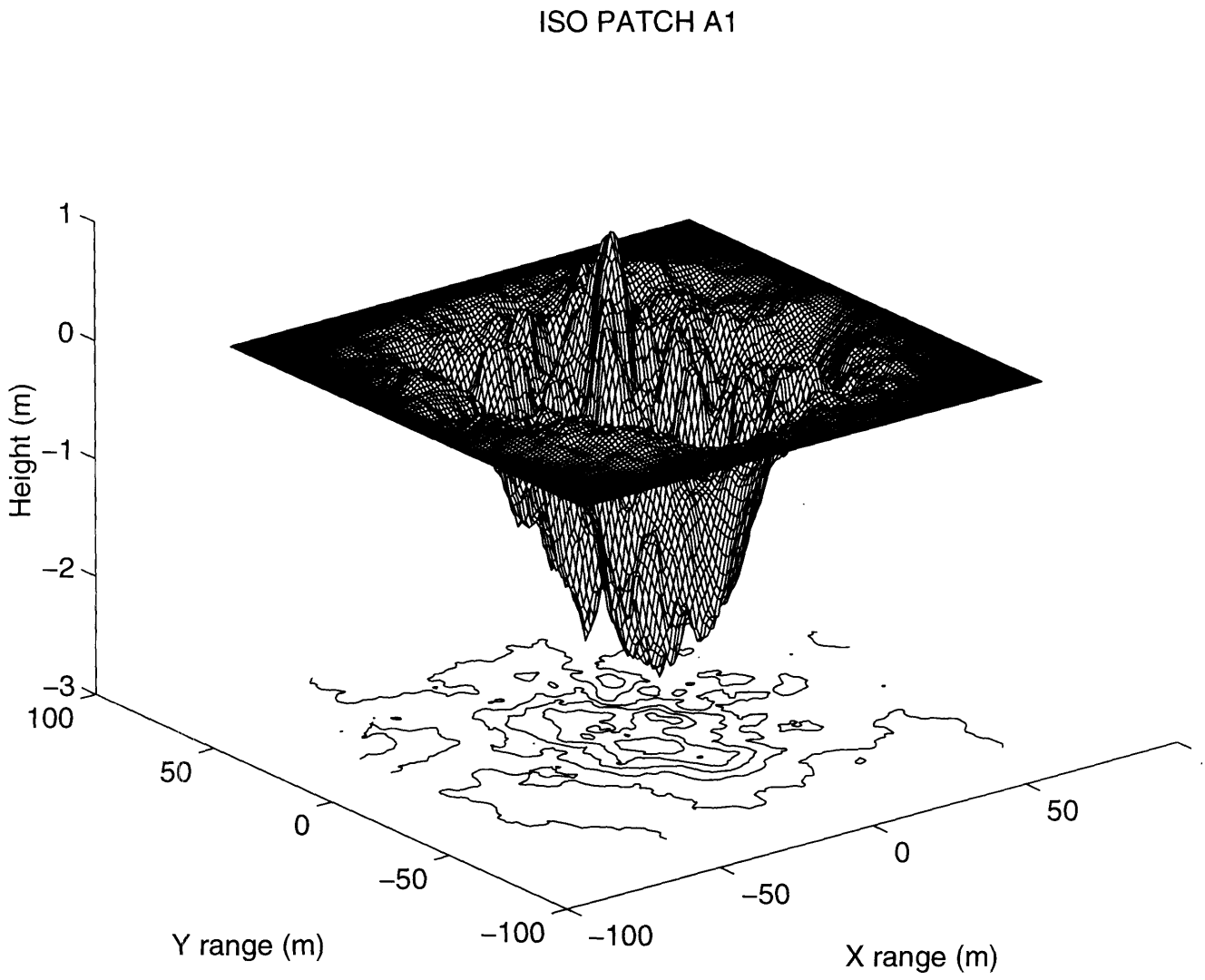

Figure 6-3: The Rough Patch Realization A1. Isotropic with Correlation Length of 15m in All Directions.

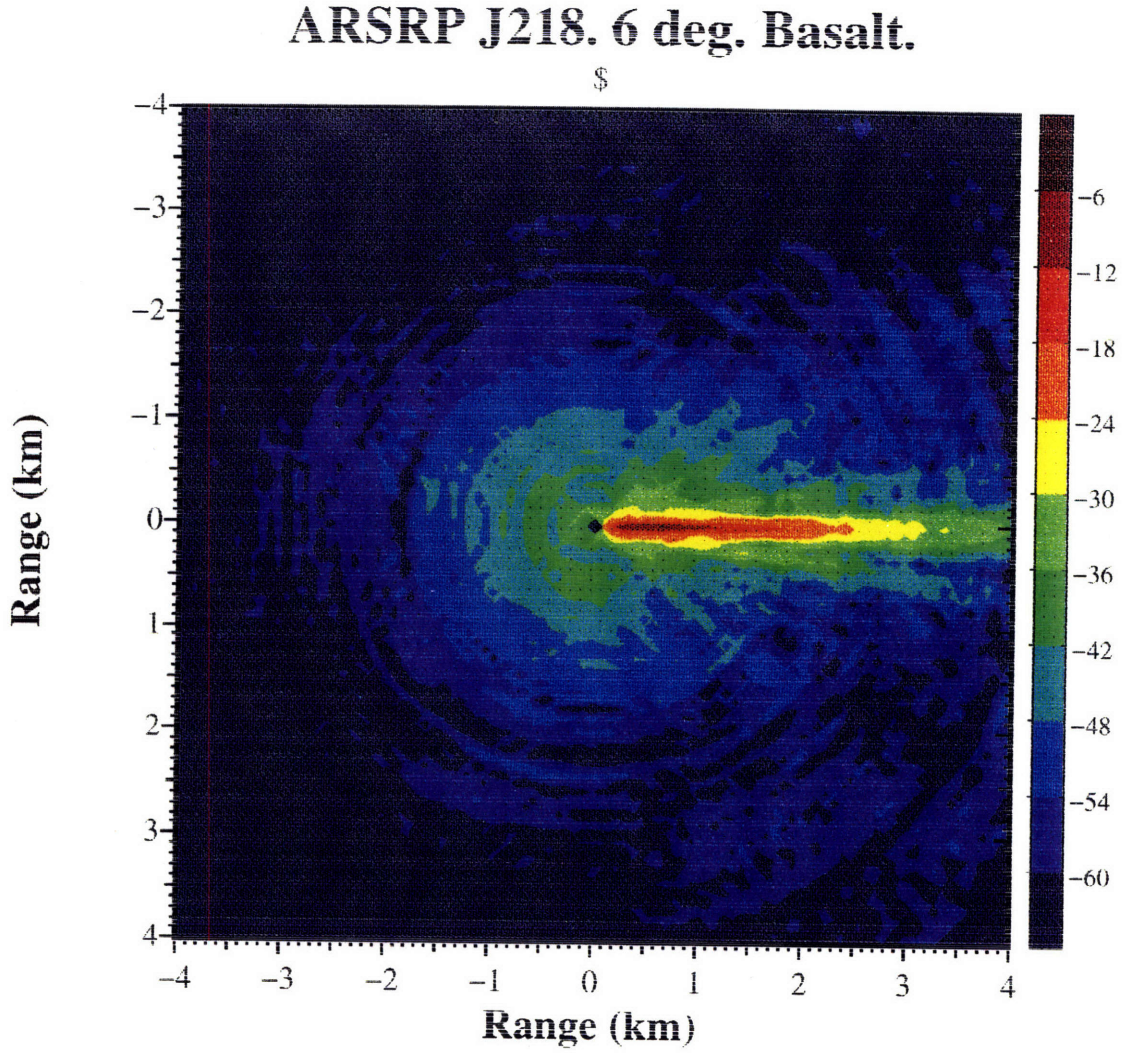

Figure 6-4: The Scattered Pressure Field 150m above the Bottom in the ARSRP Ocean Environment. Beam centered at 6 degree grazing insonifies on the rough patch A1.

6.2.2 The Anisotropic Patch

Now, we consider an anisotropic patch whose main axis lies at 45^0 away from X axis with correlation lengths 20 meters and 5 meters in the main and minor axes respectively (roughness statistics B). A realization is shown in Fig. (6-5). Again, the scattered pressure field at 3850m depth (i.e. 150m above the bottom) is calculated and shown in Fig. (6-6). It is obvious that the anisotropy of the patch "steered" part of energy out-of plane, which can not be adequately accounted for using a 2 dimensional model. It is interesting to note that the dominating scattering is in the first quadrant, that is, along the alignment of the roughness features of the patch. It should be reiterated that it is the one REALIZATION of the roughness profile out of the probability space that generates this result. We can in no means draw any conclusion in a statistically certain manner from such one result. Thus we use the same stochastic process to generate another realization of th e patch (B2) (Fig. 6-7) and calculate the scattered fields at the same depth, which is shown in , Fig. 6-8. We can see the same "steering" effect.

6.2.3 Strongly Anisotropic Patch

To isolate important features from the other complicated scattering pattern, we run another strongly delineated case, where the correlation length along the major and minor axis on the patch are 80m and 1m respectively. The major axis is still at 45^0 from X axis (statistics C). One particular realization is shown in Fig. 6-9 (patch C1). As seen on the image of the patch, the roughness features are strongly lineated and form very long and narrow valleys. The scattered field 150m above the bottom is shown in Fig. 6-10. It is very "clean", with few strong features in geometrically special locations. The strong scattering in the X and Y direction are easy to understand physically. They correspond to the shadow effect and the specular reflection respectively.

If we think of the strongly lineated features in the patch as cylinders lying in the 45^0 direction, we will expect the two group of scattered beams in the forward direction,

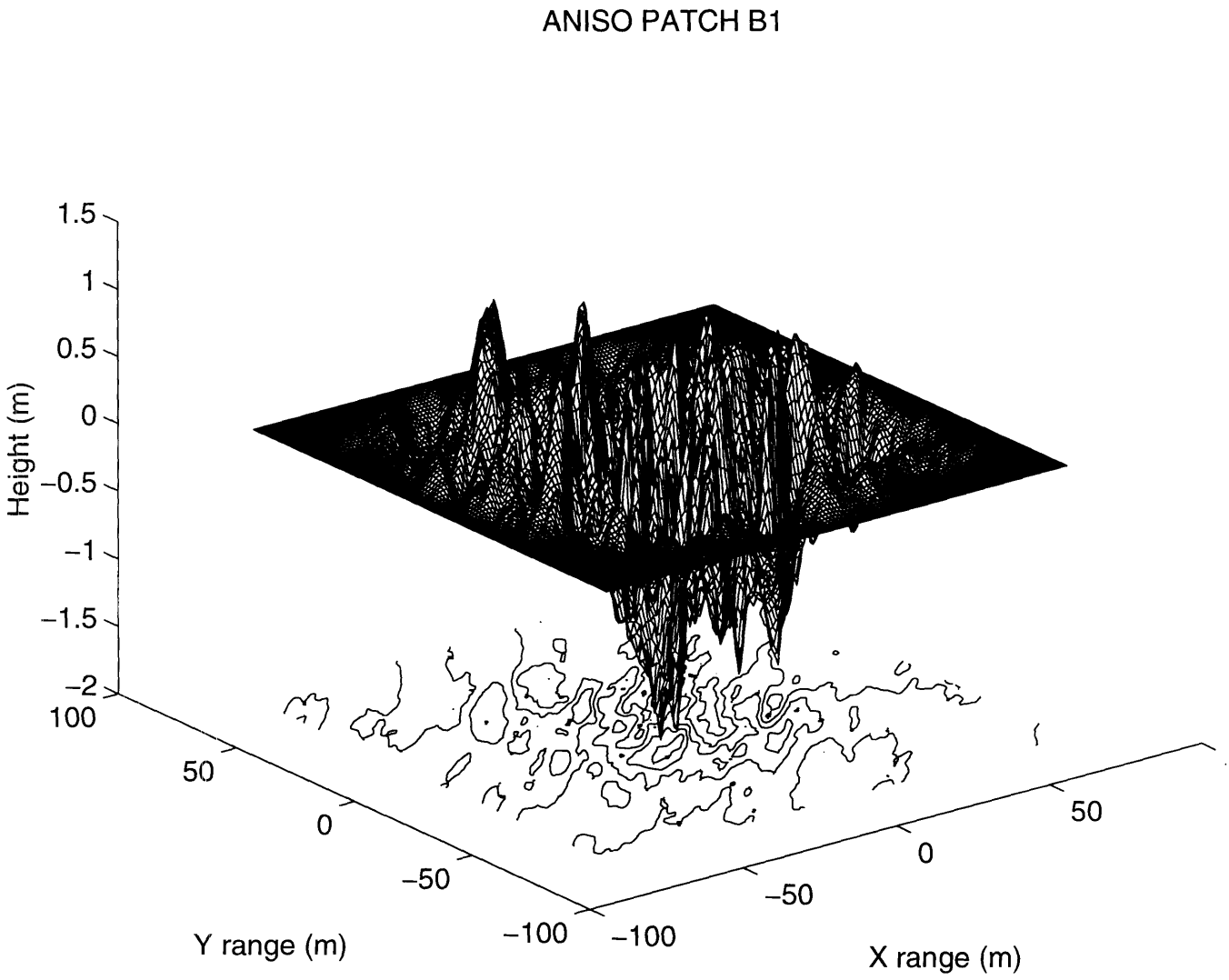

Figure 6-5: The Anisotropic Rough Patch Realization B1. Correlation Lengths of 20m and 5m Along the Major and Minor Axes

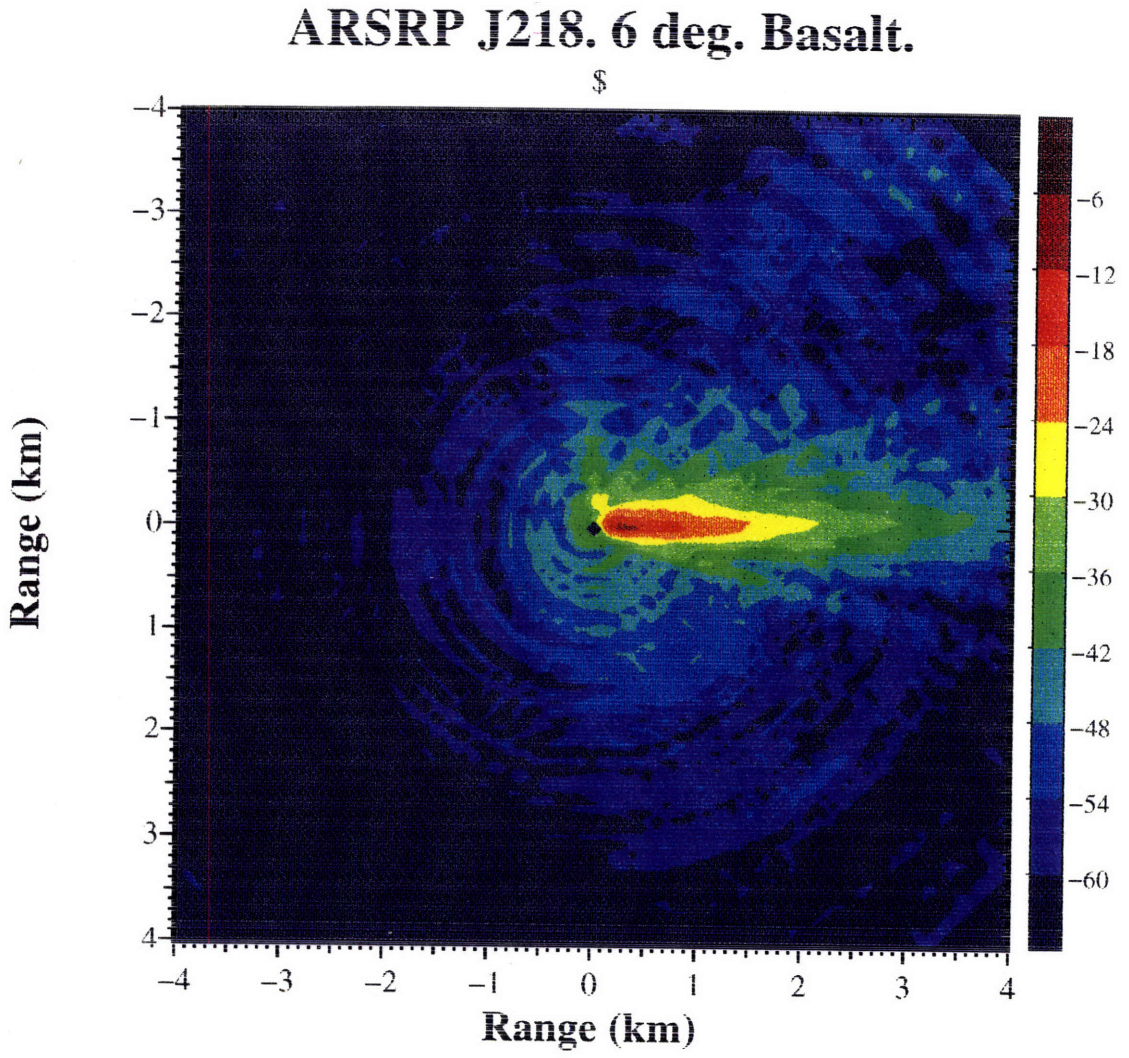

Figure 6-6: The Scattered Pressure Field 150m above the Bottom in ARSRP Environment. Beam centered at 6 degree grazing insonifies on the rough patch B1.

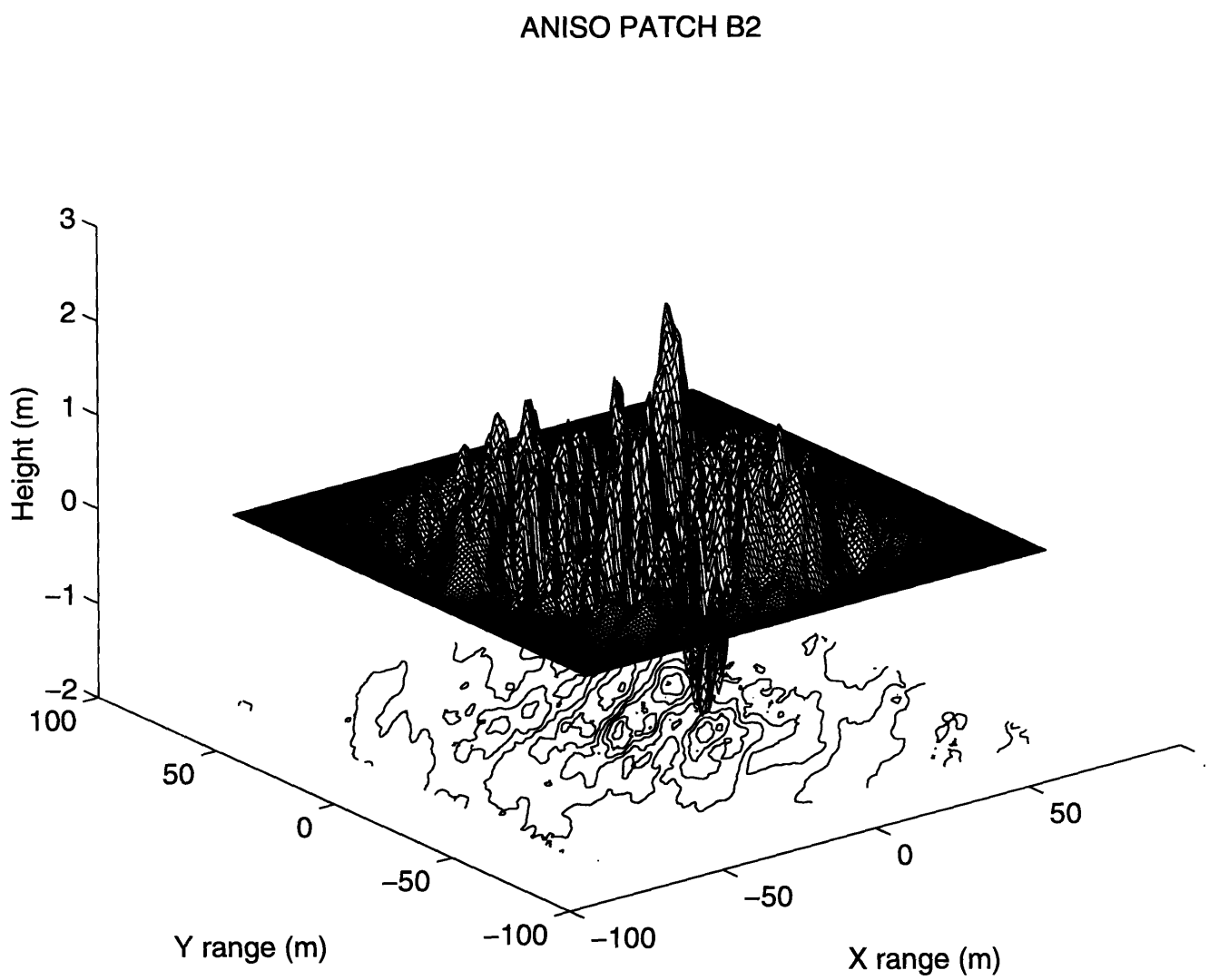

Figure 6-7: The Anisotropic Rough Patch Realization B2. Correlation Lengths of 20m and 5m Along the Major and Minor Axes

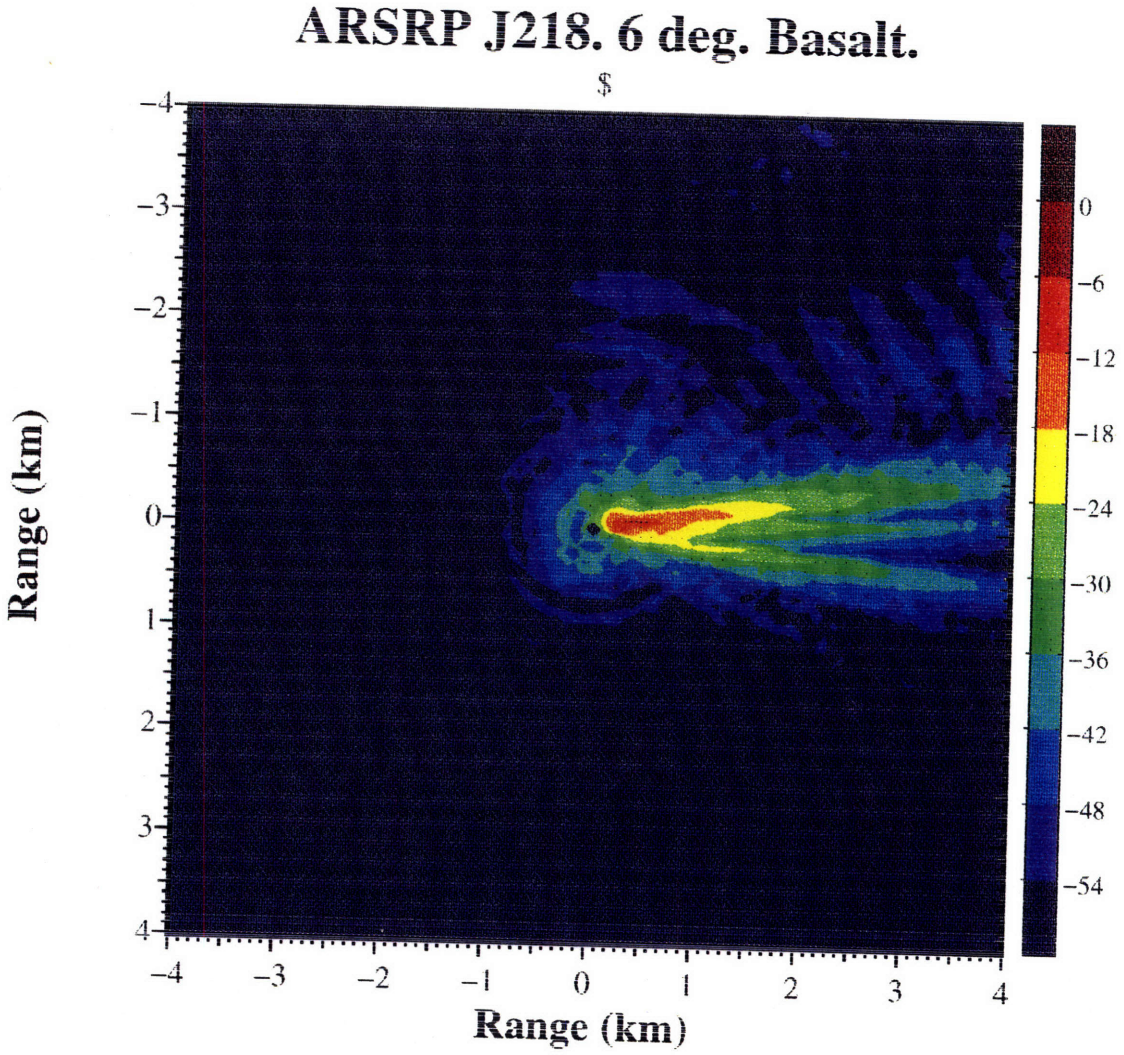

Figure 6-8: The Scattered Pressure Field 150m above the Bottom. Beam centered at 6 degree grazing insonifies on the rough patch B2.

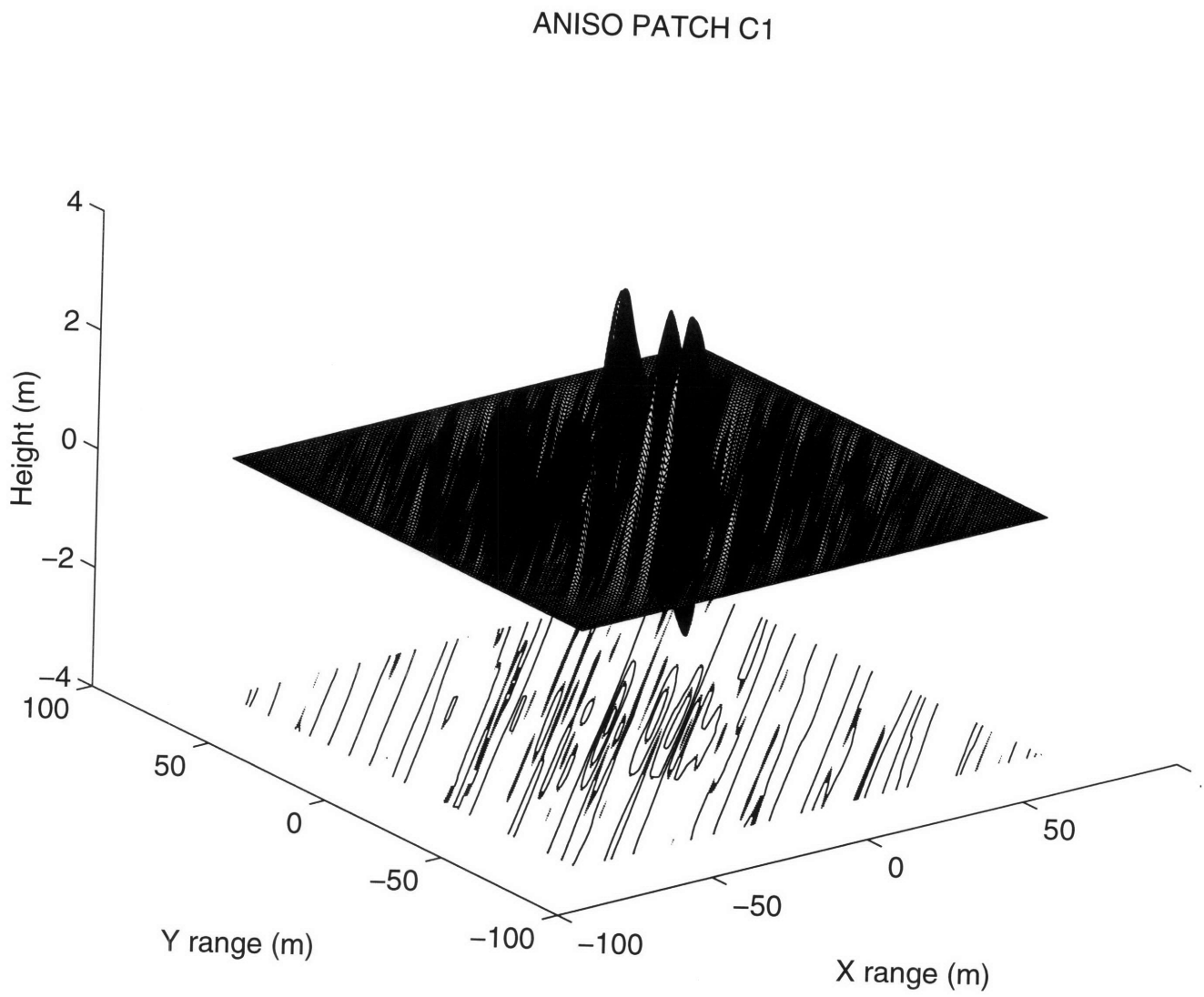

Figure 6-9: The Strongly Anisotropic Rough Patch Realization: C1. Correlation lengths are 80m and 1m along the major and minor axes

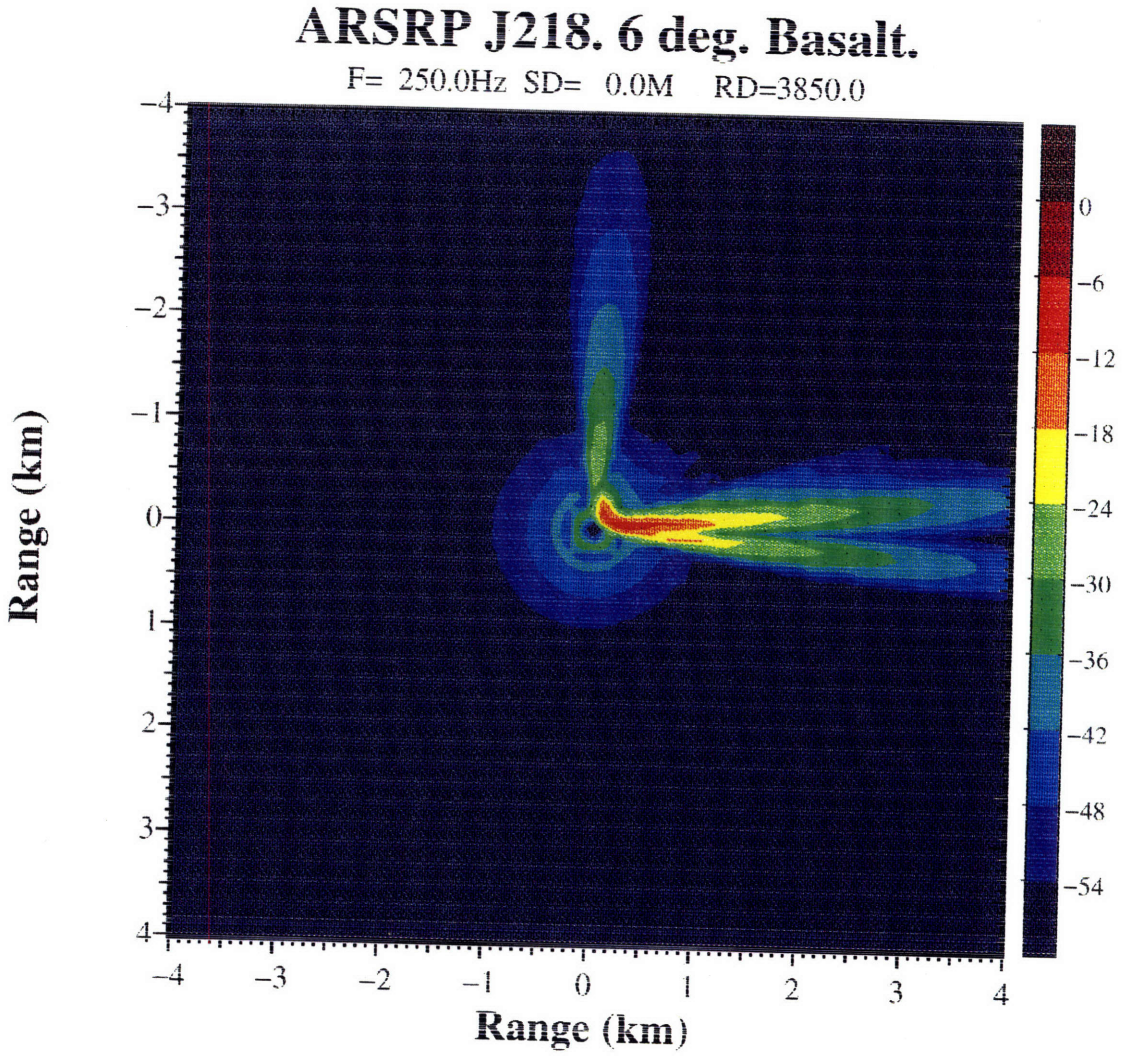

Figure 6-10: The Scattered Pressure Field 150m above the Bottom in ARSRP Ocean Environment. Beam centered at 6 degree grazing insonifies on the rough patch C1.

just as observed in the sediment covered ridge case in Chapter 4 (Fig. 4-14).

6.2.4 Average Over Realizations

As we mentioned, our model computes the scattered field from particular realizations of the rough patch. It is arguable that some of features we observed in the previous result might have very small probability of occurrence and might not be statistically significant at all.

To address that question, we generate 10 realizations for each of the three roughness power spectra used above, and compute the resulting scattered fields. The average scattered pressure fields at 150m above the bottom are shown in Fig. 6-11, Fig. 6-12, Fig. 6-13. From these figures we can see that the basic features we mentioned are still there. Of course, the details are different. So, we conclude that the power spectrum of the rough interface patch is the decisive factor at shaping up the pattern of scattering, while the details of the scattered field depend on the particular realization.

6.3 Shallow Water Scenarios: The Waveguide Effects

In this section, we examine the scattering and reverberation effects of the rough patch with the presence of the waveguide.

In the deep ocean scenarios presented in last section, the upper surface has little effect in the reverberation field until at very far field. But in shallow water, the upper boundary plays an important role in the scattering and reverberation. Here, the waveguide not only affects the propagation of the scattered waves, but also affects the excitation of different scattered waves. Waveguide and roughness scattering forms an integral problem. This is exactly the strength of our approach.

The environment we consider is as following: 20m deep water column with compressional sound speed of $1530 m/s$ and density of $1 g/cm^3$. Beneath is elastic bottom

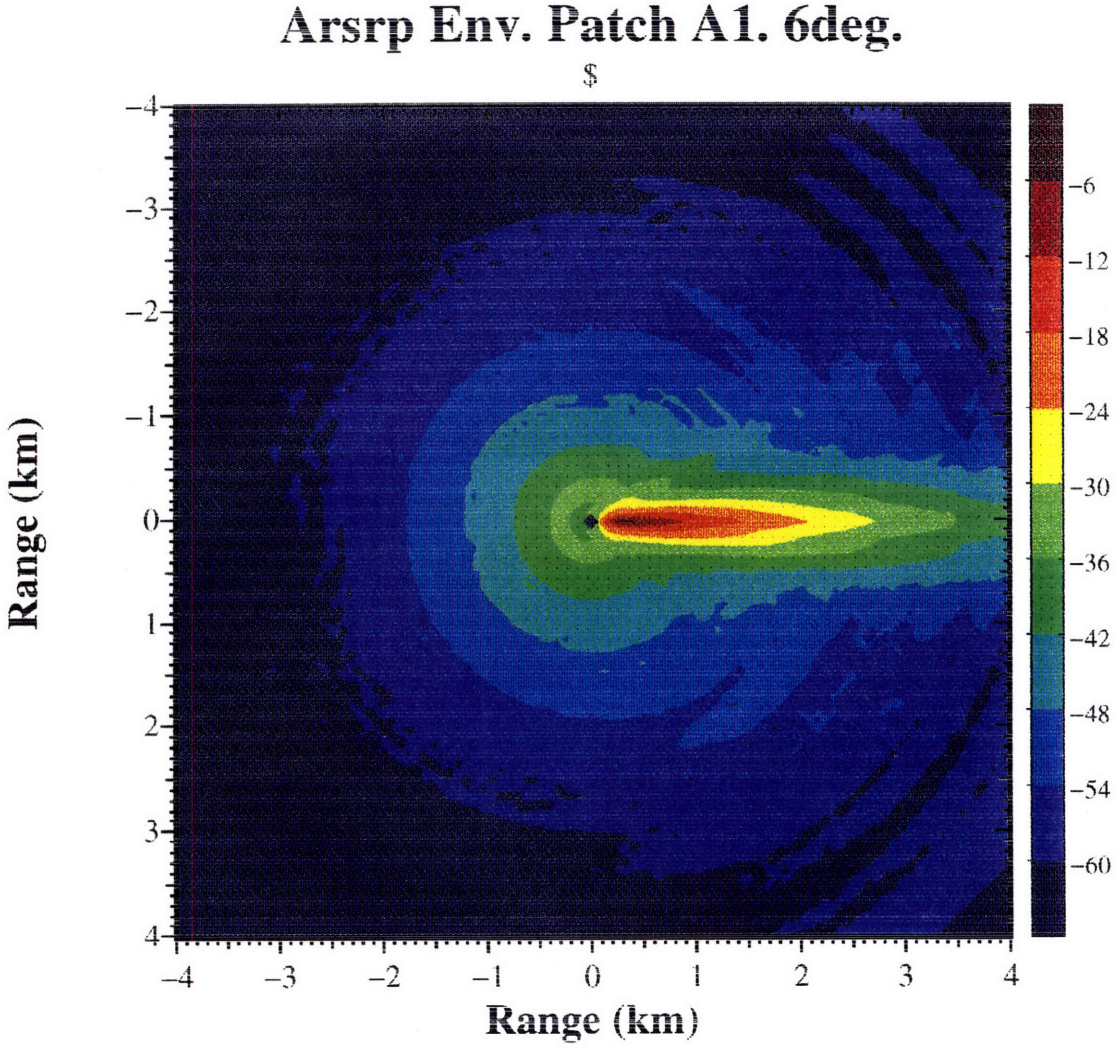

Figure 6-11: The Average Scattered Pressure Field Over Ten Realizations with Roughness Spectrum A. The field is at 150m above the bottom in the ARSRP ocean environment. Beam incidence centered at 6 degree grazing.

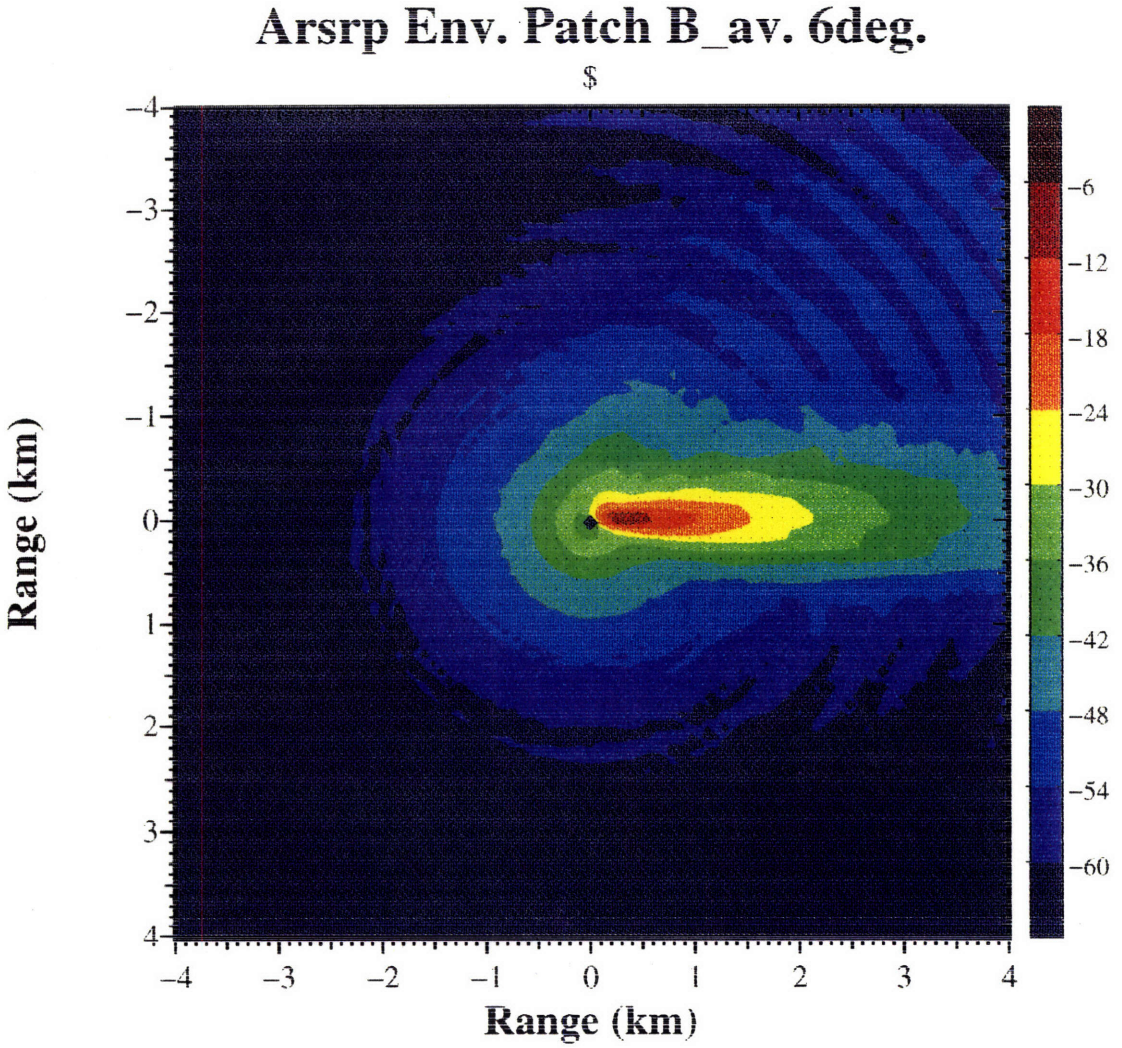

Figure 6-12: The Average Scattered Pressure Field Over Ten Realizations with Roughness Spectrum B. The field is at 150m above the bottom in the ARSRP ocean environment. Beam incidence centered at 6 degree grazing.

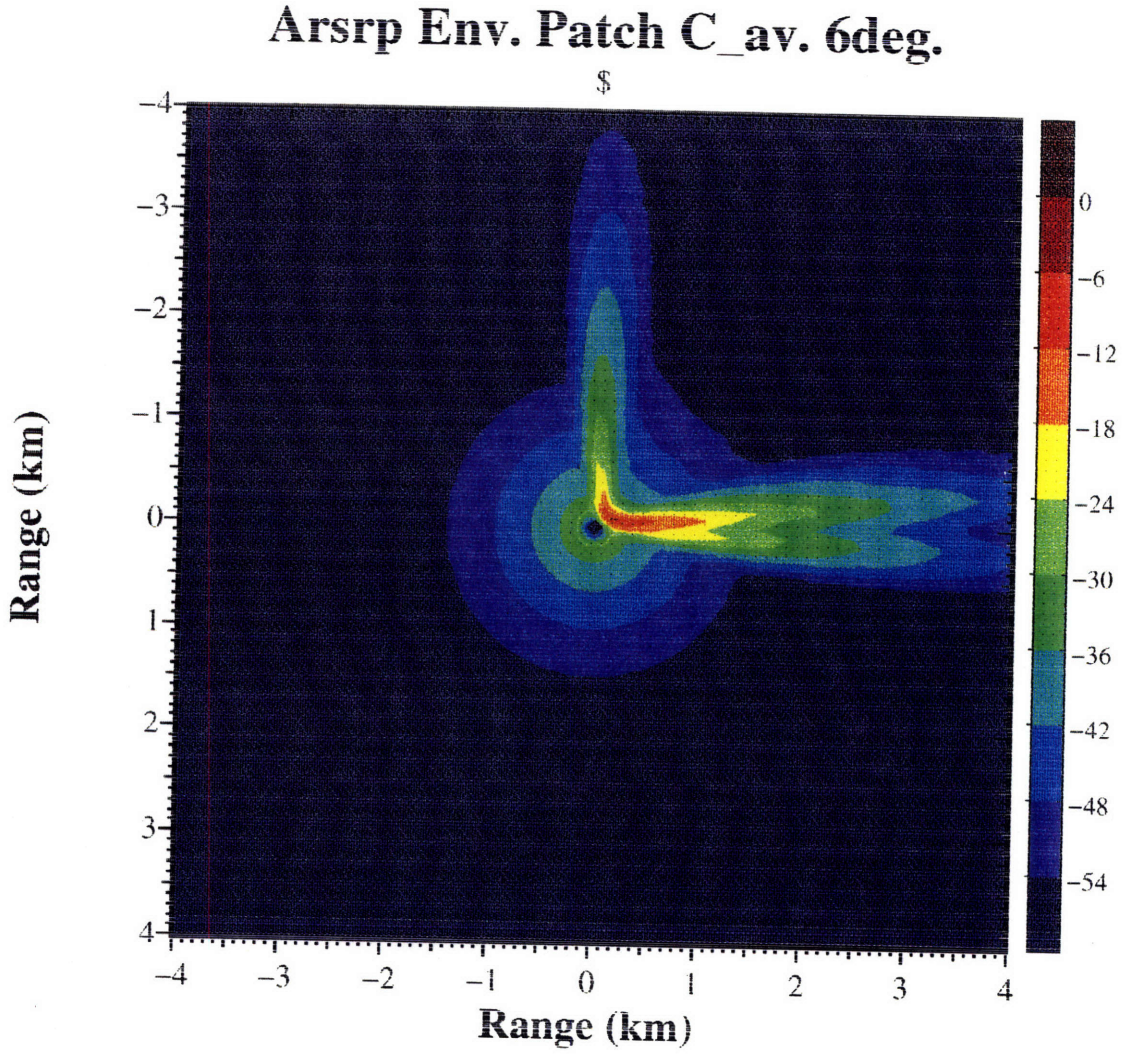

Figure 6-13: The Average Scattered Pressure Field Over Ten Realizations with Roughness Spectrum C. The field is at 50m above the bottom in the ARSRP ocean environment. Beam incidence centered at 6 degree grazing.

with compressional sound speed of $5200m/s$, shear sound speed of $2500m/s$ and density of $2.4g/cm^3$. The water is assumed lossless and the elastic bottom has compressional attenuation of $0.2dB/\Lambda$ and shear attenuation of $0.5dB/\Lambda$. We used the patch B1(see Fig. 6-5) throughout this section.

In contrast to the deep ocean scenario, where a beam is the natural way to describe the acoustic wave propagation, in the shallow water waveguide scenario, a modal description should be used. So, instead of have a beam insonification on the patch, a single mode is generated as the incoming field.

First, to examine the modal situations in this waveguide, a SAFARI run is performed. A point explosive source of 250Hz is placed at 2m beneath the vacuum/water interface and receiver is placed at 5m deep. The point source excites the whole wavenumber spectrum, which is filtered by the waveguide. Those waves which satisfy modal conditions remain strong at the receiver. The wavenumber spectrum at the receiver depth is shown is Fig. (6-14). In our calculation below, we have a plane wave incident whose direction of propagation only excites the 5th mode ($k_x = 0.67m^{-1}$) as the zeroth order field. The quantities calculated are normalized such that the pressure field in the water column generated by the plane wave has amplitude of 1 (0dB).

To understand the effects of the waveguide on scattering and reverberation, it is illustrative to examine the cases both with and without the upper boundary. Next, we calculate the scattered pressure field when the upper boundary is absent, i.e., the environment with just two half spaces: the water and elastic bottom. The scattered pressure field at the horizontal plane 14m above the water/bottom interface is shown in Fig. (6-15). Notice the scattered pattern is different from that from the same patch (Fig.6-6) in the deep water case. The incoming field was a beam back then, but here we use an incident plane wave. More importantly, the grazing angles are quite different. In the last section, 6^0 grazing angle was used. Here it is 48^0. This difference shows how important the inherently three-dimensional effect is.

Now, we examine the waveguide effect. Fig. 6-16 shows the scattered pressure field 14m above the bottom in the 20m deep waveguide. The modal propagation is clearly visible. To check which modes are present in the scattered field, a close-

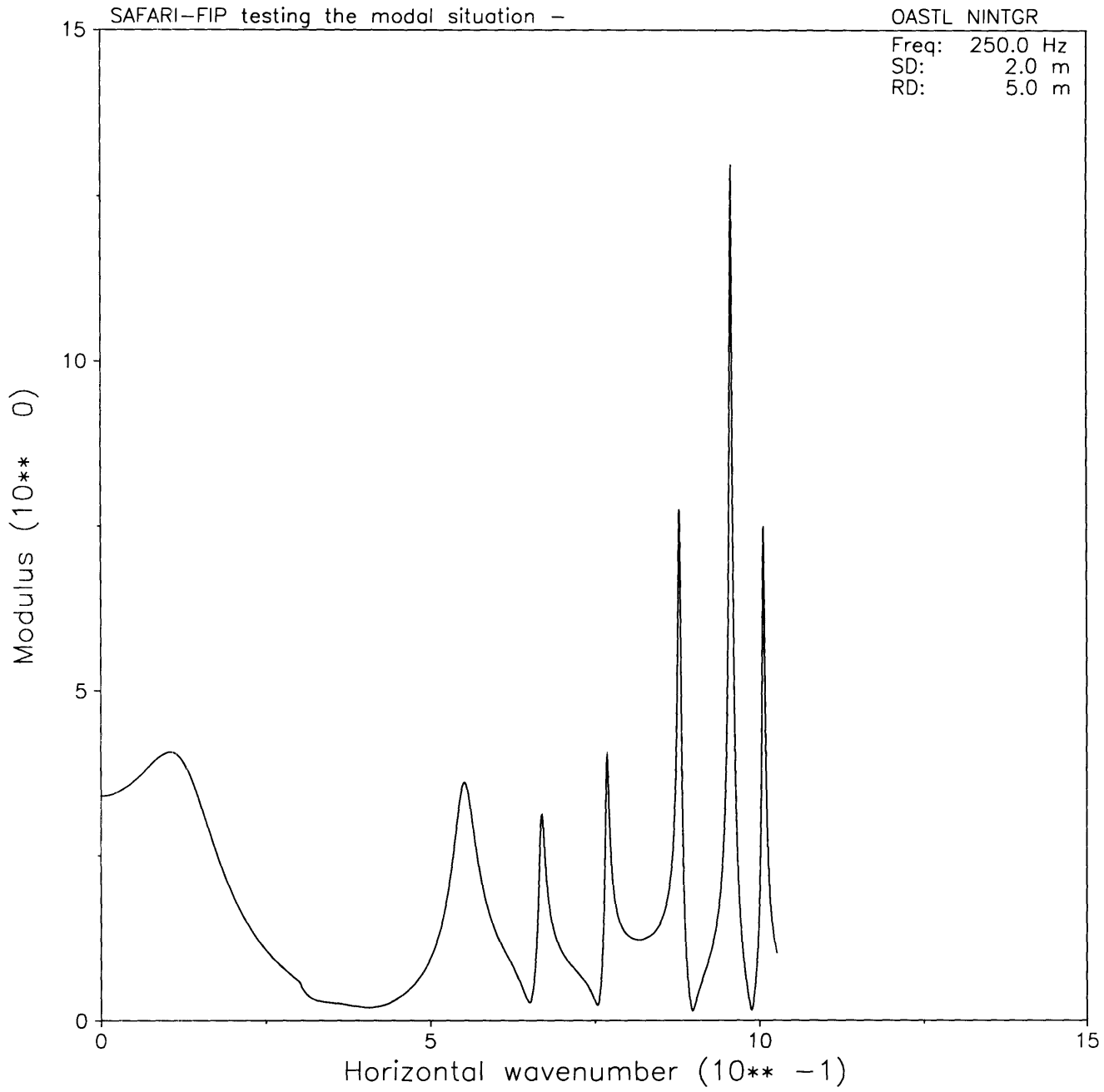

Figure 6-14: The Wavenumber Spectrum at 5m below the Free Surface in the 20m deep Waveguide, calculated by SAFARI. Generated by a 250Hz point source 2m below the free surface. Basalt Bottom.

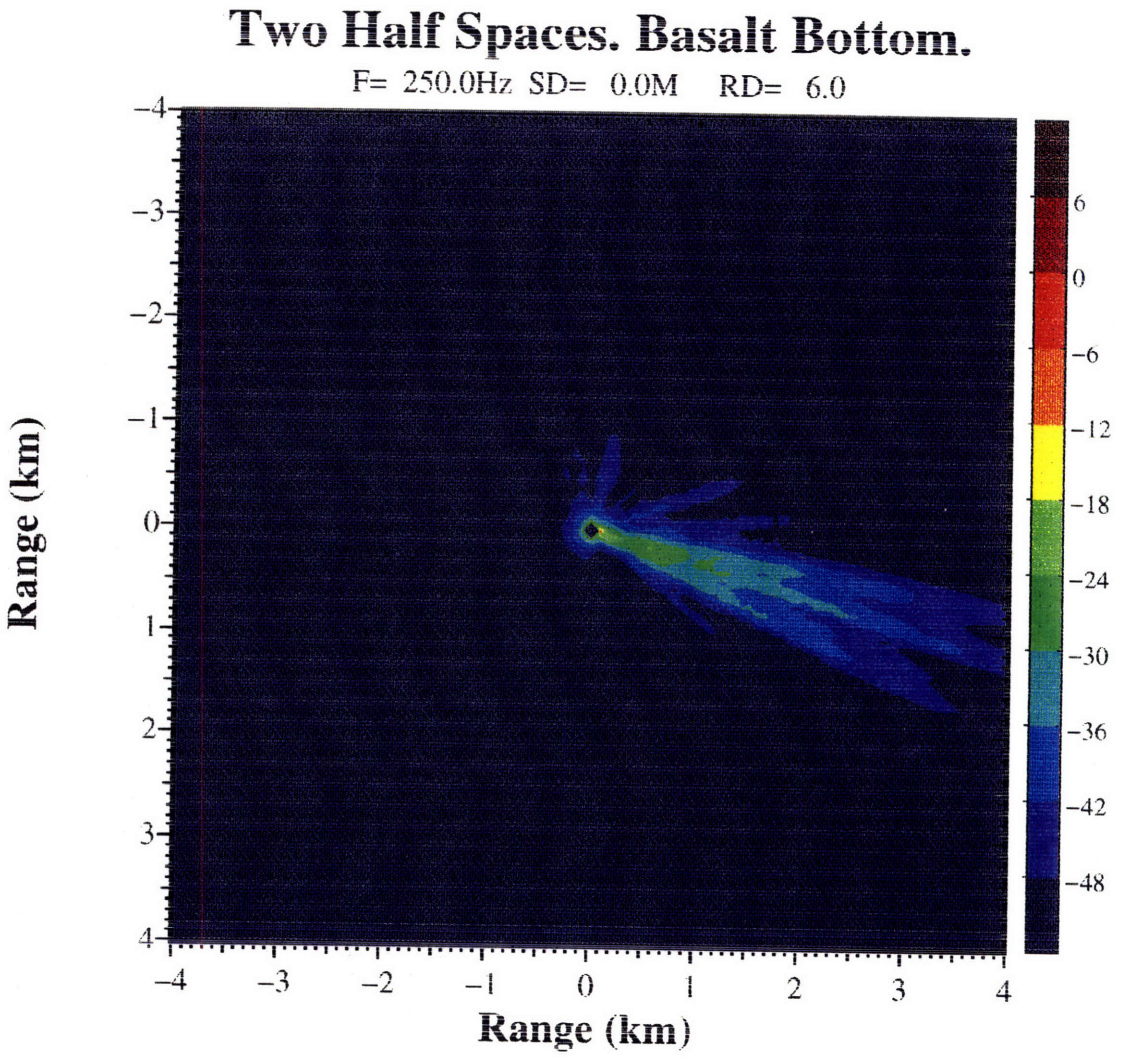

Figure 6-15: The Scattered Pressure Field in the Horizontal Plane 14m above the Bottom. Plane Wave Incidence on patch B1

up picture of the same field is shown in Fig. (6-17). It can be seen that the radial period of the strong scattering region is approximately 60m. But from Fig. (6-14) we know that the horizontal wavenumber of the 5th mode in this waveguide is 0.67 m^{-1}, which gives the radial wavelength at approximately 10m. So the 5th mode alone could not generate the propagation pattern observed - actually no single mode alone can generate this pattern. Checking Fig. (6-14) again, it is noticed that half the difference of wavenumbers between the 5th mode and mode 3 is roughly 0.1 m^{-1}. Thus the interference between these two modes can generate a pattern with radial period of around 60m.

So, we have one mode coming in; and at least one other mode scattered out. The rough patch converts part of the energy from the one incident mode to other modes. Actually, the rough patch scatters the incoming two wavenumber vectors into a whole array of wavenumber vectors which fill the three dimensional space (not uniformly, of course). Among these wavenumber vectors, only those satisfy the modal conditions for this particular waveguide survive. Specifically, each mode has a fixed k_z, so all the possible directions of that mode forms a cone with the vertical axis. Higher order modes have larger k_z, thus the corresponding cones span a narrower angle. There are six modes in our waveguide, so only those scattered wavenumber vectors that fall into one of these six cone surfaces will not be filtered out during propagation.

Now we have illustrated that the rough surface scattering in shallow water is an integral problem involving the waveguide propagation, scattering mechanism and three dimensional effect, and that our approach can treat this problem elegantly.

Next, we examine whether elasticity is important here. We rerun the same scenario as above, except using a fluid bottom. The scattered pressure fields are shown in Fig. (6-18) and Fig. (6-19) with the bottom sound speed being 5200m/s (same as the compressional sound speed of the old elastic bottom) and 2500m/s (the old shear speed) respectively.

It can be seen that neither of the two scattered fields in the fluid bottom cases portray the right level, or even the pattern of the original elastic bottom case. So we conclude that the elasticity is important in the rough surface scattering in shallow

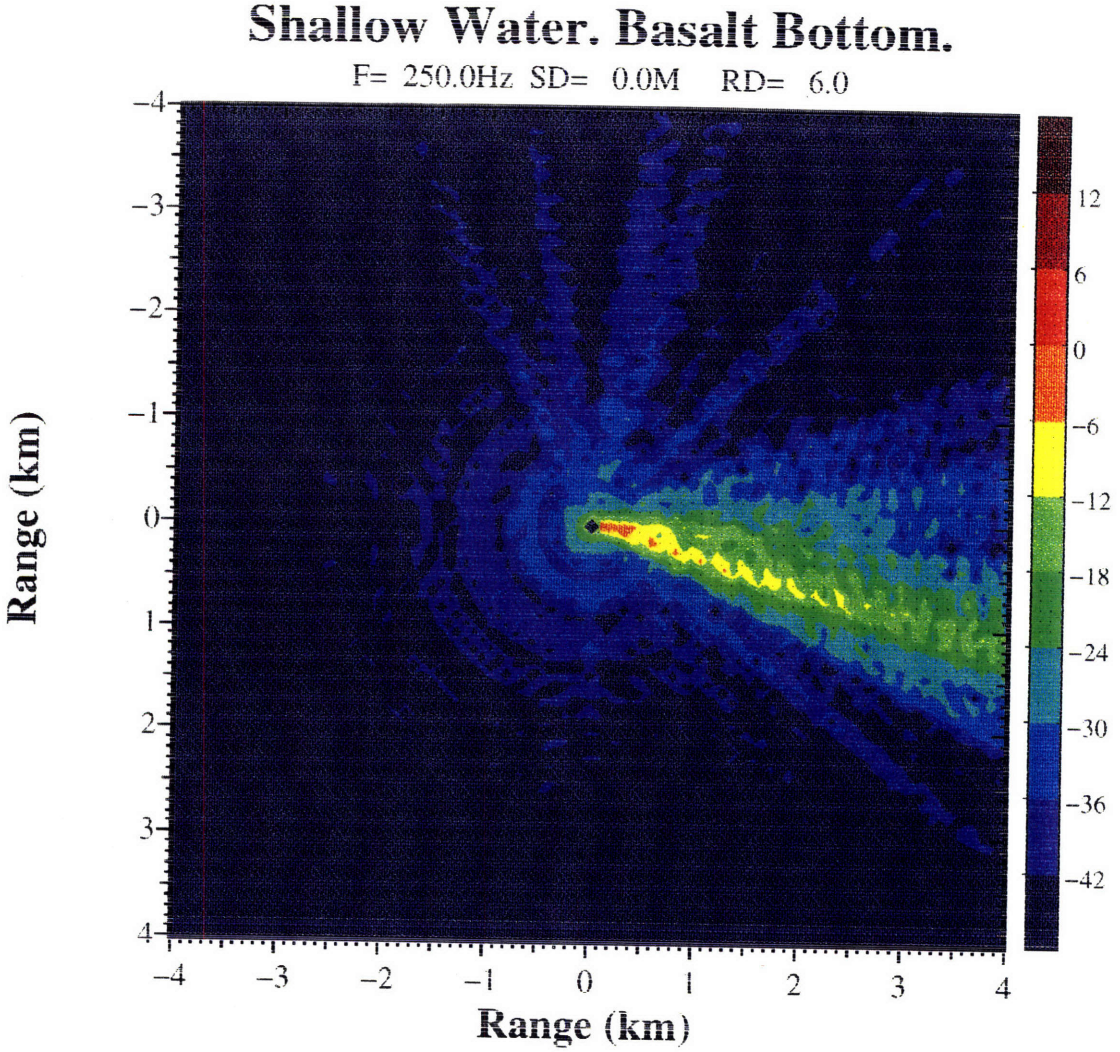

Figure 6-16: The Scattered Pressure Field in the Horizontal Plane 14m above the Bottom in a 20m Deep Waveguide. Zeroth order field has only the 5th mode. The rough patch is B1

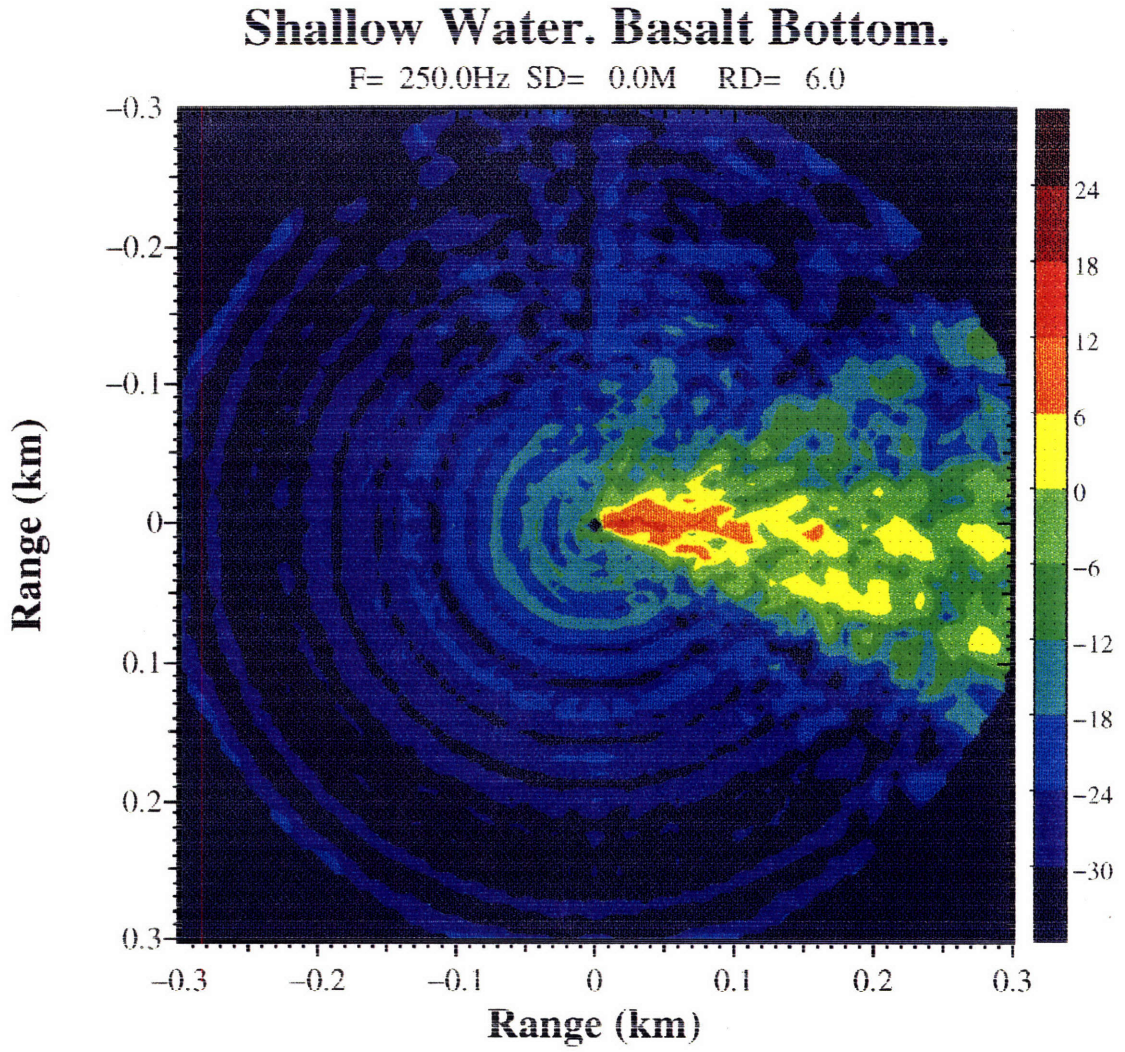

Figure 6-17: The Scattered Pressure Field in the Horizontal Plane 14m above the Bottom in a 20m Deep Waveguide. The Zoomed-In Version. Zeroth order field has only the 5th mode. The rough patch is B1.

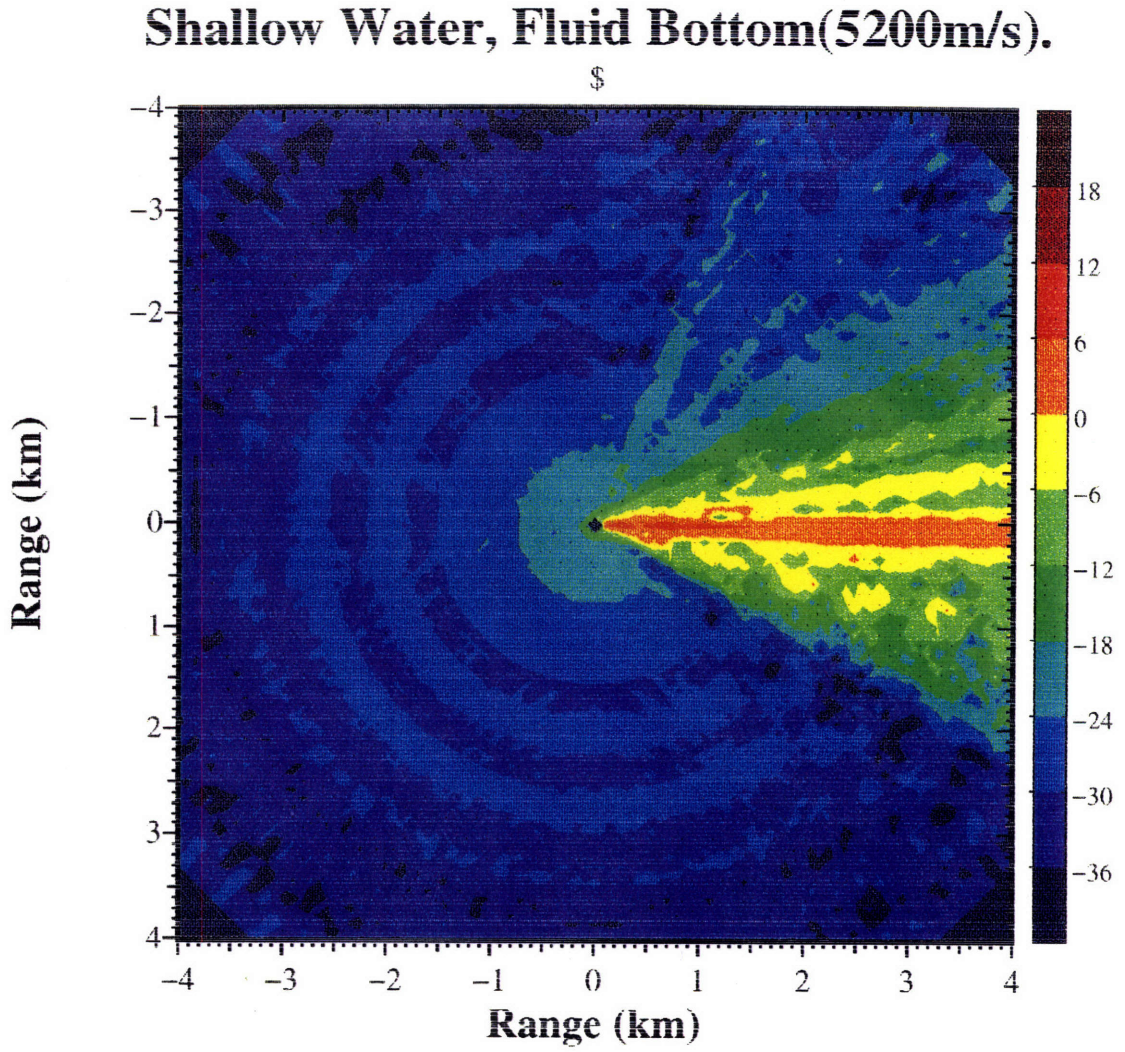

Figure 6-18: The Scattered Pressure Field in the Horizontal Plane 14m above the Bottom in a 20m Deep Waveguide. Plane Wave Insonification (kx=0.67 m^{-1}, ky=0). Fluid Bottom with Cp=5200m/s. Patch B1

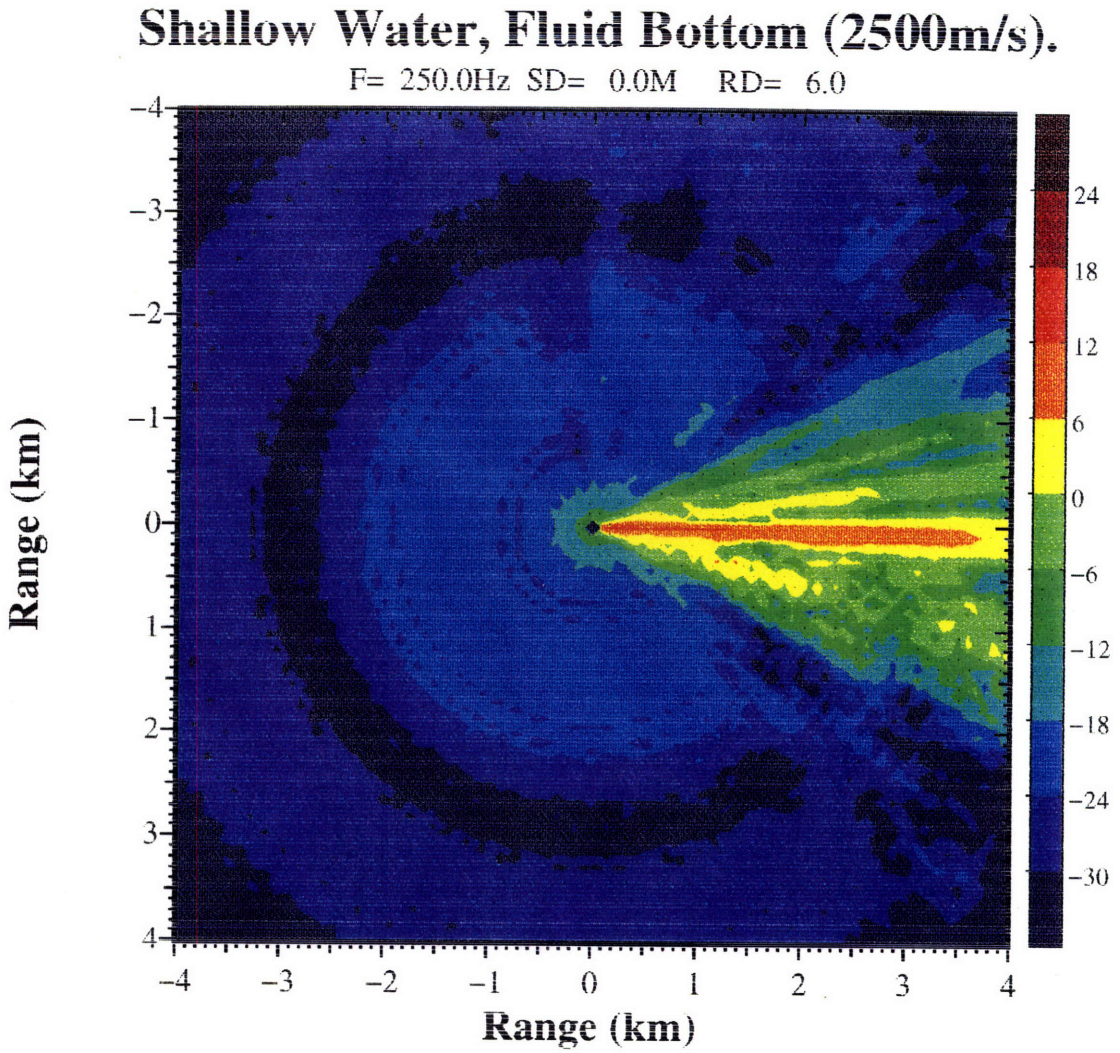

Figure 6-19: The Scattered Pressure Field in the Horizontal Plane 14m above the Bottom in a 20m Deep Waveguide. Plane Wave Insonification (kx=0.67 m^{-1}, ky=0). Fluid Bottom with Cp=2500m/s. Patch B1

water environment.

Now, we reduce the sound speed of the fluid bottom to 1600m/s. Again, using plane wave incidence ($k_x = 0.67m^{-1}$), the scattered pressure field 14m above the bottom is calculated and shown in Fig. (6-20). Let's investigate the modes closely. Of course, with different bottom, the wavenumbers of the modes will be different from those in the elastic case. We used SAFARI to calculate the wavenumber spectrum received at 15m above the bottom generated by a point source at 18m above the bottom (Fig. 6-21). Again, six modes exist in this waveguide, but at different location in the wavenumber domain. The incident plane wave lies between the 5th and 6th modes. No modes would be excited if all boundaries were smooth. But Fig. (6-20) clearly shows modal propagation, especially in the far field. The radial period of the interference pattern is approximately 600m. Going back to the SAFARI result, we see that no mode alone can generate this pattern. Actually, the wavenumber of the bottom is 0.982 m^{-1}. So all the modes except 1st and 2nd are leaky modes, which will lose energy due to penetration into the bottom. So only the first two modes can contribute to the far field. The wavenumber difference of the two modes is around 0.02 m^{-1}, and the envelope of the interference of them gives exactly the radial period of 600m. Thus the rough patch converts energy and excites the modes far away in the wavenumber domain as well as the neighboring modes.

In the previous examples we considered the waveguide with basalt bottom. It was for the illustrative purpose and to compare with the deep water scenario. This is another example of the "controlled experiment" function of models. The factor we want to examine is the waveguide effect, so we keep bottom property the same and single out the waveguide factor, which could not be done in real experiment.

Typical shallow water seabed is covered by silt. Now we calculate the rough patch scattering for a more realistic shallow water scenario: Same 20m deep waveguide and same plane wave insonification, but with silt bottom (Cp=1600 m/s, Cs=400 m/s, d= 1.8 g/cm**3, compressional attenuation = 0.2dB/wavelength, shear attenuation = 0.5dB/wavelength). The scattered pressure field 14m above the bottom is shown in Fig. 6-22. It can be seen that the level of the scattered field is much lower than

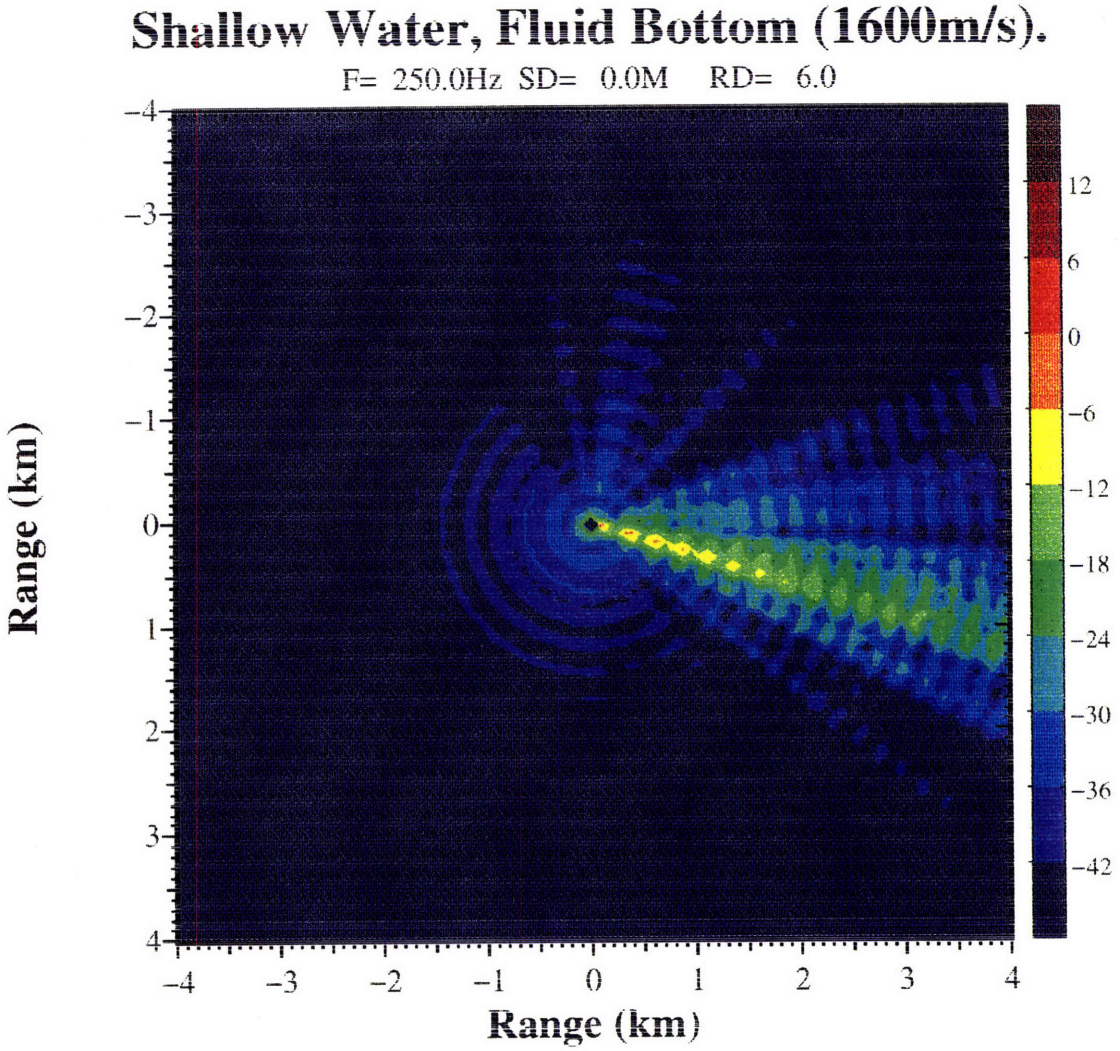

Figure 6-20: The Scattered Pressure Field in the Horizontal Plane 14m above the Bottom in a 20m Deep Waveguide. Plane Wave Insonification (kx=0.67 m^{-1}, ky=0). Fluid Bottom with Cp=1600m/s. Patch B1

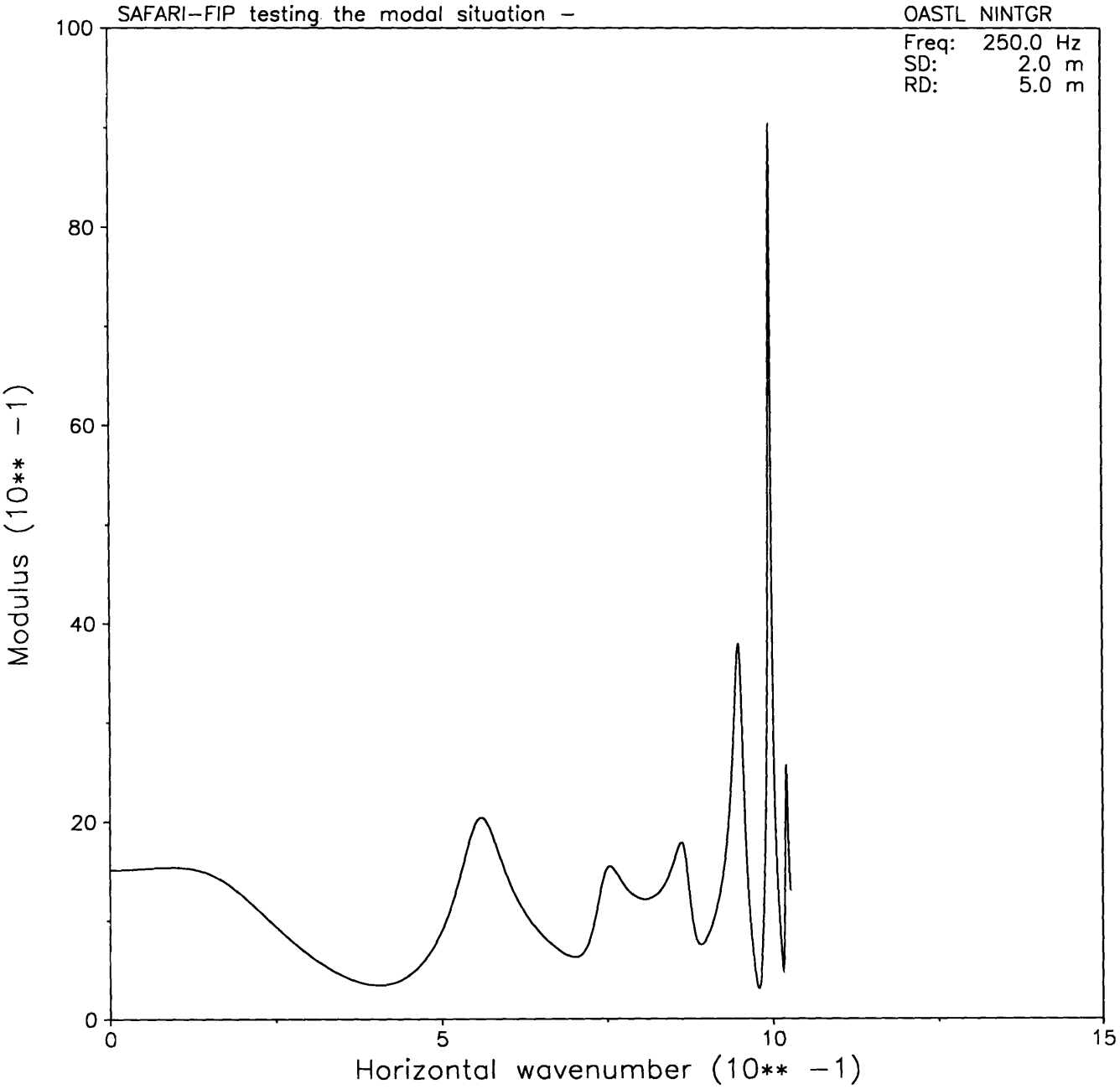

Figure 6-21: The Wavenumber Spectrum 5m below the Free Surface Calculated by SAFARI. Generated by a Point Source 2m below the Free Surface. The Waveguide is 20m Deep with Fluid Bottom, where Sound Speed is 1600m/s

that in the basalt bottom case. The reason is that we have a slow shear wave in the bottom ($400m/s < 1530m/s$). So for all the modes some energy will leak into the bottom as they propagate.

6.4 About Lambert's Law

As mentioned in Chapter Two, Lambert's law is a simple classical model of rough surface scattering. It proposes that the scattered sound intensity is proportional to the sine of the angle of scattering:

$$I_s = \mu I_i \sin\theta \sin\phi dA. \tag{6.13}$$

Traditionally, Lambert's law has been used in the monostatic sense, i.e., for the backscattering direction. However, because of the way it is formulated, it is tempting to use the Lambert's law in the bistatic sense, too. Indeed, there are discussions in the academic community to apply it in the bistatic scenario.

In this section, we shall investigate the validity of the Lambert's law in the bistatic sense. We shall consider a fixed incoming wave and consider the scattering in various direction (ϕ).

The Lambert's law as we cited in the above equation is for 2-D environment. Many real scattering problems will be in 3-D scenario. We shall extend the above equation into 3-D case.

First, we establish the spherical coordinate system as shown in Fig. 6-23. The direction of propagation is determined by vertical angle α and azimuthal angle β. The basic assumption in Lambert's law is that the scattered sound intensity is proportional the the sine of the grazing angle, i.e., the cosine of angle α. The most straight forward extension into 3-D is to assume that this is the only directional dependence of the scattering intensity. Under this assumption, the azimuthal angle does not matter and the scattering pattern will be rotational symmetric around the vertical axis.

$$I_s(\alpha, \beta) = C \cos\alpha, \tag{6.14}$$

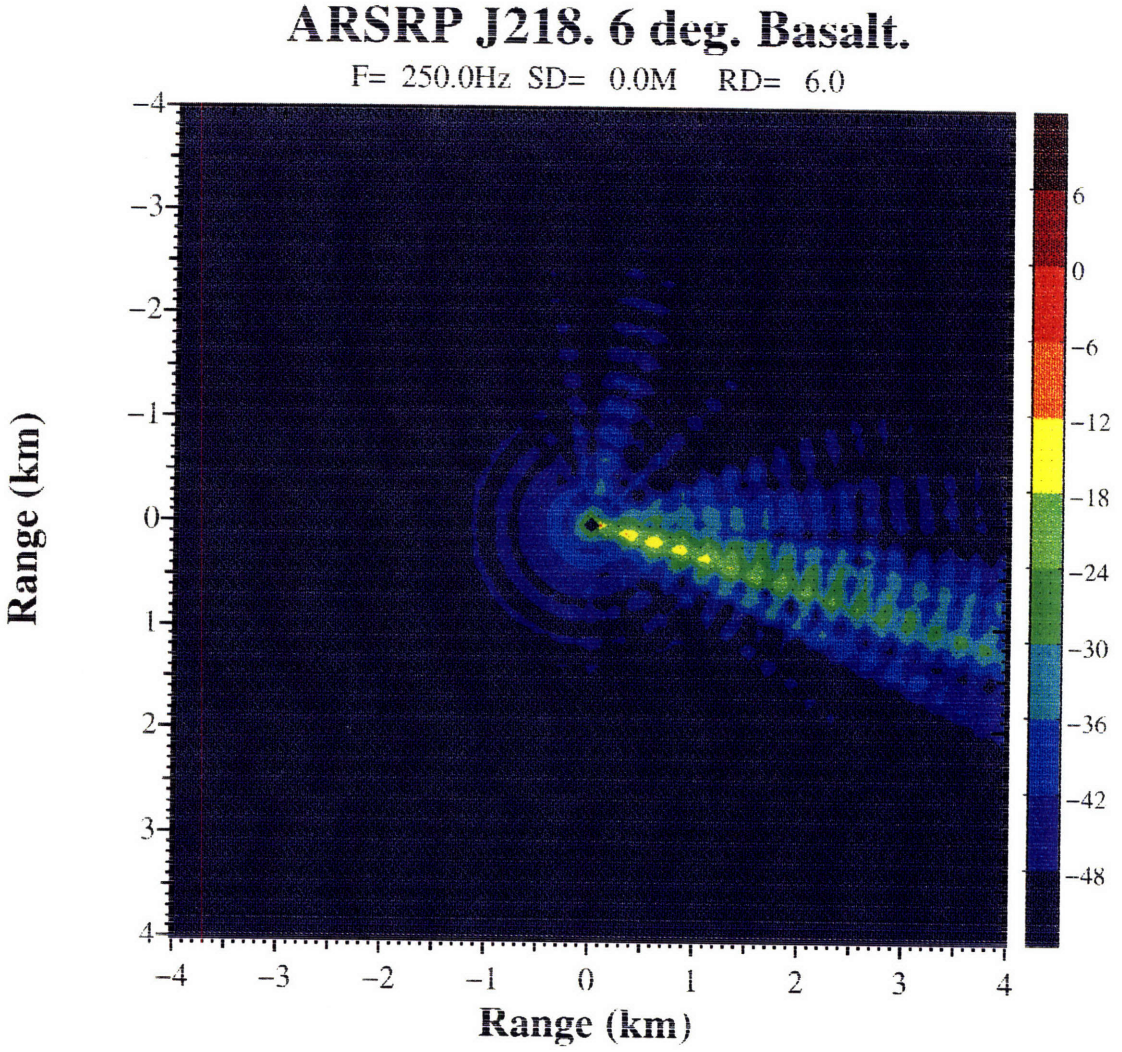

Figure 6-22: The Scattered Pressure Field in the Horizontal Plane 14m above the Bottom in a 20m Deep Waveguide. Plane Wave Insonification (kx=0.67 m^{-1}, ky=0). Silt Bottom with Cp=1600m/s, Cs=400m/s. The First Anisotropic Rough Patch Realization

where C is a constant independent of α and β.

Now, let us run a series of simulations use our model to investigate the validity of this assumption.

6.4.1 Roughness Statistics

Since we are only interested in the scattering pattern, wave guides effects are not of our concern. Here we will choose environment with two half spaces. Our first example concerns the water/basalt environment with patch B1 (with correlation lengths of 5m and 20m along the minor and major axes), with 6^0 grazing beam incidence. The angular spectrum at $150m$ above the bottom is shown in Fig. 6-24.

The figure plots the scattered sound intensity as a function of its direction of propagation. It can be seen as the half-sphere in Fig. 6-23 folded out, looking down at the patch. The radial distance from the center corresponds to vertical angle α; the azimuthal corresponds to angle β.

It is obvious from Fig. 6-24 that the scattered sound intensity is not rotational symmetric. And the maximum strength is not at the vertical direction, but approximately at 50^0 vertical angle and 20^0 azimuth from the forward scattering direction. None of these two features can be explained by Lambert's law.

To make sure this pattern is not a small probability event. We run 16 realizations with the same patch statistics and average the angular spectrum. The result is shown in Fig. 6-25.

Again, we can see the same features:

- it is not rotational symmetric.
- the maximum scattering does not occur at the vertical direction.

This deviation from Lambert's law is not caused by anisotropy. In Fig. 6-26 the averaged scattering angular spectrum over 16 realizations of statistics A (isotropic, correlation length 15m) is shown. The aforementioned two features are still present.

Now we concluded that patches with statistics A and B does not scatter sounds according to Lambert's law. Naturally, the next question is: if the roughness statistics

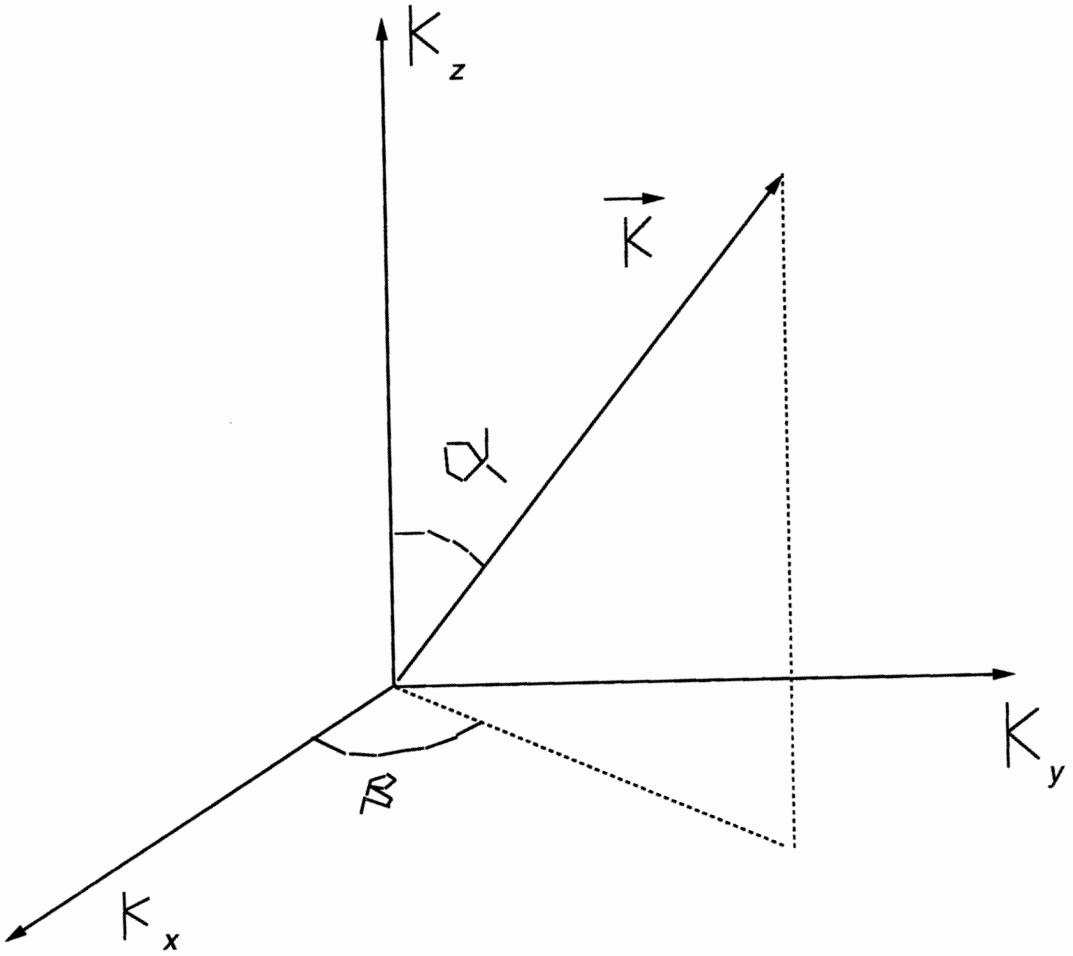

Figure 6-23: The 3-D coordinate system for Lambert's law

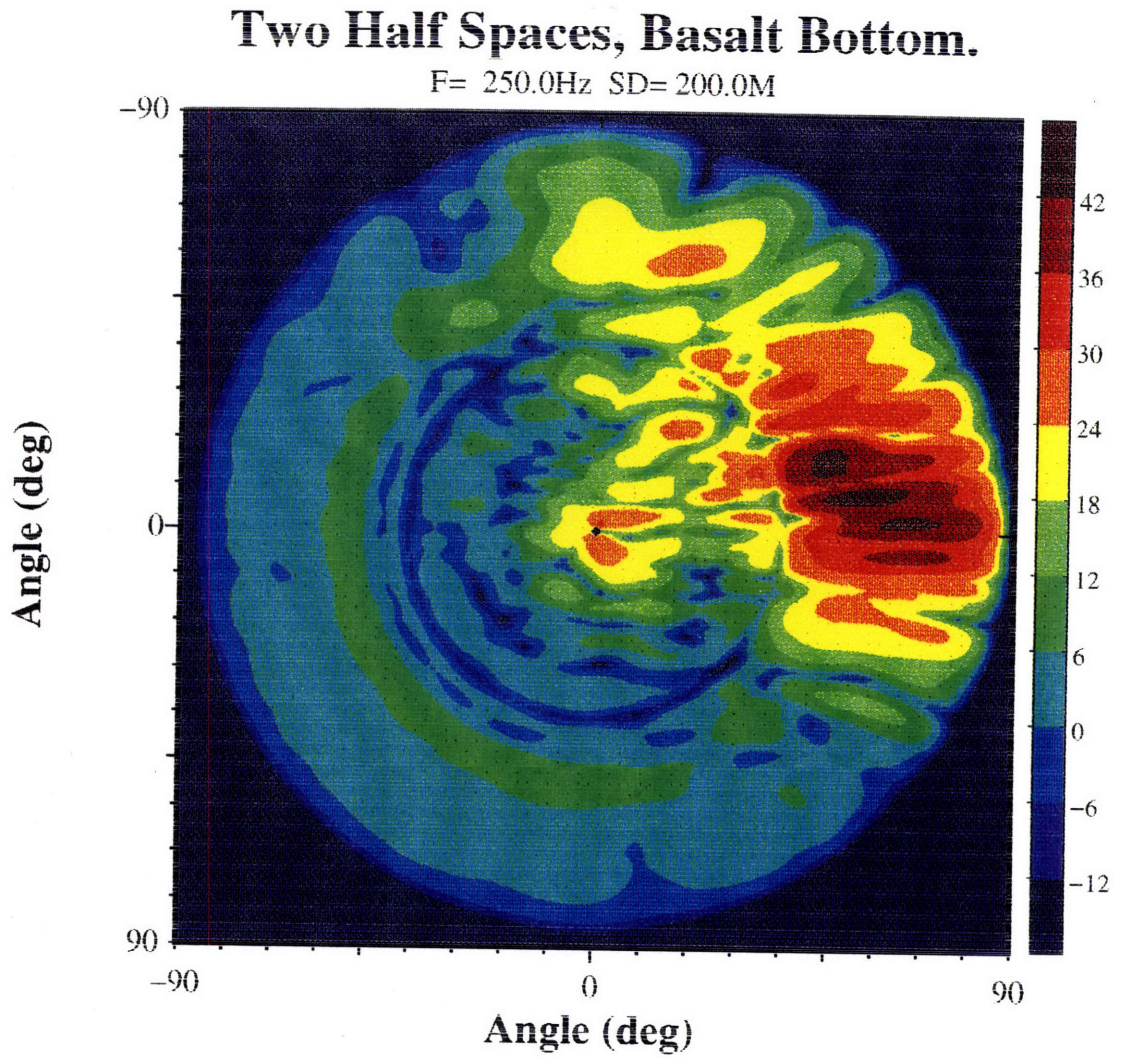

Figure 6-24: The scattering angular spectrum from patch B1 with 6 degree grazing beam insonification. The environment is water half space over basalt bottom.

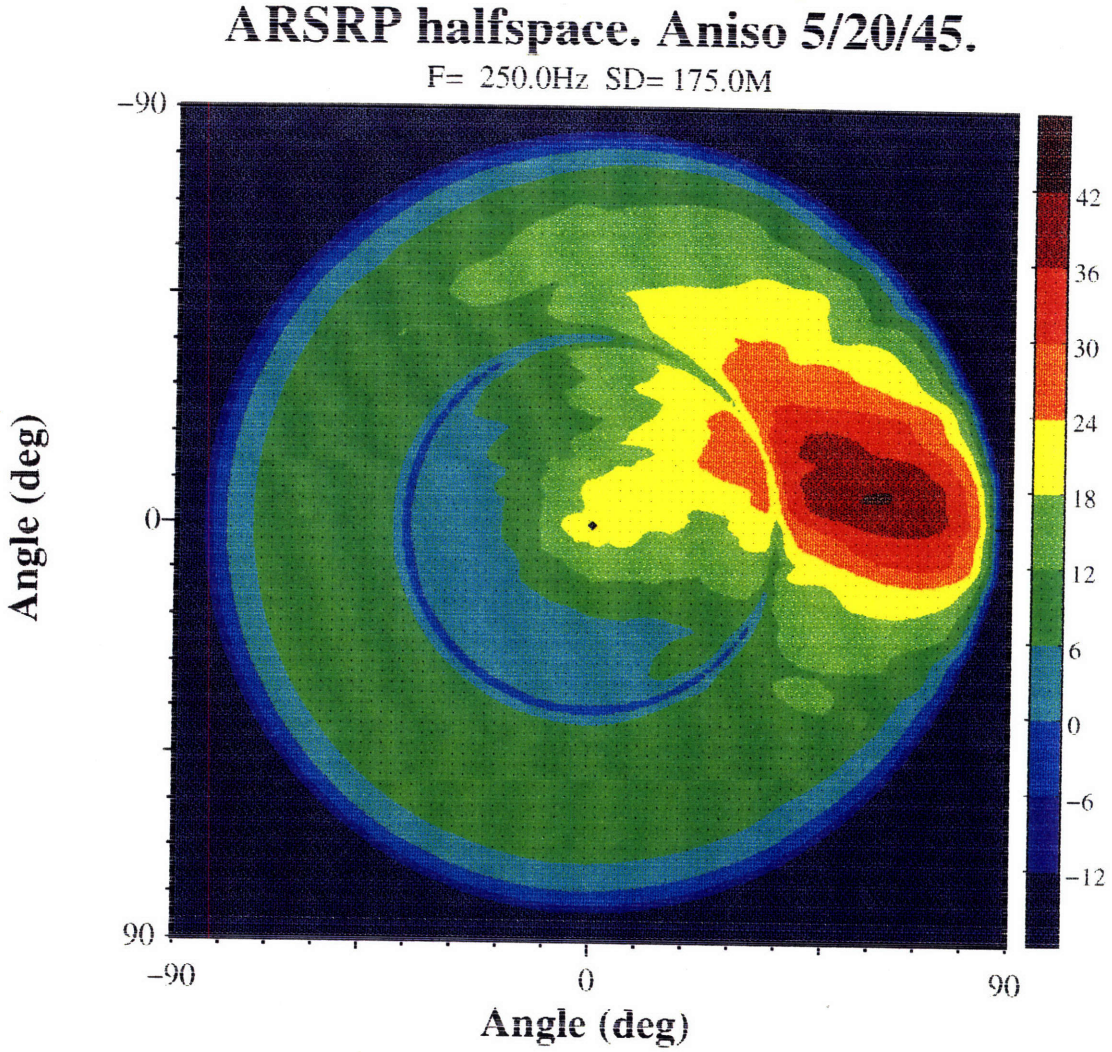

Figure 6-25: The averaged scattering angular spectrum for 16 realizations of patch roughness spectrum B, with 6 degree grazing beam insonification. The environment is water half space over basalt bottom.

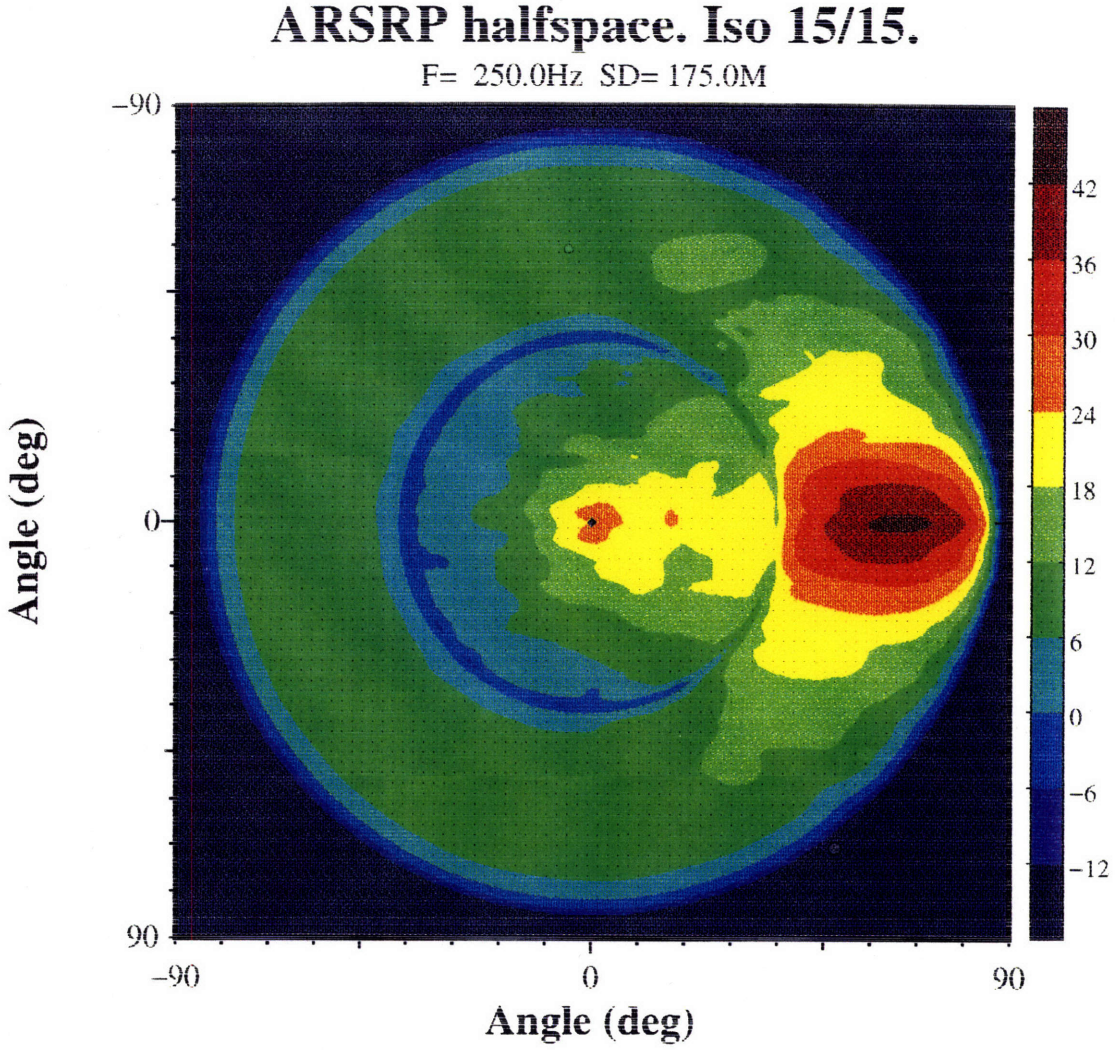

Figure 6-26: The averaged scattering angular spectrum for 16 realizations of patch roughness spectrum A, with 6 degree grazing beam insonification. The environment is water half space over basalt bottom.

or the bottom property is changed, will the scattering pattern become closer to the Lambert's law behavior?

Up to this point, our definition of Lambert's law behavior has been characterized by two features of the scattering intensity: the rotational symmetry and the cosine of vertical angle dependence. These two features might not change in the same way as patch changes. For example, as we change the patch, we might get a more symmetric scattering but the scattering deviates further from $\cos\alpha$ dependence. Of the two characteristics, $\cos\alpha$ dependence is more essential to Lambert's law assumption. We can relax the azimuthal symmetry and allow the coefficient C in Eq. (6.14) to be a function of azimuthal angle β. Thus, from now on, we speak of "more Lambertian" or "less Lambertian" scattering in reference to how close the scattering intensity changes proportional to $\cos\alpha$, regardless of azimuthal dependence.

First, we would like to examine the effect of changing the rough statistics of the patch. We keep all the parameters in statistics B, only change the correlation lengths proportionally: from $5m/20m$ on minor/major axis (statistics B) to $20m/80m$ (statistics D) and $1m/4m$ (statistics E).

The scattering angular spectra for D and E realizations are shown in Fig. 6-27 and Fig. 6-28 respectively. Comparing these two figures with Fig. 6-24, it can be seen that the rougher the patch is (shorter correlation length), the stronger the scattering close to vertical direction. So we can say loosely that rougher patches are more Lambertian. However, in all three scenarios, the maximum is at the direction far from vertical. To find out whether the maximum will move to the vertical for extremely rough patch is beyond the capability of our model. One of the basic restrictions of perturbation method is that the gradient of the roughness be much smaller than one. To have extremely short correlation length, the gradient of roughness can be very large, which caused that higher order terms in the expansion not being neglicable.

6.4.2 Bottom Properties

Next, let us examine the effect of changing the bottom material. The scattering angular spectra from fluid patches with sound speed of $5200m/s$ and $2500m/s$ are

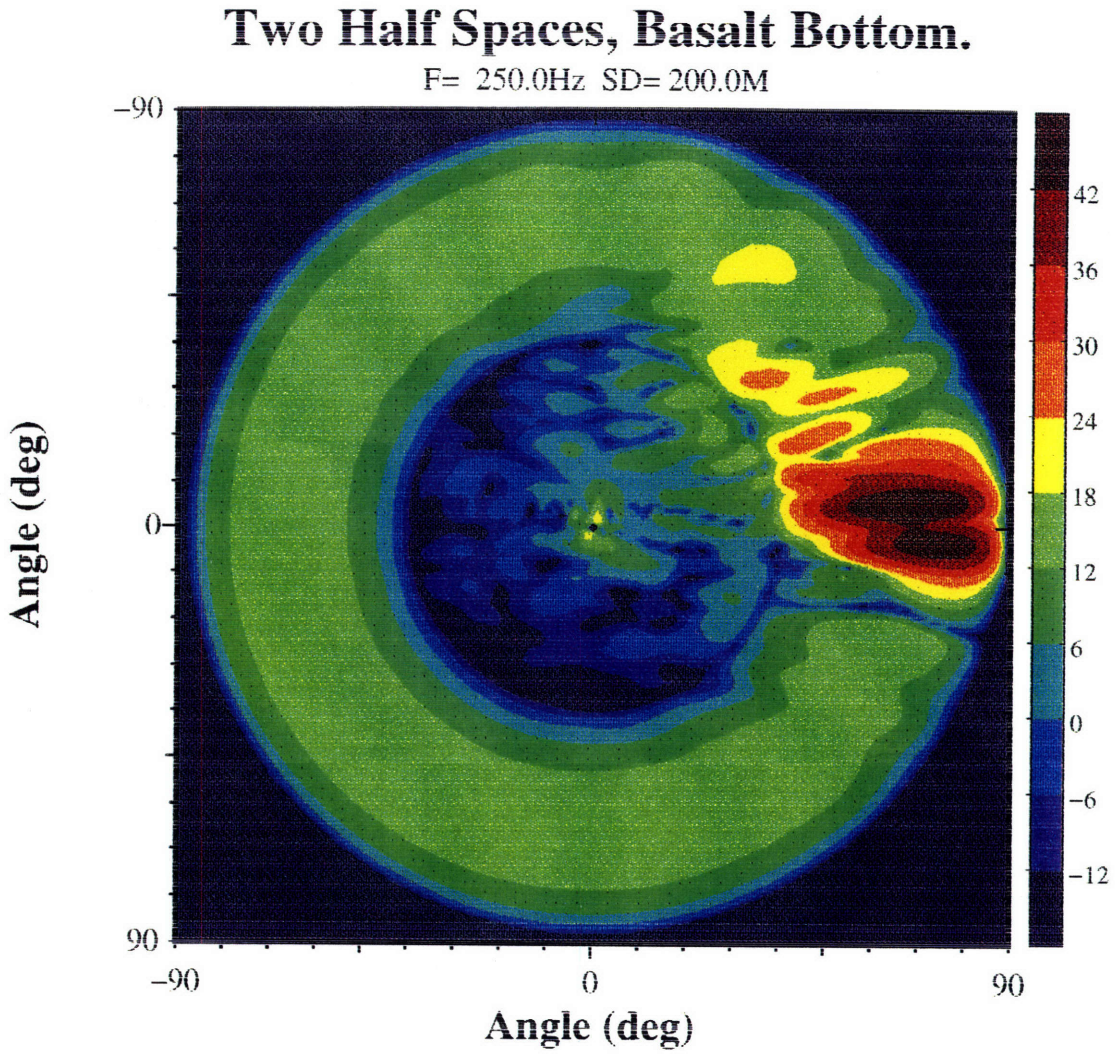

Figure 6-27: The scattering angular spectrum from patch D1 with 6 degree grazing beam insonification. The environment is water half space over basalt bottom.

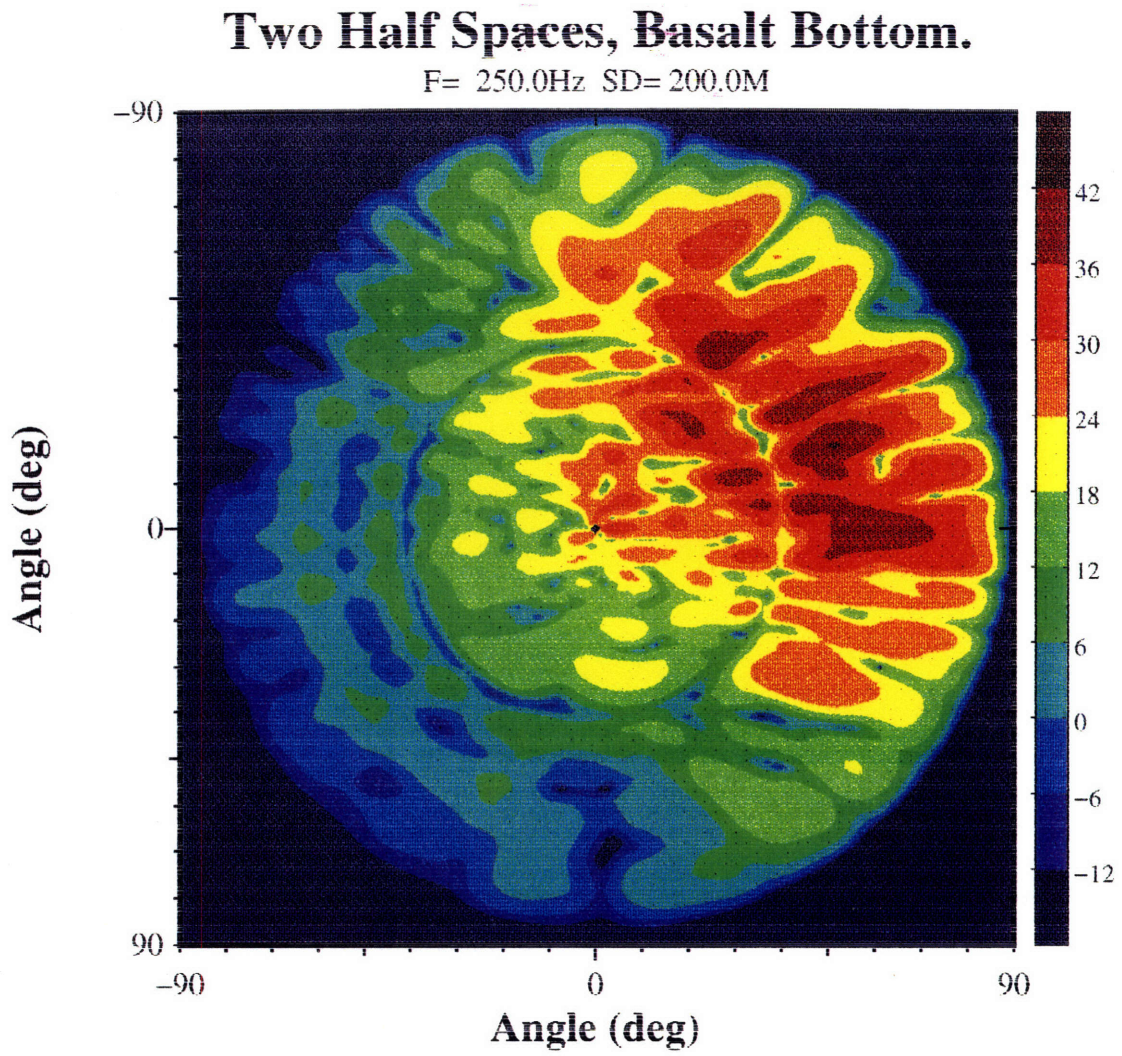

Figure 6-28: The scattering angular spectrum from patch E1 with 6 degree grazing beam insonification. The environment is water half space over basalt bottom.

shown in Fig. 6-29 and Fig. 6-30 respectively. The patch profile is assumed to be B1. There are no significant differences between these two figures and Fig. 6-24.

Thus, we conclude that the Lambert's law is not a good description of the bistatic rough surface sound scattering for the rough statistics we used here. The scattering pattern is far more sensitive to the rough statistics than to the material property of the bottom. Lambert's law is a better description for rougher surface. If we use Lambert's law in the monostatic sense, comparing our simulation with Eq. (6.13), , a coefficient μ around $-20dB$ is obtained. This is consistant with experiment observation.

So far, we have examined the effects of the roughness statistics, waveguide physics and bottom property on the rough patch scattering. In the following examples, these individual effects and their interplay are clearly shown. Fig. 6-31 shows the scattered wavenumber spectrum at $150m$ above the bottom with rough patch $C1$ with 6^0 grazing beam incidence. A ring structure is visible. The outer circle corresponds to the compressional wavenumber of the water column. The inner circle corresponds to the shear wavenumber in the bottom. Those waves having wavenumber spectrum inside the inner circle will be refracted into propagating shear waves in the bottom. These waves have grazing angle larger than the critical angle. Part of the energy is lost into the bottom. Thus in the wavenumber spectrum, we see a hole inside the inner circle. In the first quadrant of the figure, a lineated feature is visible. This corresponds to the roughness spectrum of the patch. Remember, the roughness in this patch is lineated at 45^0 between X and Y axis, so its spectrum is perpendicular to that direction. It runs through the point which corresponds to the specular reflection, i.e., the point on the positive k_y axis. This roughness spectrum, together with the ring structure, determines the scattered field.

Now, instead the half space, we consider the ARSRP waveguide. The scattered wavenumber spectrum $170m$ below the sea surface is shown in Fig. 6-32. The patch and incident beam are the same as those in the last example. Now, many circle structures emerge. These are the modes in the waveguide. These two examples showed that the wavenumber integration approach gives us a clear picture of the basic physical mechanism. By just looking at the picture, it is easy to pick up the information about

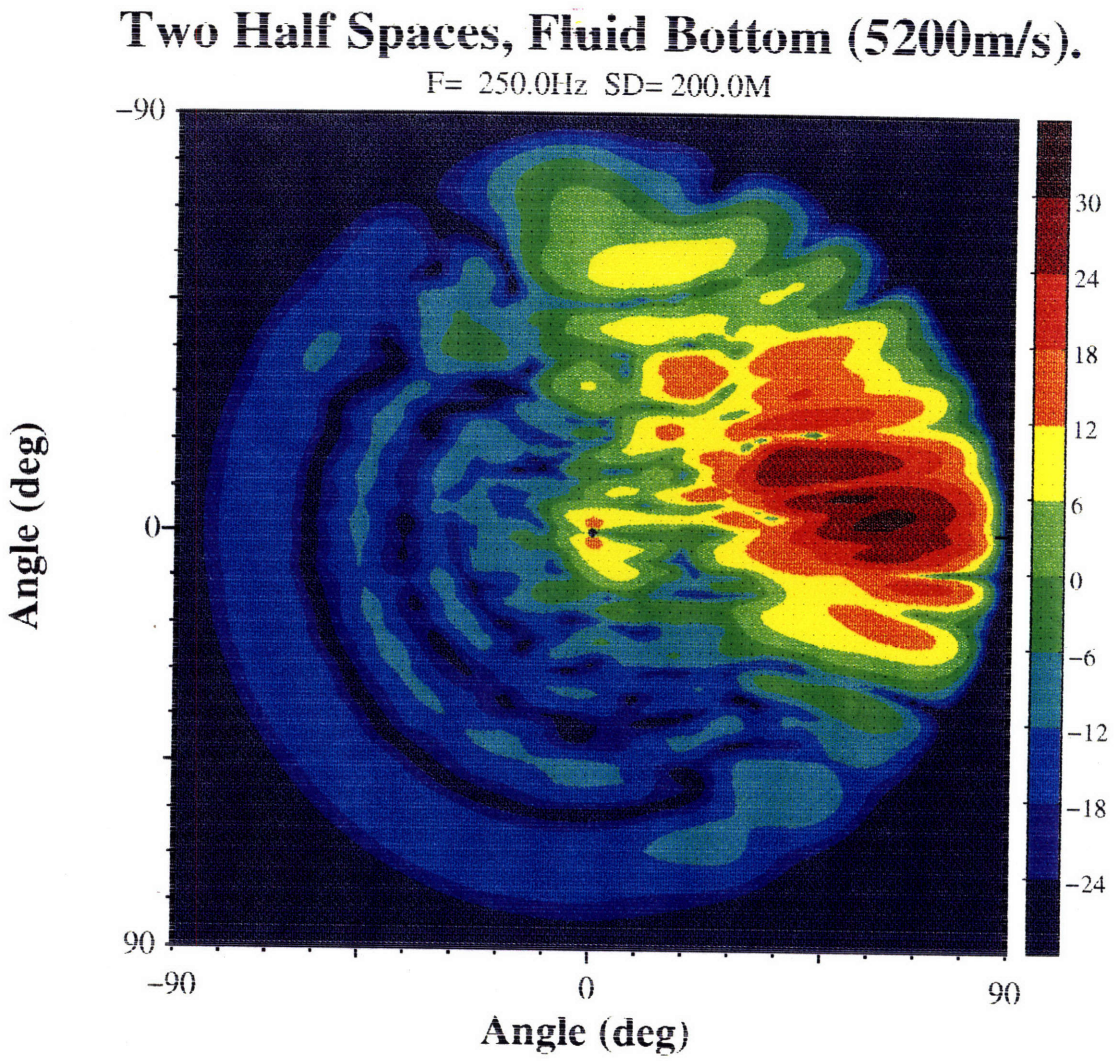

Figure 6-29: The scattering angular spectrum from patch B1 with 6 degree grazing beam insonification. The bottom is fluid with sound speed of 5200m/s.

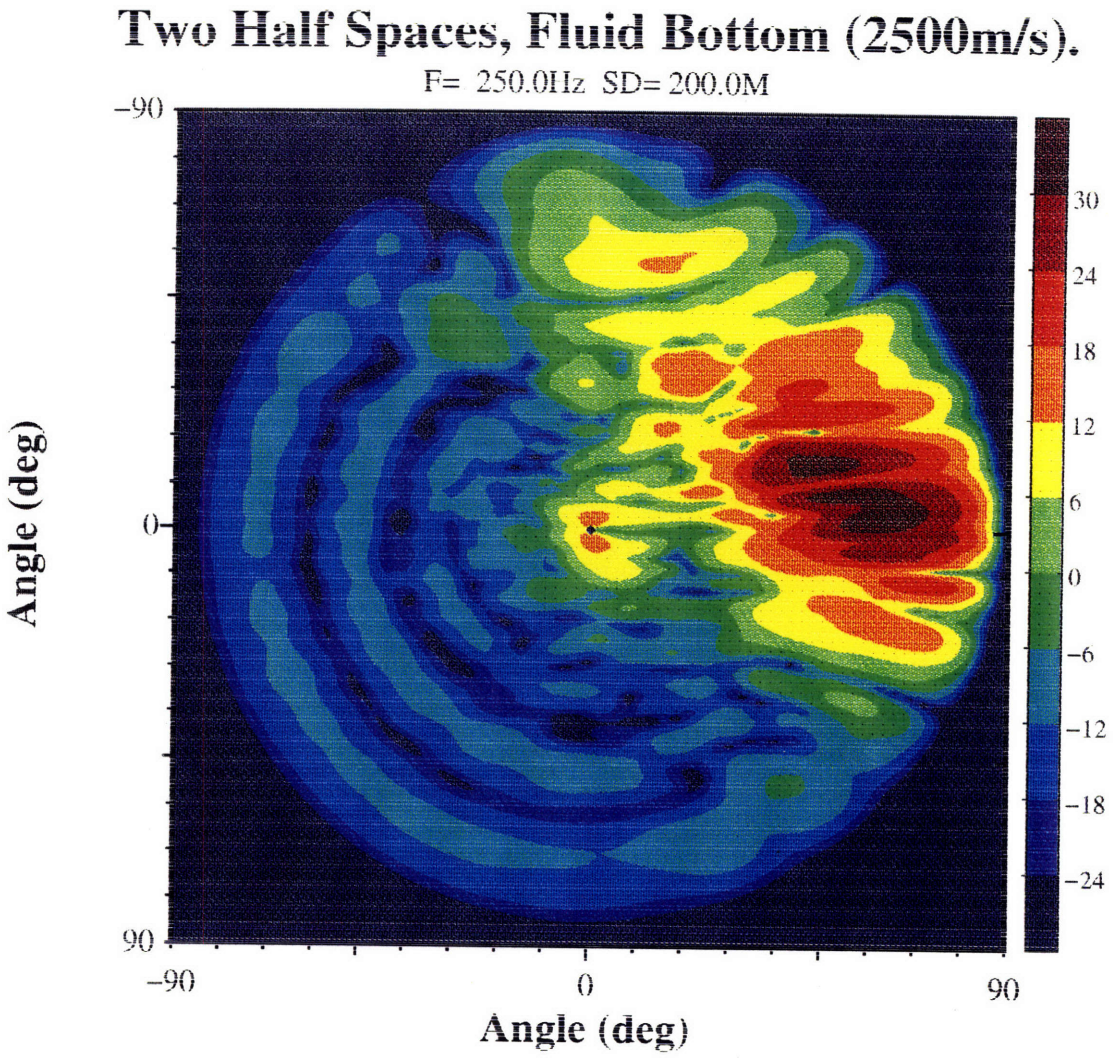

Figure 6-30: The scattering angular spectrum from patch B1 with 6 degree grazing beam insonification. The bottom is fluid with sound speed of 2500m/s.

the medium properties (the width of the ring structure), the roughness spectrum (the direction of lineation and the width of the straight band), and the waveguide height (the circle pattern).

There are discussions in the academic community as regard to whether the elasticity is important to the rough interface scattering. In the last two scenarios shown, elasticity is very important. Without the shear wave in the bottom, wavenumber spectrum of the scattered field will extend inward all the way to the circle corresponds to the compressional wavenumber of the basalt. Thus, there will be a much smaller hole in the wavenumber spectrum. As a result, more steep propagating modes will be received at the sonar array.

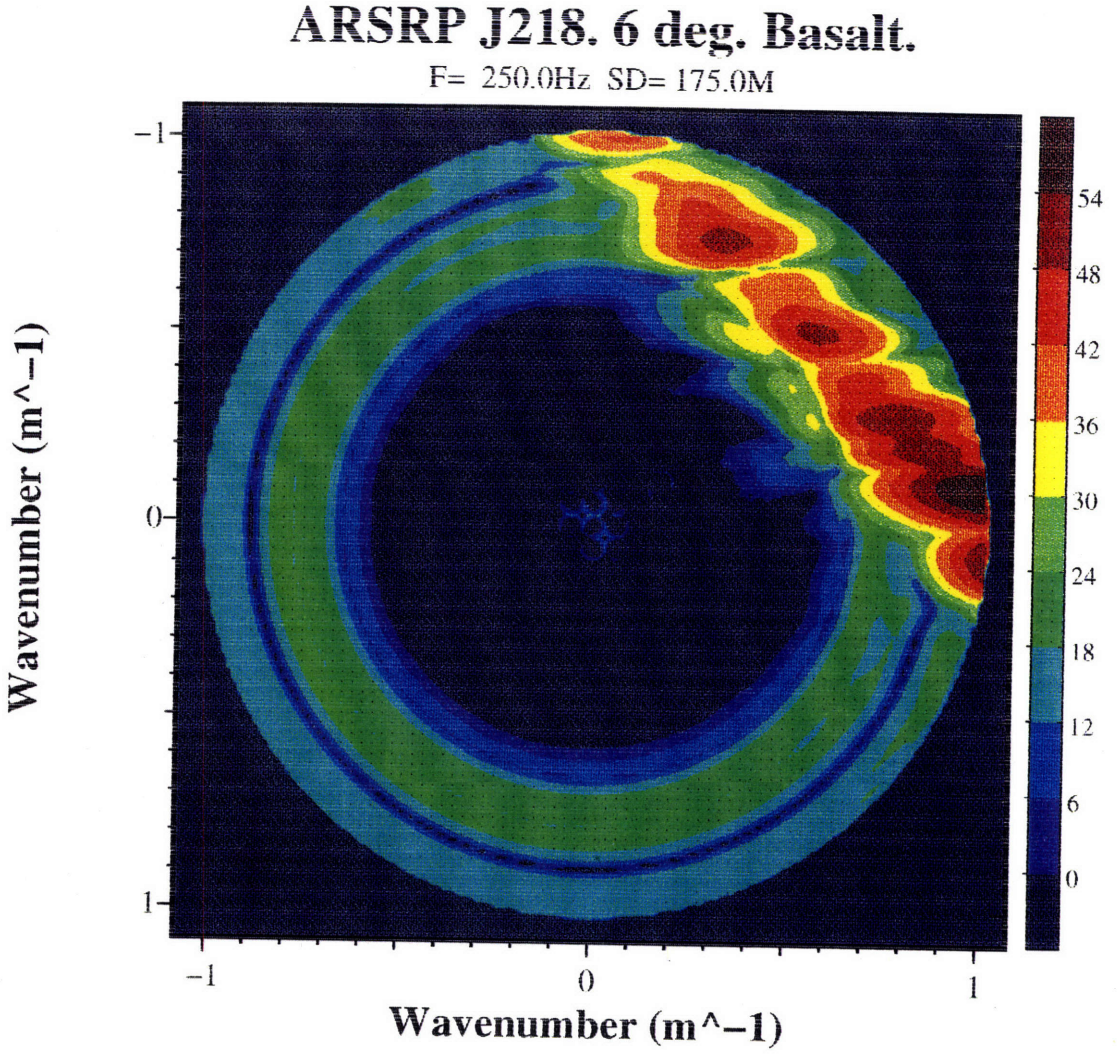

Figure 6-31: The scattered wavenumber spectrum from patch C1 with 6 degree grazing beam insonification, 150m above the bottom. Water half space overlays the basalt half space.

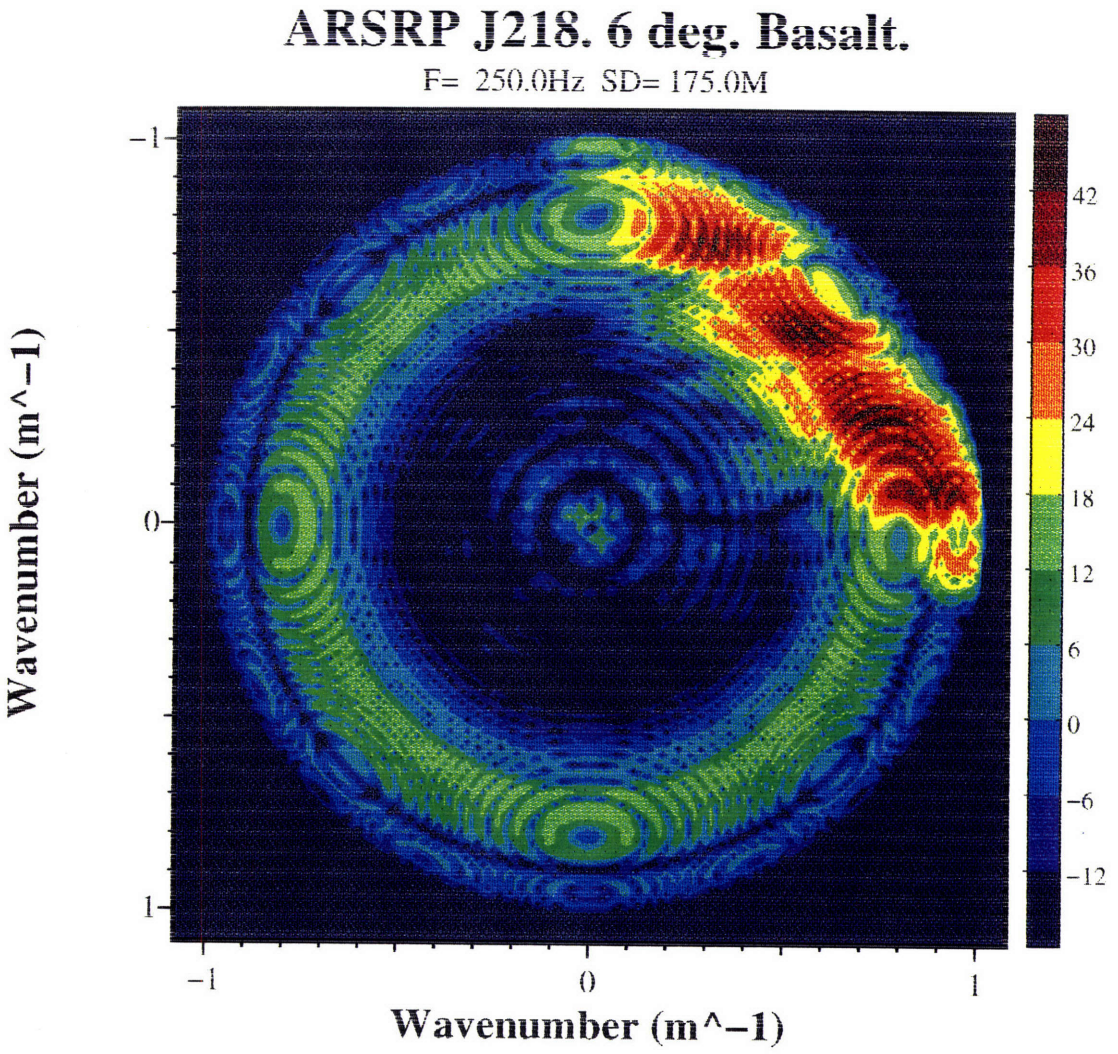

Figure 6-32: The scattered wavenumber spectrum from patch C1 with 6 degree grazing beam insonification, 170m below the sea surface. ARSRP environment.

Chapter 7

Summary

7.1 Accomplishments and Conclusions

The motivations of this thesis are the improvement of sonar array performance and seismic exploration. We set out to model the seismo-acoustic reverberation in the ocean environment. It is our hope that the model can facilitate our understanding of the underlying physics and ultimately can be incorporated in solving the inverse problem (e.g. MFP).

The accomplishments and conclusions of this study can be summarized as follows:

- A 3D Wavenumber Integration approach in Cartesian Coordinate system for arbitrary fluid/elastic stratification is developed. This is vital for the development of 2-1/2D WI-BEM modeling. It will also be very useful for the 3D WI-BEM model and for the extension of the range-dependent OASES to N by 2D scenario.

- The emphasis of the thesis has been on the combined effects of **3D**, **Elasticity**, and **Waveguide Effect** on the seismo-acoustic reverberation in the ocean environment. It is shown that all three of these factors are important in most scenarios. The traditional 2D, fluid model and separated treatment of scattering/propagation is extremely restrictive and is only applicable to a small subset of the many possible scenarios in the realistic ocean environment. Furthermore,

all these factors are different aspects of an integrated problem. This calls for unified approaches like those used in the thesis.

- Although because of their different attributes, two models are developed for facet and diffuse scattering problem. But the centerpiece is the same: **the Wavenumber Integration** approach. This is the key to the efficiency of the algorithms based on the models. Since the background ocean waveguide is horizontally stratified, the waveguide effect can be efficiently accounted for by means of the existing SAFARI code.

- Because the Wavenumber Integral approach is used, the reverberation field can be expressed in terms of different wave components, which facilitates easy physical understanding. This is even more important in 3D, elastic scenarios. Since the geometry and environment are so complicated, it is extremely difficult, if not outright impossible to conceive what's going on intuitively.

- The choice of the BEM approach in treating the facet scattering problem is another key to the numerical efficiency, since only the facet boundary need to be discretized, limiting the size of equations to be solved as compared to FEM or FD approaches. Also the radiation condition problems in FEM and FD are eliminated.

- The hybrid spatial-wavenumber domain approach used in the rough interface patch scattering modeling further increases the numerical efficiency by the direct evaluation of the source distribution in a compact spatial domain.

- Although our modeling work has been geared to somewhat special cases (2hD facet scattering instead of full 3D problem, and rough interface patch instead of infinite extended roughness), the results are very illustrative and give us some insights to the underlying physics in the ocean seismo-acoustic reverberation. For example, it is shown that both the scattering mechanism can convert energy to different wave types and different modes. These models have significant applications to realistic ocean environments. Furthermore, the approaches and

philosophies employed here can be extended to developing more generalized models.

7.2 Suggestions for Future Work

The models developed in this thesis are for somewhat special case scenarios. The logical next step will be to generalized them.

- It is desirable to develop a 3D WI-BEM facet reverberation model. The major principles and approaches are clear. But there are some issues remained to be addressed.

  a) In the 2D and 2hD WI-BEM model significant computational savings have been obtained by performing element integrations analytically in the wavenumber domain. Similar techniques must be developed in 3D.

  b) As the author has experienced throughout this study, the choice of coordinate system can be a tricky problem in 3D case. It might be necessary to use both cylindrical and Cartesian coordinates at different part of the code. (Cylindrical for propagation and Cartesian for BEM formulation). This calls for proper coordinates transforms. Some of the coordinate transform formulations derived by the author might be useful, both between cylindrical and Cartesian (Appendix B) and between cylindrical coordinates with different axis (Appendix A).

- The diffuse scattering cases treated in this thesis have been for realizations of a rough interface patch. So the results are samples from the probability space. It is desirable to obtain the mean and variance of the scattered field. An easy way to get statistical results is to perform Monto-Carlo simulations. Each one using our code on one of the realizations. This algorithm is naturally suitable to large scale parallel machines. The average scattered field was calculated this way and was shown in Chapter 6. Next step is to compute the covariance of the field.

Appendix A

3-D DGM Formulation

A.0.1 Equation of Motion

The displacement field can be described by a scalar potential and a vector potential.

$$\vec{u} = \nabla\phi(x,y,z) + \nabla \times \vec{\psi}(x,y,z) \tag{A.1}$$

We can expand the vector displacement potential $\vec{\psi}$ as following:

$$\vec{\psi}(x,y,z) = \nabla \times (0,0,\Lambda) + (0,0,\psi_z) \tag{A.2}$$

For homogeneous part of the field, the displacement potentials satisfy the Helmholtz equations:

$$\begin{cases} (\nabla^2 + K_p^2)\phi(x,y,z) = 0 \\ (\nabla^2 + K_s^2)\Lambda(x,y,z) = 0 \\ (\nabla^2 + K_s^2)\psi_z(x,y,z) = 0 \end{cases} \tag{A.3}$$

where, K_p is the compressional media wavenumber, and K_s the shear media wavenumber.

We apply the Fourier Transform:

$$\begin{cases} F(x,k_y,z) = \int_{-\infty}^{+\infty} f(x,y,z)e^{ik_y y}dy \\ f(x,y,z) = \frac{1}{2\pi}\int_{-\infty}^{+\infty} F(x,k_y,z)e^{-ik_y y}dk_y \end{cases} \tag{A.4}$$

on the Helmholtz equations to get:

$$\begin{cases} (\frac{\partial^2}{\partial x^2} + \frac{\partial^2}{\partial z^2} - (k_y^2 - k_p^2))\phi(x, k_y, z) = 0 \\ (\frac{\partial^2}{\partial x^2} + \frac{\partial^2}{\partial z^2} - (k_y^2 - k_s^2))\Lambda(x, k_y, z) = 0 \\ (\frac{\partial^2}{\partial x^2} + \frac{\partial^2}{\partial z^2} - (k_y^2 - k_s^2))\psi_z(x, k_y, z) = 0 \end{cases} \tag{A.5}$$

Similarly, apply Fourier Transform with respect to x, we get:

$$\begin{cases} (\frac{\partial^2}{\partial z^2} - \alpha^2)\phi(k_x, z; k_y) = 0 \\ (\frac{\partial^2}{\partial z^2} - \beta^2)\Lambda(k_x, z; k_y) = 0 \\ (\frac{\partial^2}{\partial z^2} - \beta^2)\psi_z(k_x, z; k_y) = 0 \end{cases} \tag{A.6}$$

where $\alpha = \sqrt{k_x^2 + k_y^2 - k_p^2}$, and $\beta = \sqrt{k_x^2 + k_y^2 - k_s^2}$.

Thus, we can solve the displacement potentials for the homogeneous field:

$$\begin{cases} \phi(k_x, z; k_y) = A^-(k_x, k_y)e^{-\alpha z} + A^+(k_x, k_y)e^{\alpha z} \\ \psi_z(k_x, z; k_y) = B^-(k_x, k_y)e^{-\beta z} + B^+(k_x, k_y)e^{\beta z} \\ \Lambda(k_x, z; k_y) = C^-(k_x, k_y)e^{-\beta z} + C^+(k_x, k_y)e^{\beta z} \end{cases} \tag{A.7}$$

A.0.2 Homogeneous Field

We have

$$\begin{aligned} \vec{u}(x, y, z) &= \nabla\phi(x, y, z) + \nabla \times (\nabla \times (0, 0, \Lambda) + (0, 0, \psi_z)) \\ &= \nabla\phi + \nabla \times (\frac{\partial}{\partial y}\Lambda, -\frac{\partial}{\partial x}\Lambda, \psi_z) \end{aligned} \tag{A.8}$$

that is,

$$\begin{cases} u(x, y, z) = \frac{\partial}{\partial x}\phi(x, y, z) + \frac{\partial}{\partial y}\psi_z(x, y, z) + \frac{\partial^2}{\partial x \partial z}\Lambda(x, y, z) \\ v(x, y, z) = \frac{\partial}{\partial y}\phi(x, y, z) - \frac{\partial}{\partial x}\psi_z(x, y, z) + \frac{\partial^2}{\partial y \partial z}\Lambda(x, y, z) \\ w(x, y, z) = \frac{\partial}{\partial z}\phi(x, y, z) - (\frac{\partial^2}{\partial x^2} + \frac{\partial^2}{\partial y^2})\Lambda(x, y, z) \end{cases} \tag{A.9}$$

so, substitute in the potential solution, we get displacements,

$$\begin{cases} u(k_x,z;k_y) = -ik_x(A^-e^{-\alpha z}+A^+e^{\alpha z}) - ik_y(B^-e^{-\beta z}+B^+e^{\beta z}) + ik_x\beta(C^-e^{-\beta z}-C^+e^{\beta z}) \\ v(k_x,z;k_y) = -ik_y(A^-e^{-\alpha z}+A^+e^{\alpha z}) + ik_x(B^-e^{-\beta z}+B^+e^{\beta z}) + ik_y\beta(C^-e^{-\beta z}-C^+e^{\beta z}) \\ w(k_x,z;k_y) = -\alpha(A^-e^{-\alpha z}-A^+e^{\alpha z}) + (k_x^2+k_y^2)(C^-e^{-\beta z}+C^+e^{\beta z}) \end{cases} \tag{A.10}$$

For stresses, we have

$$\begin{cases} \sigma_{zz}(x,y,z) = \lambda(\frac{\partial u}{\partial x}+\frac{\partial v}{\partial y}+\frac{\partial w}{\partial z}) + 2\mu\frac{\partial w}{\partial z} = (\lambda+2\mu)\frac{\partial w}{\partial z} + \lambda(\frac{\partial u}{\partial x}+\frac{\partial v}{\partial y}) \\ \sigma_{zx}(x,y,z) = \mu(\frac{\partial w}{\partial x}+\frac{\partial u}{\partial z}) \\ \sigma_{zy}(x,y,z) = \mu(\frac{\partial w}{\partial y}+\frac{\partial v}{\partial z}) \end{cases} \tag{A.11}$$

$$\begin{aligned} &\sigma_{zz}(k_x,z;k_y) \\ &= (\lambda+2\mu)(\alpha^2(A^-e^{-\alpha z}+A^+e^{\alpha z}) - (k_x^2+k_y^2)\beta(C^-e^{-\beta z}-C^+e^{\beta z})) \\ &\quad + \lambda(-k_x^2(A^-e^{-\alpha z}+A^+e^{\alpha z}) - k_xk_y(B^-e^{-\beta z}+B^+e^{\beta z}) + k_x^2\beta(C^-e^{-\beta z}-C^+e^{\beta z})) \\ &\quad + \lambda(-k_y^2(A^-e^{-\alpha z}+A^+e^{\alpha z}) + k_xk_y(B^-e^{-\beta z}+B^+e^{\beta z}) + k_y^2\beta(C^-e^{-\beta z}-C^+e^{\beta z})) \\ &= \mu(2(k_x^2+k_y^2)-k_s^2)(A^-e^{-\alpha z}+A^+e^{\alpha z}) - 2\mu(k_x^2+k_y^2)\beta(C^-e^{-\beta z}-C^+e^{\beta z}) \end{aligned} \tag{A.12}$$

$$\begin{aligned} &\sigma_{zx}(k_x,z;k_y) \\ &= \mu(ik_x\alpha(A^-e^{-\alpha z}-A^+e^{\alpha z}) - ik_x(k_x^2+k_y^2)(C^-e^{-\beta z}+C^+e^{\beta z})) \\ &\quad + \mu(ik_x\alpha(A^-e^{-\alpha z}-A^+e^{\alpha z}) + ik_y\beta(B^-e^{-\beta z}-B^+e^{\beta z}) \\ &\quad - ik_x\beta^2(C^-e^{-\beta z}+C^+e^{\beta z})) \\ &= 2i\mu k_x\alpha(A^-e^{-\alpha z}-A^+e^{\alpha z}) + i\mu k_y\beta(B^-e^{-\beta z}-B^+e^{\beta z}) \\ &\quad - i\mu k_x(2(k_x^2+k_y^2)-k_s^2)(C^-e^{-\beta z}+C^+e^{\beta z}) \end{aligned} \tag{A.13}$$

$$\begin{aligned} &\sigma_{zy}(k_x,z;k_y) \\ &= \mu(ik_y\alpha(A^-e^{-\alpha z}-A^+e^{\alpha z}) - ik_y(k_x^2+k_y^2)(C^-e^{-\beta z}+C^+e^{\beta z})) \end{aligned}$$

$$+\mu(ik_y\alpha(A^-e^{-\alpha z}-A^+e^{\alpha z})-ik_y\beta^2(C^-e^{-\beta z}+C^+e^{\beta z})-ik_x\beta(B^-e^{-\beta z}-B^+e^{\beta z}))$$

$$= 2i\mu k_y\alpha(A^-e^{-\alpha z}-A^+e^{\alpha z})-i\mu k_x\beta(B^-e^{-\beta z}-B^+e^{\beta z})$$

$$-i\mu k_y(2(k_x^2+k_y^2)-k_s^2)(C^-e^{-\beta z}+C^+e^{\beta z}) \tag{A.14}$$

A.0.3 Source Field

Compressional Point Source

The source field $\hat{\phi}(x,y,z)$ safisfies the following equation,

$$(\nabla^2+k_p^2)\hat{\phi}(x,y,z)=-S_w\delta(x)\delta(y)\delta(z-z_s) \tag{A.15}$$

where S_w is the source strength. Apply Fourier Transform with respect to x and y, we get

$$(\frac{\partial^2}{\partial z^2}-\alpha^2)\hat{\phi}(k_x,z;k_y)=-\frac{S_w}{4\pi^2}\delta(z-z_s) \tag{A.16}$$

so

$$\hat{\phi}(k_x,z;k_y)=\frac{S_w}{8\pi^2\alpha}e^{-\alpha|z-z_s|} \tag{A.17}$$

from equation (A.9), we get

$$\begin{cases}\hat{u}(k_x,z;k_y)=-\frac{ik_xS_w}{8\pi^2\alpha}e^{-\alpha|z-z_s|}\\ \hat{v}(k_x,z;k_y)=-\frac{ik_yS_w}{8\pi^2\alpha}e^{-\alpha|z-z_s|}\\ \hat{w}(k_x,z;k_y)=-\frac{S_w}{8\pi^2}sign(z-z_s)e^{-\alpha|z-z_s|}\end{cases} \tag{A.18}$$

from equation (A.11)

$$\hat{\sigma}_{zz} = (\lambda+2\mu)\frac{S_w\alpha}{8\pi^2}e^{-\alpha|z-z_s|}+\lambda(-\frac{k_x^2S_w}{8\pi^2\alpha}-\frac{k_y^2S_w}{8\pi^2\alpha})e^{-\alpha|z-z_s|}$$

$$= \frac{\mu S_w}{8\pi^2\alpha}(2(k_x^2+k_y^2)-k_s^2)e^{-\alpha|z-z_s|} \tag{A.19}$$

$$\hat{\sigma}_{zx} = \mu(\frac{ik_xS_w}{8\pi^2}sign(z-z_s)e^{-\alpha|z-z_s|}+\frac{ik_xS_w}{8\pi^2}sign(z-z_s)e^{-\alpha|z-z_s|})$$

$$= \frac{i\mu k_xS_w}{4\pi^2}sign(z-z_s)e^{-\alpha|z-z_s|} \tag{A.20}$$

$$\hat{\sigma}_{zy} = \mu(\frac{ik_yS_w}{8\pi^2}sign(z-z_s)e^{-\alpha|z-z_s|}+\frac{ik_yS_w}{8\pi^2}sign(z-z_s)e^{-\alpha|z-z_s|})$$

$$= \frac{i\mu k_y S_w}{4\pi^2} sign(z - z_s) e^{-\alpha|z-z_s|} \tag{A.21}$$

Point Force Source of Arbitrary Direction

Assume the source is (F_x, F_y, F_z), define

$$\begin{cases} \phi_0(k_x, z; k_y) = -\frac{1}{\rho\omega^2}\frac{1}{8\pi^2\alpha} e^{-\alpha|z-z_s|} \\ \psi_0(k_x, z; k_y) = -\frac{1}{\rho\omega^2}\frac{1}{8\pi^2\beta} e^{-\beta|z-z_s|} \end{cases} \tag{A.22}$$

the displacement potentials for the source field are

$$\begin{cases} \phi(x, y, z) = \vec{F} \bullet \nabla\phi_0(x, y, z) \\ \vec{\psi}(x, y, z) = \nabla \times (-F_x\psi_0(x, y, z), -F_y\psi_0(x, y, z), -F_z\psi_0(x, y, z)) \end{cases} \tag{A.23}$$

so,

$$\phi(k_x, z; k_y) = \frac{ik_x F_x}{\rho\omega^2}\frac{1}{8\pi^2\alpha} e^{-\alpha|z-z_s|} + \frac{ik_y F_y}{\rho\omega^2}\frac{1}{8\pi^2\alpha} e^{-\alpha|z-z_s|} + \frac{F_z}{\rho\omega^2} sign(z - z_s)\frac{1}{8\pi^2} e^{-\alpha|z-z_s|} \tag{A.24}$$

$$\begin{aligned} \vec{\psi}(k_x, z; k_y) &= \{\vec{e}_x[0 + \beta sign(z - z_s)F_y - ik_y F_z] \\ &\quad + \vec{e}_y[-\beta sign(z - z_s)F_x + 0 + ik_x F_z] \\ &\quad + \vec{e}_z[ik_y F_x - ik_x F_y + 0]\}\frac{1}{\rho\omega^2}\frac{1}{8\pi^2\beta} e^{-\beta|z-z_s|} \end{aligned} \tag{A.25}$$

From equation (A.9)

$$\begin{aligned} u(k_z, z; k_y) = \\ &[k_x^2 F_x + k_x k_y F_y - ik_x\alpha sign(z - z_s)F_z]\frac{1}{\rho\omega^2}\frac{1}{8\pi^2\alpha} e^{-\alpha|z-z_s|} \\ &+ [(k_s^2 - k_x^2)F_x - k_x k_y F_y + ik_x\beta sign(z - z_s)F_z]\frac{1}{\rho\omega^2}\frac{1}{8\pi^2\beta} e^{-\beta|z-z_s|} \end{aligned} \tag{A.26}$$

$$\begin{aligned} v(k_z, z; k_y) = \\ &[k_x k_y F_x + k_y^2 F_y - ik_y\alpha sign(z - z_s)F_z]\frac{1}{\rho\omega^2}\frac{1}{8\pi^2\alpha} e^{-\alpha|z-z_s|} \end{aligned}$$

$$+ [-k_x k_y F_x + (k_s^2 - k_y^2)F_y + ik_y \beta sign(z - z_s)F_z] \frac{1}{\rho\omega^2} \frac{1}{8\pi^2\beta} e^{-\beta|z-z_s|} \quad \text{(A.27)}$$

$$w(k_z, z; k_y) =$$
$$[-ik_x \alpha sign(z - z_s)F_x - ik_y \alpha sign(z - z_s)F_y - \alpha^2 F_z] \frac{1}{\rho\omega^2} \frac{1}{8\pi^2\alpha} e^{-\alpha|z-z_s|}$$
$$+ [ik_x \beta sign(z - z_s)F_x + ik_y \beta sign(z - z_s)F_y + (k_x^2 + k_y^2)F_z] \frac{1}{\rho\omega^2} \frac{1}{8\pi^2\beta} e^{-\beta|z-z_s|} \quad \text{(A.28)}$$

and from equation (A.11)

$$\hat{\sigma}_{zz}(k_x, z; k_y) =$$
$$\mu[2(k_x^2 + k_y^2) - k_s^2] \frac{1}{\rho\omega^2} \frac{1}{8\pi^2\alpha} e^{-\alpha|z-z_s|} \{ik_x F_x + ik_y F_y + \alpha sign(z - z_s)F_z\}$$
$$- 2\mu \frac{1}{\rho\omega^2} \frac{1}{8\pi^2} e^{-\beta|z-z_s|} \{ik_x \beta F_x + ik_y \beta F_y + (k_x^2 + k_y^2) sign(z - z_s)F_z\} \quad \text{(A.29)}$$

$$\hat{\sigma}_{zx}(k_x, z; k_y) =$$
$$\frac{2\mu k_x}{\rho\omega^2} \frac{1}{8\pi^2} e^{-\alpha|z-z_s|} \{-k_x sign(z - z_s)F_x - k_y sign(z - z_s)F_y + i\alpha F_z\}$$
$$+ \frac{\mu}{\rho\omega^2} \frac{1}{8\pi^2\beta} e^{-\beta|z-z_s|} \{[2k_x^2 - k_s^2]\beta sign(z - z_s)F_x + 2k_x k_y \beta sign(z - z_s)F_y$$
$$- ik_x[2(k_x^2 + k_y^2) - k_s^2]F_z\} \quad \text{(A.30)}$$

$$\hat{\sigma}_{zy}(k_x, z; k_y) =$$
$$\frac{2\mu k_y}{\rho\omega^2} \frac{1}{8\pi^2} e^{-\alpha|z-z_s|} \{-k_x sign(z - z_s)F_x - k_y sign(z - z_s)F_y + i\alpha F_z\}$$
$$+ \frac{\mu}{\rho\omega^2} \frac{1}{8\pi^2\beta} e^{-\beta|z-z_s|} \{2k_x k_y \beta sign(z - z_s)F_x + [2k_y^2 - k_s^2]\beta sign(z - z_s)F_y$$
$$- ik_y[2(k_x^2 + k_y^2) - k_s^2]F_z\} \quad \text{(A.31)}$$

A.0.4 Fluid Medium

Homogeneous Solution

The results before are for the elastic medium, for fluid we have the acoustic wave equation

$$(\nabla^2 + k_p^2)\phi(x, y, z) = 0 \tag{A.32}$$

Applying the Fourier Transform for x and y, it becomes

$$(\frac{\partial^2}{\partial z^2} - \alpha^2)\phi(k_x, z; k_y) = 0 \tag{A.33}$$

where $\alpha = (k_x^2 + k_y^2 - k_p^2)^{1/2}$.

The solution is of the form

$$\phi(k_x, z; k_y) = A^- e^{-\alpha z} + A^+ e^{\alpha z} \tag{A.34}$$

but we have

$$\vec{u}(x, y, z) = \nabla\phi(x, y, z) \tag{A.35}$$

$$\begin{cases} \sigma_{zz}(x, y, z) = \lambda\nabla^2\phi = -\rho\omega^2\phi \\ \sigma_{zx}(x, y, z) = 0 \\ \sigma_{zy}(x, y, z) = 0 \end{cases} \tag{A.36}$$

thus

$$\begin{cases} u(k_x, z; k_y) = -ik_x(A^- e^{-\alpha z} + A^+ e^{\alpha z}) \\ v(k_x, z; k_y) = -ik_y(A^- e^{-\alpha z} + A^+ e^{\alpha z}) \\ w(k_x, z; k_y) = -\alpha(A^- e^{-\alpha z} - A^+ e^{\alpha z}) \\ \sigma_{zz}(k_x, z; k_y) = -\rho\omega^2(A^- e^{-\alpha z} + A^+ e^{\alpha z}) \\ \sigma_{zx}(k_x, z; k_y) = 0 \\ \sigma_{zy}(k_x, z; k_y) = 0 \end{cases} \tag{A.37}$$

Source Field

Similar to compressional source in solid, here for fluid we also have

$$\hat{\phi}(k_x, z; k_y) = \frac{S_w}{8\pi^2\alpha} e^{-\alpha|z-z_s|} \tag{A.38}$$

so,

$$\begin{cases} \hat{u}(k_x, z; k_y) = -\frac{ik_x S_w}{8\pi^2\alpha} e^{-\alpha|z-z_s|} \\ \hat{v}(k_x, z; k_y) = -\frac{ik_y S_w}{8\pi^2\alpha} e^{-\alpha|z-z_s|} \\ \hat{w}(k_x, z; k_y) = -\frac{S_w}{8\pi^2} sign(z-z_s) e^{-\alpha|z-z_s|} \\ \hat{\sigma}_{zz}(k_x, z; k_y) = -\frac{\rho\omega^2 S_w}{8\pi^2\alpha} e^{-\alpha|z-z_s|} \\ \hat{\sigma}_{zx}(k_x, z; k_y) = 0 \\ \hat{\sigma}_{zy}(k_x, z; k_y) = 0 \end{cases} \tag{A.39}$$

A.0.5 Solution Technique

Define $S2 = k_x^2 + k_y^2$, $S = (S2)^{1/2}$,

$$\begin{cases} con1 = \mu \\ con2 = \mu[2(k_x^2 + k_y^2) - k_s^2] \\ con3 = \mu 2S\alpha \\ con4 = \mu 2S\beta \\ con5 = \mu\frac{ik_x}{s}[2(k_x^2 + k_y^2) - k_s^2] \\ con6 = \mu\frac{ik_y}{s}[2(k_x^2 + k_y^2) - k_s^2] \\ con7 = \mu 2ik_x\alpha \\ con8 = \mu 2ik_y\alpha \\ con9 = \mu ik_y\beta \\ con10 = \mu ik_x\beta \end{cases} \tag{A.40}$$

Then the field can be writen as

$$\begin{bmatrix} \omega \\ u \\ v \\ \sigma_{zz} \\ \sigma_{zx} \\ \sigma_{zy} \end{bmatrix} = [A][B] + [R] \tag{A.41}$$

wher [R] is the contribution of source,

$$[B] = \begin{bmatrix} A^- \\ SC^- \\ B^- \\ A^+ \\ SC^+ \\ B^+ \end{bmatrix} \tag{A.42}$$

Assume there is N layers, the global set of equations is

$$\begin{bmatrix} [A_{1,l}] & [-A_{2,u}] & & & \\ & [A_{2,l}] & [-A_{3,u}] & & \\ & & & & \\ & & & [A_{N-1,l}] & [-A_{N,u}] \end{bmatrix} \bullet \begin{bmatrix} B_1 \\ B_2 \\ \vdots \\ B_N \end{bmatrix} = \begin{bmatrix} R_{2,u} \\ R_{3,u} \\ \vdots \\ R_{N,u} \end{bmatrix} - \begin{bmatrix} R_{1,l} \\ R_{2,l} \\ \vdots \\ R_{N-1,l} \end{bmatrix} \tag{A.43}$$

For elastic media,

$$[A_{n,u}] = \begin{bmatrix} \alpha & -S & 0 & -\alpha & -S & 0 \\ ik_x & -ik_x\beta/S & ik_y & ik_x & ik_x\beta/S & ik_y \\ ik_y & -ik_y\beta/S & -ik_x & ik_y & ik_y\beta/S & -ik_x \\ -con2 & con4 & 0 & -con2 & -con4 & 0 \\ -con7 & con5 & -con9 & con7 & con5 & con9 \\ -con8 & con6 & con10 & con8 & con6 & -con10 \end{bmatrix} \tag{A.44}$$

For fluid medium, $con1 = \rho\omega^2$

$$[A_{n,u}] = \begin{bmatrix} \alpha & 0 & 0 & -\alpha & 0 & 0 \\ ik_x & 0 & 0 & ik_x & 0 & 0 \\ ik_y & 0 & 0 & ik_y & 0 & 0 \\ con1 & 0 & 0 & con1 & 0 & 0 \\ 0 & 0 & 0 & 0 & 0 & 0 \\ 0 & 0 & 0 & 0 & 0 & 0 \end{bmatrix} \tag{A.45}$$

$$[A_{n,l}(k_x, z; k_y)] = [A_{n,u}(k_x, z; k_y)] I_n(k_x, z; k_y) \tag{A.46}$$

where

$$[I_n(k_x, z; k_y)] = \begin{bmatrix} e^{-\alpha z_n} & 0 & 0 & 0 & 0 & 0 \\ 0 & e^{-\beta z_n} & 0 & 0 & 0 & 0 \\ 0 & 0 & e^{-\beta z_n} & 0 & 0 & 0 \\ 0 & 0 & 0 & e^{\alpha z_n} & 0 & 0 \\ 0 & 0 & 0 & 0 & e^{\beta z_n} & 0 \\ 0 & 0 & 0 & 0 & 0 & e^{\beta z_n} \end{bmatrix} \tag{A.47}$$

Now that we have defined all matrix [A] and right hand side vector R in Eq. (A.43), it can be solved for the vector B, i.e., the amplitudes of the up-going and down-going potentials in each layer.

Appendix B

The Point Force Field Under Cylindrical Coordinate Transformation

B.1 Transformation of Bessel Functions

Here, we try to transform the sources to (r_0, z_0, θ_0). From Graf's Theorem (Abramowitz et. al., "Handbook of Mathematical Functions", P.363), for the geometry in Fig. B-1, we have:

$$J_k(w) \begin{matrix} cos \\ sin \end{matrix} k\alpha = \sum_{m=-\infty}^{\infty} J_{k+m}(u) J_m(v) \begin{matrix} cos \\ sin \end{matrix} m\beta. \tag{B.1}$$

In Fig. B-2, we illustrated our coordinate transform. From Eq.(B.1), we have:

$$J_k(s\tilde{r}) \begin{matrix} cos \\ sin \end{matrix} k(\tilde{\theta} - \theta_0) = \sum_{m=-\infty}^{\infty} J_{k+m}(sr_0) J_m(sr) \begin{matrix} cos \\ sin \end{matrix} m(\pi - (\theta - \theta_0)). \tag{B.2}$$

For $k = 0$, we get:

$$J_0(s\tilde{r}) = \sum_{m=-\infty}^{\infty} (-1)^m J_m(sr_0) J_m(sr) cos(m(\theta - \theta_0)); \tag{B.3}$$

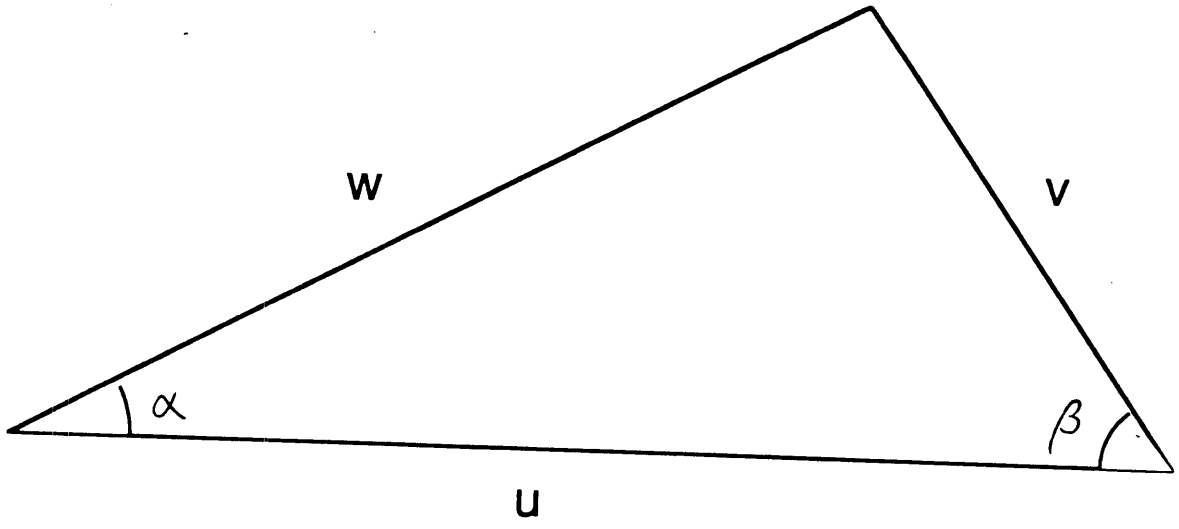

Fig. B-1

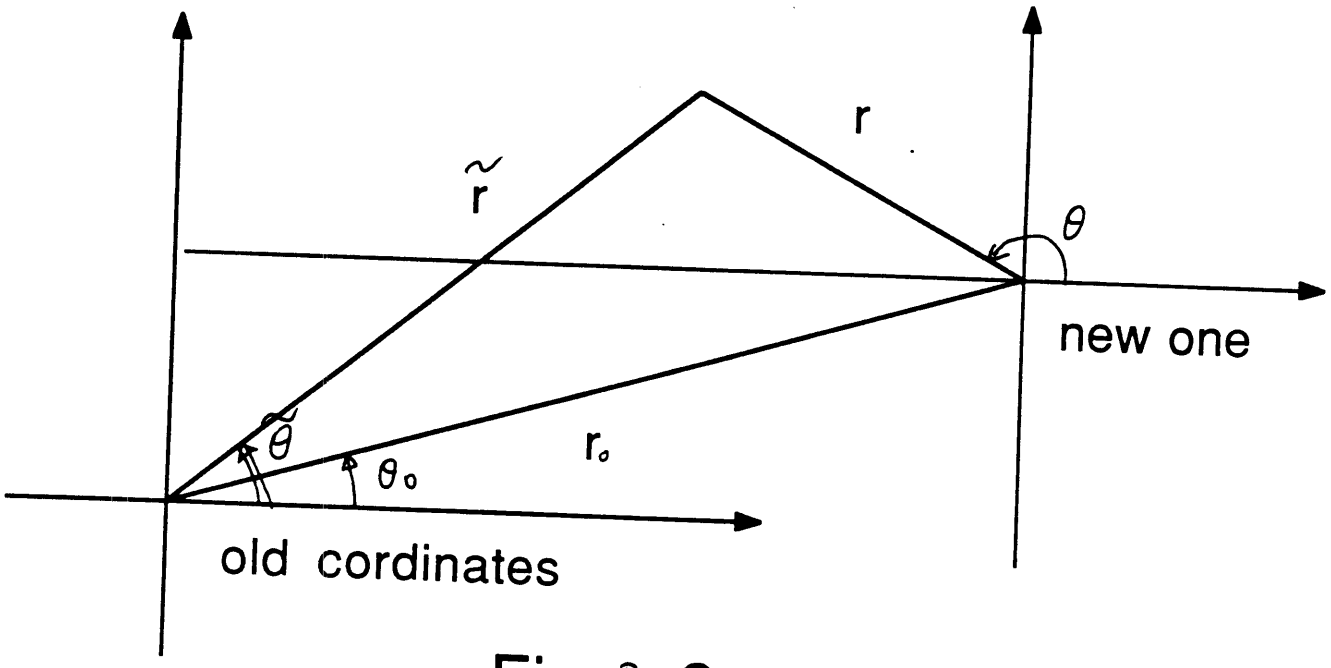

Fig. B-2

for $k = 1$, we get:

$$J_1(s\tilde{r}) \begin{matrix} cos \\ sin \end{matrix} (\tilde{\theta} - \theta_0)$$

$$= \sum_{m=-\infty}^{\infty} (-1)^m J_{m+1}(sr_0) J_m(sr) \begin{matrix} cos \\ sin \end{matrix} m(\theta - \theta_0). \tag{B.4}$$

By simple linear combination, we end up with:

$$J_1(s\tilde{r}) \begin{matrix} cos \\ sin \end{matrix} \tilde{\theta} = \sum_{m=-\infty}^{\infty} (-1)^m J_{m+1}(sr_0) J_m(sr) \begin{matrix} cos \\ sin \end{matrix} ((m+1)\theta_0 - m\theta). \tag{B.5}$$

B.2 Scalar potential expression of the field

Let:

$$\vec{\psi}(r, \theta, z) = \nabla \times (0, 0, \Lambda) + (0, 0, \psi), \tag{B.6}$$

then $\vec{u} = \nabla\phi(r, \theta, z) + \nabla \times \vec{\psi}(r, \theta, z)$ is the displacement field. Expressed in components:

$$\begin{cases} u_z = \frac{\partial}{\partial z}\phi - \frac{1}{r}\frac{\partial}{\partial r}(r\frac{\partial}{\partial r}\Lambda) - \frac{1}{r^2}\frac{\partial^2}{\partial^2\theta}\Lambda, \\ u_r = \frac{\partial}{\partial r}\phi + \frac{\partial^2}{\partial z \partial r}\Lambda + \frac{1}{r}\frac{\partial}{\partial \theta}\psi, \\ u_\theta = \frac{1}{r}\frac{\partial}{\partial \theta}\phi + \frac{1}{r}\frac{\partial^2}{\partial z \partial \theta}\Lambda - \frac{\partial}{\partial r}\psi, \end{cases} \tag{B.7}$$

and stresses are:

$$\begin{cases} \sigma_{zz}^m = \lambda\nabla^2\phi^m + 2\mu\frac{\partial}{\partial z}u_z^m; \\ \sigma_{zr}^m \pm \sigma_{z\theta}^m = \mu(\frac{\partial}{\partial z}(u_r^m \pm u_\theta^m) + (\frac{\partial}{\partial r} \mp \frac{m}{r})u_z^m). \end{cases} \tag{B.8}$$

B.3 Transformation of point force field

Notice that potentials ϕ, Λ and ψ are invariands under our coordinates tranformation. We just have to utilize the transformation of the Bessel functions to express them in the new coordinate system. The potentials generated by a point force at the origin

have been derived [39].

B.3.1 F_z Source

For a force in Z direction, the integrand of the potentials are (omitting $\frac{e^{i\omega t}}{4\pi\rho\omega^2}$):

$$\begin{cases} \phi = F_z \zeta s e^{-\alpha|z-z_0|} J_0(s\tilde{r}), \\ \Lambda = F_z \frac{s}{\beta} e^{-\beta|z-z_0|} J_0(s\tilde{r}), \\ \psi = 0, \end{cases} \tag{B.9}$$

where $\zeta = sign(z - z_0)$, h is the media compressional wavenumber, k is the media shear wavenumber and $\alpha = \sqrt{s^2 - h^2}, \beta = \sqrt{s^2 - k^2}$. By eq. (B.3), the potentials can be expressed in the new coordinates:

$$\begin{cases} \phi = F_z \zeta s e^{-\alpha|z-z_0|} \sum_{m=-\infty}^{\infty} (-1)^m J_m(sr_0) J_m(sr) cos(m(\theta - \theta_0)); \\ \Lambda = F_z \frac{s}{\beta} e^{-\beta|z-z_0|} \sum_{m=-\infty}^{\infty} (-1)^m J_m(sr_0) J_m(sr) cos(m(\theta - \theta_0)); \\ \psi = 0. \end{cases} \tag{B.10}$$

Then, by eq. (B.7) and (B.8), the displacement and stress field expressed in the new coordinates is:

$$\begin{cases} u_z^m = (-1)^m F_z (-s\alpha e^{-\alpha|z-z_0|} + \frac{s^3}{\beta} e^{-\beta|z-z_0|}) J_m(sr_0) J_m(sr) \begin{matrix} cos \\ sin \end{matrix} m\theta_0, \\ u_r^m \pm u_\theta^m = \mp (-1)^m F_z \zeta s^2 (e^{-\alpha|z-z_0|} - e^{-\beta|z-z_0|}) J_m(sr_0) J_{m\pm1}(sr) \begin{matrix} cos \\ sin \end{matrix} m\theta_0, \\ \sigma_{zz}^m = (-1)^m \mu F_z \zeta (s(2s^2 - k^2) e^{-\alpha|z-z_0|} - 2s^3 e^{-\beta|z-z_0|}) J_m(sr_0) J_m(sr) \begin{matrix} cos \\ sin \end{matrix} m\theta_0, \\ \sigma_{zr}^m \pm \sigma_{z\theta}^m = \pm (-1)^m \mu F_z (2\alpha s^2 e^{-\alpha|z-z_0|} - \frac{s^2}{\beta}(2s^2 - k^2) e^{-\beta|z-z_0|}) J_m(sr_0) J_{m\pm1}(sr) \begin{matrix} cos \\ sin \end{matrix} m\theta_0, \end{cases} \tag{B.11}$$

where we have used the notion:

$$\begin{cases} u_z = \sum_{m=-\infty}^{\infty} u_z^m \begin{matrix} cos \\ sin \end{matrix} m\theta, \\ u_r = \sum_{m=-\infty}^{\infty} u_r^m \begin{matrix} cos \\ sin \end{matrix} m\theta, \\ u_\theta = \sum_{m=-\infty}^{\infty} u_\theta^m \begin{matrix} sin \\ -cos \end{matrix} m\theta, \\ \sigma_{zz} = \sum_{m=-\infty}^{\infty} \sigma_{zz}^m \begin{matrix} cos \\ sin \end{matrix} m\theta, \\ \sigma_{zr} = \sum_{m=-\infty}^{\infty} \sigma_{zr}^m \begin{matrix} cos \\ sin \end{matrix} m\theta, \\ \sigma_{z\theta} = \sum_{m=-\infty}^{\infty} \sigma_{z\theta}^m \begin{matrix} sin \\ -cos \end{matrix} m\theta. \end{cases} \tag{B.12}$$

B.3.2 F_x Source

In old Coordinates $(\tilde{r}, \tilde{\theta}, z)$, omitting $\frac{e^{i\omega t}}{4\pi\rho\omega^2}$,

$$\begin{cases} \phi = F_x \frac{s^2}{\alpha} e^{-\alpha|z-z_0|} J_1(s\tilde{r}) cos\tilde{\theta}; \\ \Lambda = F_x \zeta e^{-\beta|z-z_0|} J_1(s\tilde{r}) cos\tilde{\theta}; \\ \psi = F_x \frac{k^2}{\beta} e^{-\beta|z-z_0|} J_1(s\tilde{r}) sin\tilde{\theta}. \end{cases} \tag{B.13}$$

In the new coordinates (r, θ, z),

$$\begin{cases} \phi = F_x \frac{s^2}{\alpha} e^{-\alpha|z-z_0|} \sum_{m=-\infty}^{\infty} (-1)^m J_{m+1}(sr_0) J_m(sr) cos((m+1)\theta_0 - m\theta); \\ \Lambda = F_x \zeta e^{-\beta|z-z_0|} \sum_{m=-\infty}^{\infty} (-1)^m J_{m+1}(sr_0) J_m(sr) cos((m+1)\theta_0 - m\theta); \\ \psi = F_x \frac{k^2}{\beta} e^{-\beta|z-z_0|} \sum_{m=-\infty}^{\infty} (-1)^m J_{m+1}(sr_0) J_m(sr) sin((m+1)\theta_0 - m\theta). \end{cases} \tag{B.14}$$

Then, we have, in the new coordinates:

$$\begin{cases} u_z^m = (-1)^m F_x \zeta s^2 (-e^{-\alpha|z-z_0|} + e^{-\beta|z-z_0|}) J_{m+1}(sr_0) J_m(sr) \begin{matrix} cos \\ sin \end{matrix} (m+1)\theta_0, \\ u_r^m \pm u_\theta^m = (-1)^m F_x (\mp \frac{s^3}{\alpha} e^{-\alpha|z-z_0|} + \frac{s}{\beta}(k^2 \pm \beta^2) e^{-\beta|z-z_0|}) J_{m+1}(sr_0) J_{m\pm1}(sr) \begin{matrix} cos \\ sin \end{matrix} (m+1)\theta_0, \\ \sigma_{zz}^m = (-1)^m \mu F_x (\frac{s^2}{\alpha}(2s^2 - k^2) e^{-\alpha|z-z_0|} - 2\beta s^2 e^{-\beta|z-z_0|}) J_{m+1}(sr_0) J_m(sr) \begin{matrix} cos \\ sin \end{matrix} (m+1)\theta_0, \\ \sigma_{zr}^m \pm \sigma_{z\theta}^m = (-1)^m \mu F_x \zeta (\pm 2s^3 e^{-\alpha|z-z_0|} + Q_\pm e^{-\beta|z-z_0|}) J_{m+1}(sr_0) J_{m\pm1}(sr) \begin{matrix} cos \\ sin \end{matrix} (m+1)\theta_0, \end{cases} \tag{B.15}$$

where $Q_+ = -2s^3$, and $Q_- = 2s\beta^2$.

Appendix C

The Relationship of Kernels in Cartesian and Cylindrical Coordinates

In cylindrical coordinates:

$$\vec{u}(r,\theta,z) = \hat{e_r}u_r(r,\theta,z) + \hat{e_\theta}u_\theta(r,\theta,z) + \hat{e_z}u_z(r,\theta,z) \tag{C.1}$$

and the components can be expanded as:

$$\begin{cases} u_r(r,\theta,z) = \sum_m [U^m_{r1}(r,z)cos(m\theta) + U^m_{r2}(r,z)sin(m\theta)] \\ u_\theta(r,\theta,z) = \sum_m [U^m_{\theta 1}(r,z)sin(m\theta) - U^m_{\theta 2}(r,z)cos(m\theta)] \\ u_z(r,\theta,z) = \sum_m [U^m_{z1}(r,z)cos(m\theta) + U^m_{z2}(r,z)sin(m\theta)] \end{cases} \tag{C.2}$$

where

$$\begin{cases} U^m_{zi}(r,z) = \int Z^m_i(k_r,z)J_m(k_r r)k_r dk_r \\ U^m_{ri}(r,z) + U^m_{\theta i}(r,z) = \int [R^m_i(k_r,z) + \Theta^m_i(k_r,z)]J_{m+1}(k_r r)k_r dk_r \\ U^m_{ri}(r,z) - U^m_{\theta i}(r,z) = \int [R^m_i(k_r,z) - \Theta^m_i(k_r,z)]J_{m-1}(k_r r)k_r dk_r \end{cases} \tag{C.3}$$

for $i = 1, 2$.

In Cartisian Coordinates:

$$\vec{u}(r,\theta,z) = \hat{e_x}u_x(r,\theta,z) + \hat{e_y}u_y(r,\theta,z) + \hat{e_z}u_z(r,\theta,z) \tag{C.4}$$

$$\begin{cases} u_x(r,\theta,z) = \sum_m [U^m_{x1}(r,z)cos(m\theta) + U^m_{x2}(r,z)sin(m\theta)] \\ u_y(r,\theta,z) = \sum_m [U^m_{y1}(r,z)sin(m\theta) - U^m_{y2}(r,z)cos(m\theta)] \\ u_z(r,\theta,z) = \sum_m [U^m_{z1}(r,z)cos(m\theta) + U^m_{z2}(r,z)sin(m\theta)] \end{cases} \tag{C.5}$$

$$\begin{cases} U^m_{xi}(r,z) = \int X^m_i(k_r,z)J_m(k_r r)k_r dk_r \\ U^m_{yi}(r,z) = \int Y^m_i(k_r,z)J_m(k_r r)k_r dk_r \\ U^m_{zi}(r,z) = \int Z^m_i(k_r,z)J_m(k_r r)k_r dk_r \end{cases} \tag{C.6}$$

for $i = 1, 2$.

But,

$$\begin{aligned} & u_r(r,\theta,z) \\ &= u_x(r,\theta,z)cos\theta + u_y(r,\theta,z)sin\theta \\ &= \sum_m [U^m_{x1}(r,z)cos(m\theta)cos\theta + U^m_{x2}(r,z)sin(m\theta)cos\theta \\ &\quad + U^m_{y1}(r,z)sin(m\theta)sin\theta - U^m_{y2}(r,z)cos(m\theta)sin\theta \\ &= \sum_m \frac{1}{2}\{U^m_{x1}(r,z)[cos(m+1)\theta + cos(m-1)\theta] \\ &\quad + U^m_{x2}(r,z)[sin(m+1)\theta + sin(m-1)\theta] \\ &\quad + U^m_{y1}(r,z)[-cos(m+1)\theta + cos(m-1)\theta] \\ &\quad + U^m_{y2}(r,z)[-sin(m+1)\theta + sin(m-1)\theta]\} \end{aligned} \tag{C.7}$$

$$\begin{aligned} & u_\theta(r,\theta,z) \\ &= -u_x(r,\theta,z)sin\theta + u_y(r,\theta,z)cos\theta \\ &= \sum_m [-U^m_{x1}(r,z)cos(m\theta)sin\theta - U^m_{x2}(r,z)sin(m\theta)sin\theta \end{aligned}$$

$$
\begin{aligned}
& +U_{y1}^m(r,z)sin(m\theta)cos\theta - U_{y2}^m(r,z)cos(m\theta)cos\theta \\
= & \sum_m \frac{1}{2}\{U_{x1}^m(r,z)[-sin(m+1)\theta + sin(m-1)\theta] \\
& +U_{x2}^m(r,z)[cos(m+1)\theta - cos(m-1)\theta] \\
& +U_{y1}^m(r,z)[sin(m+1)\theta + sin(m-1)\theta] \\
& +U_{y2}^m(r,z)[-cos(m+1)\theta - cos(m-1)\theta]\}
\end{aligned} \tag{C.8}
$$

From (22), (23) and (17), we get:

$$
\begin{cases}
U_{r1}^m(r,z) = \frac{1}{2}[U_{x1}^{m-1}(r,z) + U_{x1}^{m+1}(r,z) - U_{y1}^{m-1}(r,z) + U_{y1}^{m+1}(r,z)] \\
U_{r2}^m(r,z) = \frac{1}{2}[U_{x2}^{m-1}(r,z) + U_{x2}^{m+1}(r,z) - U_{y2}^{m-1}(r,z) + U_{y2}^{m+1}(r,z)] \\
U_{\theta 1}^m(r,z) = \frac{1}{2}[-U_{x1}^{m-1}(r,z) + U_{x1}^{m+1}(r,z) + U_{y1}^{m-1}(r,z) + U_{y1}^{m+1}(r,z)] \\
U_{\theta 2}^m(r,z) = \frac{1}{2}[-U_{x2}^{m-1}(r,z) + U_{x2}^{m+1}(r,z) + U_{y2}^{m-1}(r,z) + U_{y2}^{m+1}(r,z)]
\end{cases} \tag{C.9}
$$

So

$$
\begin{cases}
U_{r1}^m(r,z) + U_{\theta 1}^m(r,z) = U_{x1}^{m+1}(r,z) + U_{y1}^{m+1}(r,z) \\
U_{r1}^m(r,z) - U_{\theta 1}^m(r,z) = U_{x1}^{m-1}(r,z) - U_{y1}^{m-1}(r,z) \\
U_{r2}^m(r,z) + U_{\theta 2}^m(r,z) = U_{x2}^{m+1}(r,z) + U_{y2}^{m+1}(r,z) \\
U_{r2}^m(r,z) - U_{\theta 2}^m(r,z) = U_{x2}^{m-1}(r,z) - U_{y2}^{m-1}(r,z)
\end{cases} \tag{C.10}
$$

Thus, from equations (25), (18) and (21), we conclude that

$$
R_i^m(k_r,z) \pm \Theta_i^m(k_r,z) = X_i^{m\pm 1}(k_r,z) \pm Y_i^{m\pm 1}(k_r,z) \tag{C.11}
$$

for $i = 1, 2$.

From perturbation code, we got $u_x(x,y,z_0)$, $u_y(x,y,z_0)$ and want to find $X_i^m(k_r,z_0)$, $Y_i^m(k_r,z_0)$, then $R_i^m(k_r,z_0) \pm \Theta_i^m(k_r,z_0)$. We can proceed by changing variables in $u_x(x,y,z_0)$ to $u_x(r,\theta,z_0)$, and expanding it in Fourier series, then performing Hankel transform. Alternatively, we can perform a 2D-FFT on $u_x(x,y,z_0)$ to get $\tilde{U_x}(k_x,k_y,z_0)$ and change variables to $\tilde{U_x}(k_r,\theta,z_0)$, then expand it in Fourier series. The Fourier components thus obtained ($\tilde{X}_i^m(k_r,z_0)$) are not exactly $X_i^m(k_r,z_0)$, etc. We will try to find out their relationship in the following.

$$
\begin{aligned}
& u_x(x,y,z_0) \\
&= \int_{-\infty}^{\infty}\int_{-\infty}^{\infty} \tilde{U}(k_x,k_y,z_0)e^{-ik_x x}e^{-ik_y y}dk_x dk_y \\
&= \int_{-\infty}^{\infty}\int_{-\pi}^{\pi} \tilde{U}(k_r,\alpha,z_0)e^{-ik_r r cos(\alpha-\theta)}k_r dk_r d\alpha \\
&= \int_{-\infty}^{\infty}\int_{-\pi}^{\pi}\sum_m [\tilde{X}_1^m(k_r,z_0)cos(m\alpha)+\tilde{X}_2^m(k_r,z_0)sin(m\alpha)]e^{-ik_r r cos(\alpha-\theta)}k_r d\alpha dk_r \\
&= \int_{-\infty}^{\infty}\sum_m \int_{-\pi}^{pi} [\tilde{X}_1^m(k_r,z_0)cosm(\beta+\theta)+\tilde{X}_2^m(k_r,z_0)sinm(\beta+\theta)]e^{-ik_r r cos\beta}k_r d\beta dk_r \\
&= \int_{-\infty}^{\infty}\sum_m [\int_{-\pi}^{\pi} e^{-ik_r r cos\beta}cosm\beta d\beta][\tilde{X}_1^m(k_r,z_0)cosm\theta+\tilde{X}_2^m(k_r,z_0)sinm\theta]k_r dk_r \qquad \text{(C.12)}
\end{aligned}
$$

but, from Abramowitz, et.al [1],

$$
\int_{-\pi}^{\pi} e^{-ik_r r cos\beta}cosm\beta d\beta = 2\int_0^{\pi} e^{-ik_r cos\beta}cosm\beta d\beta = 2\pi i^m J_m(-k_r r) = 2\pi(-i)^m J_m(k_r r) \qquad \text{(C.13)}
$$

So,

$$
X_i^m(k_r,z_0) = 2\pi(-i)^m \tilde{X}_i^m(k_r,z_0) \qquad \text{(C.14)}
$$

where i=1,2.

Similarly

$$
Y_i^m(k_r,z_0) = 2\pi(-i)^m \tilde{Y}_i^m(k_r,z_0) \qquad \text{(C.15)}
$$

$$
Z_i^m(k_r,z_0) = 2\pi(-i)^m \tilde{Z}_i^m(k_r,z_0) \qquad \text{(C.16)}
$$

Bibliography

[1] M Abramowitz and I. A. Stegun. *Handbook of Mathematical Functions: with Formulas, Graphs, and Mathematical Tables.* Dover, New York, 1972.

[2] K. Aki and P. G. Richards. *Quantitative Seismology Theory and Methods.* Freeman, New York, 1980.

[3] C. Garrett amd W. Munk. Space-time scales of internal waves. *Geophy. Fluid Dynamics*, 2:225–264, 1972.

[4] W. S. Ament. *1977 IEEE Ultrasonics Symp. Proc.*, pages 61–66, 1977.

[5] P. Beckmann and A. Spizzichino. *Scattering of light by rough surfaces.* Pergamon, Oxford, 1963.

[6] M. A. Biot. *J. Acoust. Soc. Am.*, 29:1193–1200, 1957.

[7] C. A. Brebbia and S. Walker. *Boundary element techniques in engineering.* Newnes-Butterworths, London, 1980.

[8] L. M. Brekhovskikh. *Waves in Layered Media.* Prentice-Hall, New York, 1980.

[9] H. P. Bucker and H. E. Morris. Normal-mode reverberation in channels or ducts. *J. Acoust. Soc. Am.*, 44:827–828, 1968.

[10] M. Campillo. Modelling of sh wave propagation in an irregularly layered medium - applicatio to seismic profiles near a dome. *Geophysical Prospecting*, 35:236–249, 1987.

[11] D. K. Dacol and D. H. Berman. Sound scattering from a randomly rough fluid-solid interface. *J. Acoust. Soc. Am.*, 84:292–302, 1988.

[12] T. W. Dawson. Acoustic scattering in a three-dimensional oceanic waveguide using boundary integral equation methods. *J. Acoust. Soc. Am.*, 90:2609–2623, 1991.

[13] T. W. Dawson and J. A. Fawcett. A boundary integral equation method for acoustic scattering in a waveguide with non-planar surfaces. *J. Acoust. Soc. Am.*, 87:1110–1125, 1990.

[14] M. E. Dougherty and R. A. Stephen. Geoacoustic scattering from sea-floor features in rose area. *J. Acoust. Soc. Am.*, 82:238–256, 1987.

[15] L. B. Dozier and F. D. Tappert. Statistics of normal mode amplitudes in a random ocean. theory. *J. Acoust. Soc. Am.*, 63:353–365, 1978.

[16] D. D. Ellis. A shallow-water normal-mode reverberation model. *J. Acoust. Soc. Am.*, 97:2804–2814, 1995.

[17] R. B. Evans. A coupled mode solution for propagation in a waveguide with stepwise depth variations of a penetrable bottom. *J. Acoust. Soc. Am.*, 74:188–95, 1983.

[18] W. M. Ewing, W. S. Jardetzky, and F. Press. *Elastic waves in layered media.* McGraw-Hill, New York, 1957.

[19] C. F. Eyring, R. J. Christensen, and R. W. Raitt. Reverberation in the sea. *J. Acoust. Soc. Am.*, 20:462, 1948.

[20] J. A. Fawcett. Directional modal scattering by a ridge. *J. Acoust. Soc. Am.*, 90:1554–1560, 1991.

[21] J. A. Fawcett and T. W. Dawson. Fourier synthesis of three-dimensional scattering in an oceanic waveguide using two-dimensional boundary integral equation methods. *J. Acoust. Soc. Am.*, 88:1913–1920, 1990.

[22] S. M. Flatte and F. D. Tappert. Calculation of the effect of internal waves on oceanic sound transmission. *J. Acoust. Soc. Am.*, 58:1151–1159, 1975.

[23] L. Fortuin. Survey of literature on reflection and scattering of sound waves at the sea surface. *J. Acoust. Soc. Am.*, 47:1209–1228, 1969.

[24] J. R. Fricke. Acoustic scattering from elemental arctic ice features: Numerical modeling results. *J. Acoust. Soc. Am.*, 93:1784–1796, 1993.

[25] J. R. Fricke, R. A. Stephen, and A. B. Baggeroer. Numerical modeling of the scattered acoustic field from elastic ice. *J. Acoust. Soc. Am.*, 83(S1):S37, 1988.

[26] J.R. Fricke. *Acoustic scattering from elastic ice: a finite difference solution.* PhD dissertation, WHOI-MIT Joint Program, June 1991.

[27] P. Gerstoft and H. Schmidt. A boundary element approach to ocean seismoacoustic facet reverberation. *J. Acoust. Soc. Am.*, 89:1629–1642, 1991.

[28] J. Goff and T. Jordan. Stochastic modeling of seafloor morphology: inversion of sea beam data for second order statistics. *J. Geophys. Res.*, 93:13589–13608, 1988.

[29] R. H. Hackman and G. S. Sammelmann. Multiple-scattering analysis for a target in an oceanic waveguide. *J. Acoust. Soc. Am.*, 84:1813–1825, 1988.

[30] R. S. Houston. *A Treatise on Light.* Longmans, Green & Co. Inc., New York, 1938.

[31] M. S. Howe. *Proc. R. Soc.*, A 337:413–433, 1974.

[32] F. Ingenito. Scattering from an object in a stratified medium. *J. Acoust. Soc. Am.*, 82:2051–2059, 1987.

[33] A. N. Ivakin. Sound scattering by random inhomogeneities of stratified ocean sediments. *Sov. Phys. Acoust.*, 32:492–496, 1986.

[34] A. N. Ivakin and Y. P. Lysanov. Theory of underwater sound scattering by random inhomogeneities of the bottom. *Sov. Phys. Acoust.*, 27:61–64, 1981.

[35] F.B. Jensen, W.A. Kuperman, M.B. Porter, and H. Schmidt. *Computational Ocean Acoustics.* American Institute of Physics, New York, 1994.

[36] H. Kawase. Time-domain response of a semi-circular canyon for incident sv, p and rayleigh waves calculated by the discrete wavenumber boundary element method. *Bull. Seismol. Soc. Am.*, 78:1415–1437, 1988.

[37] H. Kawase and K. Aki. A study on the response of a soft basin for incident s, p and rayleigh waves with special reference to the long duration observed in mexico city. *Bull. Seismol. Soc. Am.*, 79:1361–1382, 1989.

[38] H. Kawase and K. Aki. Topolography effect at the critical sv wave incidence: possible explanations of dammage pattern by the whittier narrows, california, earthquake of 1 october 1987. *Bull. Seismol. Soc. Am.*, 80:1–22, 1990.

[39] J. S. Kim. *Radiation from directional seismic sources in laterally stratified media with application to Arctic ice cracking noise.* PhD dissertation, Massachusetts Institute of Technology, Department of Ocean Engineering, September 1989.

[40] G. R. Kirchhoff. *Vorlesung uber mathematische physik, Vol. II.* Teubner, Leipzig, 1891.

[41] W.A. Kuperman and H. Schmidt. Self-consistent perturbation approach to rough surface scattering in stratified elastic media. *J.Acoust.Soc.Am.*, 86:1511–1522, 1989.

[42] K. LePage and H. Schmidt. Modeling of low frequency transmission loss in the central arctic. *J.Acoust.Soc.Am.*, 96:xxxx, 1994.

[43] K. LePage, D.J. Tang, and Henrik Schmidt. An improved kirchhoff approximation for scattering from penetrable media using the operaor expansion. *J. Acoust. Soc. Am.*, 91:2342 (A), 1992.

[44] K.D. LePage. *Elastic scattering in oceanic waveguides.* PhD dissertation, Massachusetts Institute of Technology, Department of Ocean Engineering, September 1992.

[45] D. Li. *Low-frequency bottom backscattering data analysis using multiple constraints beamforming.* Master thesis, WHOI-MIT Joint Program, June 1995.

[46] R. Lim. Scattering by objects buried in underwater sediments: Theory and experiment. *J.Acoust.Soc.Am.*, 93:1762–1784, 1993.

[47] J.Y. Liu, H. Schmidt, and W.A. Kuperman. Effect of a rough seabed on the spectral composition of deep ocean infrasonic ambient nose. *J.Acoust.Soc.Am.*, 93:753–769, 1993.

[48] N. C. Makris, L. Z. Avelino, and R. Menis. Deterministic reverberation from ocean ridges. *J.Acoust.Soc.Am.*, 97:3547–3574, 1995.

[49] B. B. Mandelbrot. *The fractal geometry of nature.* W. H. Freeman, New York, 1985.

[50] J. Miklowitz. *The Theory of Elastic Waves and Waveguides.* North-Holland, New York, 1984.

[51] P. M. Morse. *Vibration and Sound.* McGraw-Hill, New York, 1948.

[52] J.E. Murphy and S.A. Chin-Bing. A seismo-acoustic finite element model for underwater acoustic propagation. *In Shear Waves in Marine Sediments, edited by J.M. Hovem, M.D. Richardson, and R.D. Stoll (Kluwer Academic Publishers, The Netherlands)*, pages 463–470, 1991.

[53] J.A. Ogilvie. Wave scattering from rough surfaces. *Rep. Prog. Phys.*, 50:1553–1608, 1987.

[54] C. L. Pekeris. Note on the scattering of radiation in an inhomogeneous medium. *Phys. Rev.*, 71:268, 1947.

[55] Lord Rayleigh. On the dynamical theory of gratings. *Proc. Roy. Soc.*, A 79:399–416, 1907.

[56] Lord Rayleigh. *The theory of sound vol. 2.* Macmillan, London, 1978.

[57] S. O. Rice. *Commun. Pure Appl. Maths.*, 4:351–378, 1951.

[58] D. C. Ricks. *Elastodynamic modeling of fluid-loaded cylinderical shells with multiple layers and internal attachments.* PhD dissertation, MIT, May 1994.

[59] H. Schmidt. *SAFARI:Seismo-acoustic fast field algorithm for range independent environments. User's guide.* SR 113, SACLANT ASW Research Centre, La Spezia, Italy, 1987.

[60] H. Schmidt and J. Glattetre. A fast field model for three-dimensional wave propagation in stratified environments based on the global matrix method. *J. Acoust. Soc. Am.*, 78:2105–2114, 1985.

[61] H. Schmidt and F.B. Jensen. A full wave solution for propagation in multilayered viscoelastic media with application to gaussian beam reflection at fluid-solid interfaces. *J. Acoust. Soc. Am.*, 77:813–825, 1985.

[62] H. Schmidt and S. Krenk. Asymmetric vibrations of a circular elastic plate on an elastic half-space. *Int. J. Solids Struct.*, 18:91–105, 1982.

[63] H. Schmidt and W.A. Kuperman. Spectral representations of rough interface reverberation in stratitied ocean waveguides. *J. Acoust. Soc. Am.*, 10:xxxx, 1994.

[64] H. Schmidt and G. Tango. Efficient global matrix approach to the computation of synthetic seismograms. *Geophys. J. R. Astr. Soc.*, 84:331–359, 1986.

[65] G. T. Schuster and L. C. Smith. Modeling scatterers embedded in a plane-layered media by a hybrid haskell-thomson and boundary integral equation method. *Commun. Pure Appl. Maths.*, 78:1387–1394, 1985.

[66] Woojae Seong. *Hybrid Galerkin boundary element - wavenumber integration method for acoustic propagation in laterally inhomogeneous media.* PhD dissertation, Massachusetts Institute of Technology, Department of Ocean Engineering, February 1990.

[67] L. M. Spetner. *Trans. IRE*, AP-6:88–94, 1958.

[68] J. H. Stockhausen. Scattering from the volume of an inhomogeneous half-space. *Naval Research Establishment Report*, 63/9, 1963.

[69] D. Tang. *Acoustic wave scattering from a random ocean bottom.* PhD dissertation, WHOI-MIT Joint Program, 1991.

[70] D. Tang and G. V. Frisk. Plane-wave reflection from a random fluid half-space. *J. Acoust. Soc. Am.*, 90:2751–2756, 1991.

[71] D. Tang and G. V. Frisk. Spectral parameterization of sound scattering from a random ocean bottom. *J. Acoust. Soc. Am.*, 92:2792–2799, 1992.

[72] D. Tang and G. V. Frisk. Spatial correlation of acoustic wave scattered from a random ocean bottom. *J. Acoust. Soc. Am.*, 97:2783–2803, 1995.

[73] E. I. Thorsos and D. R. Jackson. The validity of the perturbation approximation for rough surface scattering using a gaussian roughness spectrum. *J. Acoust. Soc. Am.*, 86:261–277, 1989.

[74] I. Tolstoy and C. S. Clay. *Ocean Acoustics: Theory and experiment in underwater sound.* American Institute of Physics, New York, 1987.

[75] V. Twersky. Multiple scattering of radiation by an arbitrary configuration of parallel cylinders. *J. Acoust. Soc. Am.*, 24:42–46, 1952.

[76] V. Twersky. On scattering and reflection of sound by rough surfaces. *J. Acoust. Soc. Am.*, 29:209–255, 1957.

[77] V. Twersky. Multiple scattering of sound by correlated monolayers. *J. Acoust. Soc. Am.*, 73:68–84, 1983.

[78] V. Twersky. Reflection and scattering of sound by correlated rough surfaces. *J. Acoust. Soc. Am.*, 73:85–94, 1983.

[79] V. Twersky. Coherent response to a point source irradiating a rough plane. *J. Acoust. Soc. Am.*, 76:1847–1863, 1984.

[80] R. J. Urick. The processes of sound scattering at the ocean surface and bottom. *J. Mar. Res.*, 15:134, 1956.

[81] R. J. Urick. *Principles of underwater sound, 3rd ed.* McGraw-Hill, New York, 1983.

[82] R. J. Urick and R. M. Hoover. Backscattering of sound from the sea surface: its measurement, casuses, and application to the prediction of reverberation levels. *J. Acoust. Soc. Am.*, 28:1038, 1956.

[83] P. C. Waterman. New formulation of acoustic scattering. *J. Acoust. Soc. Am.*, 45(6):1417–1429, 1969.

[84] P. C. Waterman. Matrix theory of elastic wave scattering. *J. Acoust. Soc. Am.*, 60(3):567–579, 1976.

[85] R. H. Zhang and G. L. Jin. Normal-mode theory of the average reverberation intensity in shallow water. *J. Sound Vib.*, 119:215–223, 1987.

[86] O. C. Zienkiewitz. *The finite element method, 3rd edition.* McGraw-Hill, New York, 1977.